Experimental and Numerical Study on Evaporation of Water at Low Pressures

by

Mohammad Amin Kazemi

A thesis submitted in partial fulfillment of the requirements for the degree of

Doctor of Philosophy

in

Chemical Engineering

Department of Chemical and Materials Engineering
University of Alberta

Abstract

Although evaporation is considered to be a surface phenomenon, the rate of molecular transport across a liquid–vapor boundary is strongly dependent on the coupled fluid dynamics and heat transfer in the bulk fluids. Recent experimental thermocouple measurements of the temperature field near the interface of evaporating water into its vapor have begun to show the role of heat transfer in evaporation. However, the role of fluid dynamics has not been explored sufficiently. Here, a combined numerical and experimental study is performed to demonstrate how the simultaneous effects of heat transfer and fluid dynamics influence the evaporation of a liquid at low pressures. For this purpose, the liquid velocities near the interface during evaporation from two different geometries (a cylindrical tube and a rectangular cuvette) are measured using particle image velocimetry. The temperature profiles in the liquid and vapor near the interface along the centerline are also measured using a fine thermocouple. A mathematical model is developed to describe the coupling of the heat, mass, and momentum transfer in the fluids with the transport phenomena at the interface. The model is validated with the experimentally measured velocity fields, temperature profiles, and evaporation rates. Once demonstrating good agreement with the experimental data, the model is then used to understand the experimentally obtained velocity field in the liquid and temperature profiles in the liquid and vapor, in evaporation from a concave meniscus for various vacuum pressures.

By using the validated model, it is shown that an opposing buoyancy flow in the liquid, even though it occurs at relatively small velocities, can suppress the thermocapillary flow in water during evaporation at low pressures. As such, in the absence of thermocapillary convection, the evaporation is controlled by heat transfer to the interface, and the predicted behavior of the system

is independent of choosing between the existing theoretical expressions for evaporation flux. The possibility of occurrence of a thermocapillary convection at the interface is further explored numerically by increasing the thermal conductivity of the container that holds the liquid in the model. By doing so, it is found that thermocapillary convection at the interface can occur at higher thermal conductivities and increases the evaporation flux significantly. However, the occurrence of a thermocapillary flow does not guarantee that the heat transfer limitations to the evaporation are removed completely. The influence of the liquid thin film formed in the corner of the rectangular cuvette is studied experimentally and numerically. Both confirmed that the contribution of the thin films is negligible in the total evaporation rates. The temperature discontinuity at the interface is also investigated and it is confirmed that the discontinuity strongly depends on the heat flux from the vapor side, which depends on the geometrical shape of the interface. The reliability of the thermocouples in measuring the interfacial temperature discontinuities is also studied and discussed extensively.

Preface

The research described herein is original work by the author Mohammad Amin Kazemi. Prof. Janet A.W. Elliott provided me with helpful ideas and thoughts in developing the theoretical sections of this study. Professor David S. Nobes also provided me with his constructive suggestions on performing the experiments.

Chapter 2 with some modifications in the experimental section has been published as: Kazemi, M. A.; Elliott, J. A. W.; Nobes, D. S. Determination of the Three Components of Velocity in an Evaporating Liquid from Scanning PIV. In the *18th International Symposium on the Application of Laser and Imaging Techniques to Fluid Mechanics, July 4 – 7; Lisbon Portugal*, 2016. Also, preliminary parts of Chapter 2 have been published as: Kazemi, M. A.; Elliott, J. A. W.; Nobes, D. S. A 3D Flow Visualization in Evaporation of Water from a Meniscus at Low Pressures. In the *10th Pacific Symposium on Flow Visualization and Image Processing, Naples, Italy, 15-18 June*; 2015.

Chapter 3 with minor modifications has been published as Kazemi, M. A.; Nobes, D. S.; Elliott, J. A. W. Experimental and Numerical Study of the Evaporation of Water at Low Pressures. *Langmuir* 2017, 33 (18), 4578–4591.

Chapter 4 as well as Appendix F and Appendix G with minor modifications have been published as Kazemi, M. A.; Nobes, D. S.; Elliott, J. A. W. Effect of the Thermocouple on Measuring the Temperature Discontinuity at a Liquid–Vapor Interface. *Langmuir* 2017, *33* (28), 7169–7180.

Chapter 5 is to be submitted as Kazemi, M. A.; Nobes, D. S.; Elliott, J. A. W.; Investigation of the phenomena occurring near the liquid–vapor interface during evaporation of water at low pressures.

The design and installation of the experimental setup, as well as the preparation of the CVI code for automated temperature measurements, were provided primarily by Professor David S. Nobes and his graduate student Xudong (Terry) Song. However, I was responsible for the installation of the components required for the PIV experiments and performing all the experiments presented in the current study. Also, the 3D image processing with DaVis software was performed with assistance from Dr. Sina Ghaemi.

Acknowledgements

Firstly, I would like to express my sincere gratitude to my supervisors Prof. Janet A.W. Elliott and Prof. David S. Nobes for their continuous support of my Ph.D. study, for their patience, motivation, and immense knowledge. Their guidance helped me in all the time of research and writing of this thesis. Besides, I would like to thank the rest of my thesis committee: Prof. Patricio F. Mendez for his encouragement, insightful comments, constructive feedback, and challenging questions. I would also like to take this opportunity to thank the examiners, Prof. Sanjeev Chandra and Prof. Robert E. Hayes, for their very helpful comments and suggestions.

I am deeply grateful to my beloved wife, Maryam, for her endless confidence, encouragement, and patience during my studies. I am also grateful to my parents who have supported me along the way.

A very special gratitude goes out to Natural Sciences and Engineering Research Council (NSERC) of Canada, the Alberta Ingenuity Fund, and the Canadian Foundation for Innovation (CFI) for providing the funding for the work.

Table of Contents

Chapter 1: Introduction 1

1.1 Motivation 1

1.2 Thesis scope 4

1.3 References 5

Chapter 2: Determination of the Three Components of Velocity in the Evaporating Liquid from Scanning PIV 7

2.1 Introduction 7

2.2 Experimental setup and procedure 9

2.2.1 Experimental setup and facilities 9

2.2.2 Scanning PIV setup 10

2.2.3 Material preparation for the scanning PIV 11

2.2.4 Moving light sheet and data recording 12

2.2.5 Calibration of the camera 13

2.2.6 Data processing 14

2.3 Results and discussion 17

2.4 Conclusion 22

2.5 References 23

Chapter 3: Evaporation of Water from a Meniscus in a Cylindrical Cuvette 26

3.1 Introduction 26

3.2 Experimental investigation 29

3.2.1 Experimental apparatus and procedure 30

3.2.2 Velocity measurement 31

3.2.3 Temperature measurement 32
3.2.4 Evaporation flux measurement 35
3.3 Formulation of governing equations 36
3.3.1 Model description 36
3.3.2 Initial and boundary conditions 37
3.4 Results and discussion 41
3.4.1 Flow pattern in liquid and vapor 43
3.4.2 Interfacial temperatures 50
3.4.3 Temperature discontinuity 52
3.4.4 Evaporation flux *vs*. pressure 54
3.5 Conclusion 57
3.6 References 59
Chapter 4: Effect of the Thermocouple on Measuring the Temperature Discontinuity at the Liquid–Vapor Interface 64
4.1 Introduction 65
4.2 Description of the experimental setup of Badam et al.[4,19] 70
4.3 Mathematical modeling 71
4.3.1 Determination of the vapor flow regime 71
4.3.2 Governing equations 73
4.3.3 Boundary conditions 75
4.4 Solution procedure 79
4.5 Results and discussion 81
4.5.1 Model validation 81
4.5.2 Velocity field 82
4.5.3 Interfacial temperatures 84

4.6 Further remarks 89
4.7 Conclusion 91
4.8 References 92
Chapter 5: Evaporation of Water from a Meniscus in a Rectangular Cuvette 96
5.1 Introduction 96
5.2 Experiments 100
5.2.1 Description of the experimental setup 100
5.2.2 Velocity measurement 102
5.2.3 Temperature measurement 102
5.2.4 Evaporation flux measurement 103
5.3 Mathematical Model 103
5.3.1 Problem description 103
5.3.2 Formulation of governing equations 104
5.3.3 Numerical Analysis 109
5.4 Results and Discussion 110
5.4.1 Velocity field in the liquid 110
5.4.2 Interfacial flows in pure liquid 115
5.4.3 Temperatures in the liquid and vapor 119
5.4.4 Liquid temperatures along the interface 121
5.4.5 Evaporation flux 123
5.4.6 Interfacial transport limit *vs*. heat transfer limit 126
5.5 Summary and Conclusions 128
5.6 References 130
Chapter 6: Final remarks and conclusions 135

Bibliography 141

Appendix A: Cylindrical Image Distortion Correction in MATLAB 155

Appendix B: Calibration of the Thermocouple with the Thermometer 160

Appendix C: Determination of the Time Constants of the Thermocouple in the Liquid and Vapor 161

Appendix D: Calculation of the Area of the Interface 162

Appendix E: Mesh Convergence Study in the Numerical Simulations 164

Appendix F: The Sensitivity of SRT to the Temperature of Vapor at the Interface 166

Appendix G: Estimation of the Effect of Thermal Radiation on Thermocouple Readings 167

List of Figures

Graphical Abstract – Chapter 2 7

Figure 2-1 The experimental setup 11

Figure 2-2 The timing diagram of control signals 12

Figure 2-3 Calibration of the camera 14

Figure 2-4 Two different methods of image processing 15

Figure 2-5 3D illustration of velocity vectors 18

Figure 2-6 The effect of the smoothing of in-plane velocity components 19

Figure 2-7 Comparison between the out-of-plane velocities 21

Figure 2-8 Comparison of *w* obtained from different boundary conditions 22

Graphical Abstract – Chapter 3 26

Figure 3-1 Schematic illustration of the experimental setup 31

Figure 3-2 Recession of the interface during the measurement of the evaporation flux 35

Figure 3-3 Comparison of the simulated velocities (right) with the experimental velocities obtained from PIV (left) 44

Figure 3-4 Velocity magnitude and interrogation windows near the interface 46

Figure 3-5 The experimental (left of each panel) and simulated (right of each panel) velocity field in the liquid at different pressures after imposing a zero tangential velocity on the interface. 48

Figure 3-6 Simulated velocity magnitude and direction above the interface at different pressures 49

Figure 3-7 Temperature distribution near the interface along the vertical centerline 51

Figure 3-8 (a) The difference between the vapor side heat flux to the interface in this study and a typical study by Ward and Stanga 53

Figure 3-9 Comparison of the simulated evaporation flux using two different theoretical expressions for flux with the experimental data 56
Graphical Abstract – Chapter 4 63
Figure 4-1 Schematic representation of the experimental setup used in the Badam et al. studies. 71
Figure 4-2 The position of the bead in the simulation when the thermocouple measures the interfacial temperatures. 79
Figure 4-3 Comparison between the experimental and simulated temperatures of the bead. 82
Figure 4-4 The effect of the thermocouple on the simulated velocity distribution in the vapor (a,b) and in the liquid (c,d) 83
Figure 4-5 Comparison of the interfacial temperatures obtained from the experiments and simulations 86
Figure 4-6 Comparison between the experimental and predicted temperature jumps at the interface for two values of energy accommodation coefficient 87
Graphical Abstract – Chapter 5 95
Figure 5-1 The vacuum chamber and other components used in evaporation experiments 102
Figure 5-2 Representation of the simplified experimental setup that was studied numerically . 104
Figure 5-3 3C3D experimental velocity vectors below the evaporating meniscus for a typical pressure of 190 Pa 112
Figure 5-4 Comparison of the simulated and experimental velocity magnitudes in liquid at three pressures 114
Figure 5-5 Simulated velocity magnitude and direction at 300 Pa 116

Figure 5-6 Experimental and simulated temperature profiles in the liquid and vapor along the centerline at five pressures 121
Figure 5-7 Interfacial temperatures in the liquid during evaporation at 382 Pa 122
Figure 5-8 Experimental and simulated evaporation fluxes as a function of pressure in the vacuum chamber 124
Figure 5-9 The position of the interface *vs*. time for a typical experiment at 380 Pa 126
Figure 5-10 Simulated evaporation flux *vs*. thermal conductivity of the cuvette at three pressures 128
Figure B1 Calibration curve that converts the temperatures read by the thermocouple 160
Figure C1 Responses of the thermocouple 161
Figure D1 The area of the interface formed in the cylindrical cuvette 162
Figure D2 The area of the interface formed in the rectangular cuvette 163
Figure E1 Illustration of the domains used in the numerical simulation 164
Figure E2 Reduction of the relative error while calculating the evaporation flux 165
Figure G1 The arrangement of the thermocouple and the heating element 168

List of Tables

Table 2-1 Discretized equations obtained from the 1st and 2nd order finite difference schemes. 16

Table 3-1 Thermodynamic properties of the liquid, vapor and solids used in the simulation..... 43

Table 3-2 Interfacial temperatures in liquid and vapor at the centerline measured by the thermocouple..... 52

Table 3-3 Comparison of the evaporation fluxes calculated in the simulation with and without the temperature jump at the interface. 54

Table 4-1 Physical properties used in the simulation 80

Table 4-2 Experimental conditions extracted from ref. 19. 80

Table 4-3 Comparison between the experimental and simulated temperature jumps and the prediction of KTG. 88

Table 4-4 The predicted pressures by SRT before and after applying the simulated interfacial temperatures. 89

Table 5-1 Physical properties of the fluids and solids used in the simulation. 110

Table 5-2 Comparison between the experimental and simulated temperature jumps. 119

Table B1 Comparison between the thermometer and thermocouple readings 160

Table F1 Three selected experimental conditions near an evaporating droplet..... 166

Chapter 1: Introduction

1.1 Motivation

Evaporation is a ubiquitous phenomenon that takes place ceaselessly in nature and is vital to maintaining life on earth. This phenomenon has attracted a considerable amount of research attention as it pertains to a variety of disciplines ranging from engineering and astronomy to biology, botany, and agriculture. Investigations on the evaporation phenomenon have increased significantly in the past few decades and have led to promising advances in the relevant technological applications such as heat pipe cooling systems,[1] ink jet printing,[2] self-assembly of nanoparticles,[3] and recently, electricity generation,[4] and evaporation–driven engines.[5] Meanwhile, fundamental studies on evaporation are still necessary as they result in innovations while developing solutions to practical problems.

The vast majority of the studies in the literature are devoted to the evaporation of a liquid, usually in the form of a sessile droplet, into a noncondensable gas such as air. In this limit of evaporation, the transport of molecules in the vapor phase often determines the conditions at the interface and in the bulk of the fluids. As a result, the evaporation flux from the liquid–vapor interface is usually calculated from the solution of the Laplace equation for the vapor concentration by assuming chemical equilibrium at the interface. The theoretical study of Hu and Larson[6] on the prediction of the evaporation flux at a droplet interface as well as the experimental observation of the coffee ring phenomenon by Deegan *et al*.[7] have been the most prominent publications around which many studies recently have revolved.

In contrast to the evaporation into noncondensable gases, however, evaporation of a liquid into its vapor has not received as much attention in the past, perhaps due to the complexity and difficulty associated with the experimental studies in low-pressure environments. In this limit of evaporation, the diffusion of vapor molecules usually takes place very fast and has a negligible contribution to the evaporation rate. Accordingly, the evaporation flux cannot be calculated simply from the solution of the Laplace equation of the vapor concentration. This is because the assumption of chemical equilibrium at the interface that was made in the previous limit, does not hold anymore and the concentration of the vapor at the interface is unknown. Rather, the interfacial

conditions at the liquid–vapor boundary (*i.e.*, the transport of molecules across the interface and transport of energy to the interface) are the determining mechanisms of the evaporation process. Most of the understanding and knowledge of evaporation in this limit was achieved from the theoretical studies of Hertz,[8,9] Knudsen,[10] and Schrage,[11] which were based on the kinetic theory of gases. In 1999 however, Ward and Fang[12] measured a relatively large temperature discontinuity at the liquid–vapor interface during evaporation, which was not in agreement with the Hertz–Knudsen–Schrage theory. As a result, they proposed a new expression for predicting the evaporation flux, known as statistical rate theory (SRT), based on the transition probability concept in quantum mechanics, which was in agreement with the measured temperature jumps.

Although the subsequent studies after the new finding of the temperature jumps and the SRT expression for evaporation flux have provided valuable insights into the problem of evaporation of a liquid into its vapor, they have essentially focused on assessing the energy balance at the interface regardless of the potential role of internal dynamics of the fluids on the evaporation phenomenon. In other words, these studies have focused only on the interfacial conditions during evaporation such as the interfacial heat fluxes and temperature profiles close to the interface. However, they have not provided sufficient detail on the circumstances that gave rise to the existing conditions at the interface as there is a strong interplay between the interfacial phenomena and the internal flow dynamics. As a result, there are still some key open questions that have not been addressed yet. Accordingly, an experimental and theoretical study on evaporation of water into its vapor at low pressure has been carried out to contribute to enhancing current knowledge of the evaporation phenomenon. The current study was performed on evaporation of water in two different geometries, a cylindrical borosilicate tube and a rectangular quartz cuvette. In the experimental section, particle image velocimetry (PIV) was utilized to quantify the flow field in the liquid during evaporation in a low-pressure environment. For the cylindrical tube, the PIV was performed only on the center plane due to the axial symmetry. However, for the rectangular cuvette, the full three-dimensional three-component velocity field in the volume was obtained by developing a scanning PIV. The applicability of the continuity equation in predicting the out-of-plane component of the velocity was also assessed. Moreover, in the experimental section, we measured the temperature profiles in the vapor and liquid along the centerline of both containers

using a fine thermocouple. The temperature jumps at the interface were quantified and compared to the previous studies.

In the theoretical section, a mathematical model of the system is developed which accounts for mass, momentum, and heat transport in the liquid and vapor, as well as the phase change at the interface. The buoyancy effects in both phases and the thermocapillary effects, which are usually overlooked in the thermal boundary condition at the interface, are both taken into account. Also, to assess the reliability of the reported temperature jumps in previous studies, a numerical study on a thermocouple when it measures the interfacial temperatures of the liquid and vapor has also been performed. By using the mathematical model that is validated with the experimental data, several questions about the evaporation phenomenon have been addressed. The most significant ones are summarized in the following. One of the most important questions that have been around for many years is that of why the thermocapillary flow in pure water during evaporation, in contrast to other liquids, does not always occur although the Marangoni number is far above the critical established value?[13] Although it is well known that the impurities at the liquid interface can suppress the interfacial flows,[14] this is probably not the reason that makes water behave differently from other liquids. In the current study, another possible answer to this question has been proposed.

Another issue that needs to be addressed is that of under what circumstances is the evaporation controlled by the interfacial resistances across the interface (interfacial transport limit) and when is it constrained by the energy transfer to the interface (heat transfer limit). This is important to know because if the experiments that are designed to investigate the temperature jumps and evaporation coefficients at the interface are performed in the interfacial-transport-limited region, the results are less prone to be affected by the limitations in the accuracy and the resolution of the currently available experimental devices. This is because when the heat transfer limitation is removed, the evaporation rate increases significantly which is accompanied by a significant increase in the temperature jump at the interfaces.[15] As shown in the next chapters, the experiments performed in this study and most probably those performed previously by others have all been conducted in the heat transfer limited region. The heat transfer limitation was demonstrated by using the numerical simulation and this thesis provides practical insight as to how to improve the experiments so that the heat transfer limitations can be removed significantly.

The last question but not the least, is that of how reliable the measured temperature discontinuities on the interface can be. The theoretical prediction by kinetic theory of gases (KTG) as well as the experimental measurements of the vapor temperatures above an evaporating interface at low pressures both demonstrate the existence of a sharp temperature variation in a small distance above the liquid–vapor interface. Given that thermocouples have been the only established device to measure these temperature variations (including the temperature of the vapor at the interface), one may doubt the reliability of the thermocouples to be used in such measurements. In other words, regardless of how carefully the measurements are performed, it is possible that the thermocouples do not show the temperatures in the vapor correctly, due to the following reasons: *i*) The sharp temperature variation can induce the flow of heat toward the thermocouple junction which leads to reading a higher temperature by the thermocouple, *ii*) The junction temperature can be remarkably different from the local vapor temperature due to rarefaction effects which decrease the thermal heat transfer between the warmer thermocouple junction (induced by (*i*)) and the colder low-density vapor, and *iii*) The thermocouple junction can never reach the interface due to the experimental limitations and the finite size of the junction. As a result of the abovementioned factors, the measured temperatures in the vapor close to the interface have most likely been higher than the actual temperatures, leading to misinterpretation of the temperature jumps at the interface. Accordingly, we have investigated the reliability of the thermocouples during the measurements of the interfacial temperatures determining what portion of the reported temperature jumps exist at the interface and what portion are only a spurious effect of the thermocouple.

1.2 Thesis scope

This thesis was prepared in a paper-based format. The remainder of this thesis is organized as follows:

In Chapter 2, the experimental setup, preparation and procedure, and the scanning particle image velocimetry (PIV) method that was used to quantify the velocity field inside the liquid during the evaporation are explained.

In Chapter 3, an experimental and a numerical investigation on the evaporation of water from a cylindrical tube at low pressures is presented. In this chapter, a 2D mathematical model is developed which takes into account the recession of the interface during evaporation. A cylindrical tube was selected for the evaporation experiments to simplify the system from three-dimensional to a two-dimensional axisymmetric problem which is much easier for the numerical study.

In Chapter 4 a numerical study is described on the reliability of thermocouples while they measure the interfacial temperatures in the vapor and liquid in low-pressure experiments. A typical evaporation study[16,17] was chosen in which the authors have reported the largest temperature jumps at a water–vapor interface. By simulating their experimental setup and their thermocouple, we determine what portion of the temperature jumps they reported may be due to the thermal effects of the thermocouple during the measurements.

In Chapter 5, a similar study to that in Chapter 3 is performed, with the difference being that the evaporation takes place in a rectangular geometry. By using the 3D geometry, although the model does not account for the recession of the interface during evaporation, more details about the evaporation phenomena are revealed, which were not studied in Chapter 3.

In Chapter 6, the main points and the contribution of our research have been summarized and some thoughts and directions for future studies have been offered.

1.3 References

(1) Faghri, A. Review and Advances in Heat Pipe Science and Technology. *J. Heat Transfer* **2012**, *134* (12), 123001.

(2) Lim, T.; Han, S.; Chung, J.; Chung, J. T.; Ko, S.; Grigoropoulos, C. P. Experimental Study on Spreading and Evaporation of Inkjet Printed Pico-Liter Droplet on a Heated Substrate. *Int. J. Heat Mass Transf.* **2009**, *52* (1–2), 431–441.

(3) Sau, T. K.; Murphy, C. J. Self-Assembly Patterns Formed upon Solvent Evaporation of Aqueous Cetyltrimethylammonium Bromide-Coated Gold Nanoparticles of Various Shapes. *Langmuir* **2005**, *21* (7), 2923–2929.

(4) Xue, G.; Xu, Y.; Ding, T.; Li, J.; Yin, J.; Fei, W.; Cao, Y.; Yu, J.; Yuan, L.; Gong, L.; et al. Water-Evaporation-Induced Electricity with Nanostructured Carbon Materials. *Nat. Nanotechnol.* **2017**, *12* (4), 317–321.

(5) Chen, X.; Goodnight, D.; Gao, Z.; Cavusoglu, A. H.; Sabharwal, N.; DeLay, M.; Driks, A.;

Sahin, O. Scaling up Nanoscale Water-Driven Energy Conversion into Evaporation-Driven Engines and Generators. *Nat. Commun.* **2015**, *6* (June), 7346.

(6) Hu, H.; Larson, R. G. Evaporation of a Sessile Droplet on a Substrate. *J. Phys. Chem. B* **2002**, *106* (6), 1334–1344.

(7) Deegan, R. D.; Bakajin, O.; Dupont, T. F.; Huber, G.; Nagel, S. R.; Witten, T. A. Capillary Flow as the Cause of Ring Stains from Dried Liquid Drops. *Nature* **1997**, *389* (6653), 827–829.

(8) Persad, A. H.; Ward, C. A. Expressions for the Evaporation and Condensation Coefficients in the Hertz-Knudsen Relation. *Chem. Rev.* **2016**, *116* (14), 7727–7767.

(9) Hertz, H. Ueber Die Verdunstung Der Flüssigkeiten, Insbesondere Des Quecksilbers, Im Luftleeren Raume. *Ann. Phys.* **1882**, *253* (10), 177–193.

(10) Knudsen, M. *Kinetic Theory of Gases*; 3rd ed.; London Methuene: London, 1950.

(11) Schrage, R. W. *A Theoretical Study of Interphase Mass Transfer*; Columbia University Press: New York, 1953.

(12) Fang, G.; Ward, C. A. Temperature Measured close to the Interface of an Evaporating Liquid. *Phys. Rev. E* **1999**, *59* (1), 417–428.

(13) Thompson, I.; Duan, F.; Ward, C. A. Absence of Marangoni Convection at Marangoni Numbers above 27,000 during Water Evaporation. *Phys. Rev. E* **2009**, *80* (5), 56308.

(14) Hu, H.; Larson, R. G. Analysis of the Effects of Marangoni Stresses on the Microflow in an Evaporating Sessile Droplet. *Langmuir* **2005**, *21* (9), 3972–3980.

(15) Cipolla, J. W. Kinetic Theory of Condensation and Evaporation. II. *J. Chem. Phys.* **1974**, *61* (1), 69.

(16) Badam, V. K. Experimental and Theoretical Investigation of the Evaporation of Fluids from Free Surfaces. PhD Thesis, University of Erlangen-Nuremberg (2007).

(17) Badam, V. K.; Kumar, V.; Durst, F.; Danov, K. Experimental and Theoretical Investigations on Interfacial Temperature Jumps during Evaporation. *Exp. Therm. Fluid Sci.* **2007**, *32* (1), 276–292.

Chapter 2: Determination of the Three Components of Velocity in the Evaporating Liquid from Scanning PIV[†]

This chapter describes the experimental investigation of the three-dimensional flow field within water during evaporation at a reduced pressure. Scanning particle image velocimetry is used to measure the three components of velocity in the volume. The images of particles captured during successive rapid scans of the volume were processed using two different methods, namely a three-dimensional PIV algorithm, and a two-dimensional PIV algorithm combined with the continuity equation. The velocity fields obtained from both methods were in good agreement.

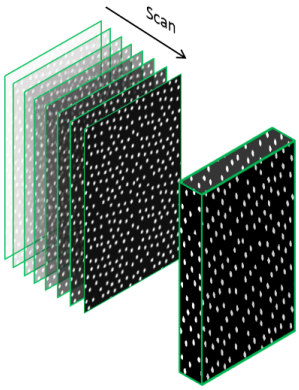

Graphical Abstract
Chapter 2

2.1 Introduction

Evaporation from the interface of a liquid may result in instabilities in the liquid. These instabilities are mainly generated by a surface tension gradient on the interface,[1,2] known as Marangoni convection, and/or by a density variation in the bulk liquid, known as Rayleigh—Bénard convection.[3,4] They play an important role in many fields including crystallization,[5,6] heat pipe cooling,[7,8] particle self-assembly on surfaces,[9,10] welding,[11,12] and spray cooling,[13] and can significantly enhance the heat/mass transfer coefficients at the liquid–vapor interface by supplying the required energy to the interface.[14] Therefore, understanding flow instability dynamics by

[†] This chapter with some modifications in the experimental section has been published as: Kazemi, M. A.; Elliott, J. A. W.; Nobes, D. S. Determination of the Three Components of Velocity in an Evaporating Liquid from Scanning PIV. In the *18th International Symposium on the Application of Laser and Imaging Techniques to Fluid Mechanics, July 4 – 7; Lisbon Portugal*, 2016. Also, preliminary parts of this chapter have been published as: Kazemi, M. A.; Elliott, J. A. W.; Nobes, D. S. A 3D Flow Visualization in Evaporation of Water from a Meniscus at Low Pressures. In the *10th Pacific Symposium on Flow Visualization and Image Processing, Naples, Italy, 15-18 June*; 2015.

visualization and quantification of the full three-dimensional (3D) velocity field within the liquid will lead to an increased understanding of how flow instabilities enhance the heat/mass transfer as well as how they can be controlled.

Investigation of the 3D velocity can be performed using a number of techniques including defocusing particle image velocimetry (PIV),[15] multi-view PIV,[16] holographic PIV,[17] and scanning PIV.[18] Detailed reviews of the available techniques for both 2D and 3D PIV are provided by Gao *et al.*[19] and Wereley and Meinhart.[20] Since in this study investigation of the instabilities during evaporation at extremely low pressures (~6×10^{-3} bar) was the purpose, a vacuum chamber made up of metallic parts had to be used. This led to limited optical access to the evaporating liquid through the small viewing windows. In such vacuum chambers, multi-view PIV methods such as tomographic PIV[16] which require using multiple cameras to capture images from different viewing angles are difficult to implement. This may be one of the reasons that there are few studies in the literature which investigate the full velocity field in the volume of an evaporating liquid at vacuum pressures. Nevertheless, there are a few studies that have dealt with liquid velocity measurement during evaporation at low pressures. For instance, Ward and Duan[21] measured one component of the velocity close to the interface of an evaporating water in a vacuum chamber by measuring the deflection of an elastic probe which was submerged into the liquid. In another study, Song and Nobes[22] used 2D PIV to measure the two components of the velocity in a single plane located at the center of an evaporating water in a vacuum chamber. Even for evaporation at atmospheric pressure which does not have the limitation stated above, there is still a lack of studies in the literature that present the full velocity field within an evaporating liquid and most of them are limited to performing 2D PIV on a single plane,[23] 2D PIV on multiple planes,[24–28] and digital holographic microscopy.[29] Although the latter performed their measurements in 3D, they only studied the velocity of a single particle by tracking it in the volume of an evaporating liquid.

Here, a scanning PIV method was employed to measure the three components of the velocity below an evaporating meniscus and within the bulk of the liquid at low pressures. The technique was firstly introduced by Brücker[30] and has been utilized by researchers to investigate fluid flows including separation of a bubble on an airfoil,[18] flow around a flapping wing,[31] and flow around an adherent red cell.[32] In scanning PIV, a light sheet scans the volume rapidly and a camera captures

images of the illuminated planes. Two methods of image processing were used to calculate the three components of the velocity. In the first method, the 2D images obtained from each scan were stacked together and the 3D images which included the 3D positions of particles were reconstructed. The 3D images were cross-correlated and the three components of the velocity were obtained.[33] In the second method, the available 2D images of one scan were cross-correlated with the corresponding images in the next scan. Using a standard two-component PIV algorithm, the in-plane components of velocity within the volume was measured. Using the continuity equation for incompressible fluids, the out-of-plane component of velocity can be determined. The results obtained from these two methods are presented in this chapter.

2.2 Experimental setup and procedure

2.2.1 Experimental setup and facilities

The experimental setup used for the evaporation experiments is illustrated in Figure 2-1(a). The setup consisted of a pressure controlled vacuum chamber (CU6-0275, Kurt J. Lesker) which was connected to a vacuum pump through a valve. The chamber had four glass windows that are placed perpendicularly to allow optical access to the sample. A pressure transducer (INFICON Porter, CDG020D) with an accuracy of 0.5% of the read value, which could measure absolute pressures in the range of 0–10 Torr, was installed on top of the chamber and monitored the pressure within the chamber. The pressure was controlled manually by fine adjustment of the valve. The evaporation took place in a quartz cuvette (9F-Q-10, Starna Cells) which was 45 mm high and had a rectangular cross section of 10 mm × 4 mm. The cuvette walls were optically smooth and clear which makes it suitable for PIV purposes. The cuvette was mounted in a fitted cavity inside a copper block the temperature of which was controlled by a thermoelectric cooling device (CP-031, TE Technology) and a controller (TC-36-25, TE Technology). Thermal paste was used between the tube and the copper block to enhance the heat transfer. A fine thermocouple was installed on top of the vacuum chamber to measure the temperatures in the fluids during the experiments. The thermocouple was attached to an *XYZ* manipulator and could be adjusted to reach any desired point in the liquid and vapor near the interface. The thermocouple configuration, dimensions, and temperature acquisition are discussed in detail in Chapter 3.

2.2.2 Scanning PIV setup

The schematic configuration of the scanning PIV system is depicted in Figure 2-1b. The light source for illumination was a continuous wave Nd:YAG laser (LRS-0532-PFW-02000-01, LaserGlow Technologies) which emitted green light at 532 nm and delivered an output maximum power of 2 W. Three converging lenses all having a focal length of 11.1 cm and one diverging lens with a focal length of 6.5 cm were used to generate a narrow laser beam. The approximate distances between the lenses, laser, and the cuvette are given in Figure 2-1b. The laser beam was converted to a scanning laser sheet by being reflected through two orthogonal mirrors. The moving mirrors were controlled by two waveforms produced by a function generator (AFG 3022B, Tektronix Inc.). Further details on how the laser beam was converted to a moving laser sheet will be provided in the following sections. For recording the images of illuminated particles, a CCD camera (sp-5000M, JAI Inc.) which was capable of taking images at up to 134 frames per second was utilized. The camera was triggered by a TTL signal from the function generator.

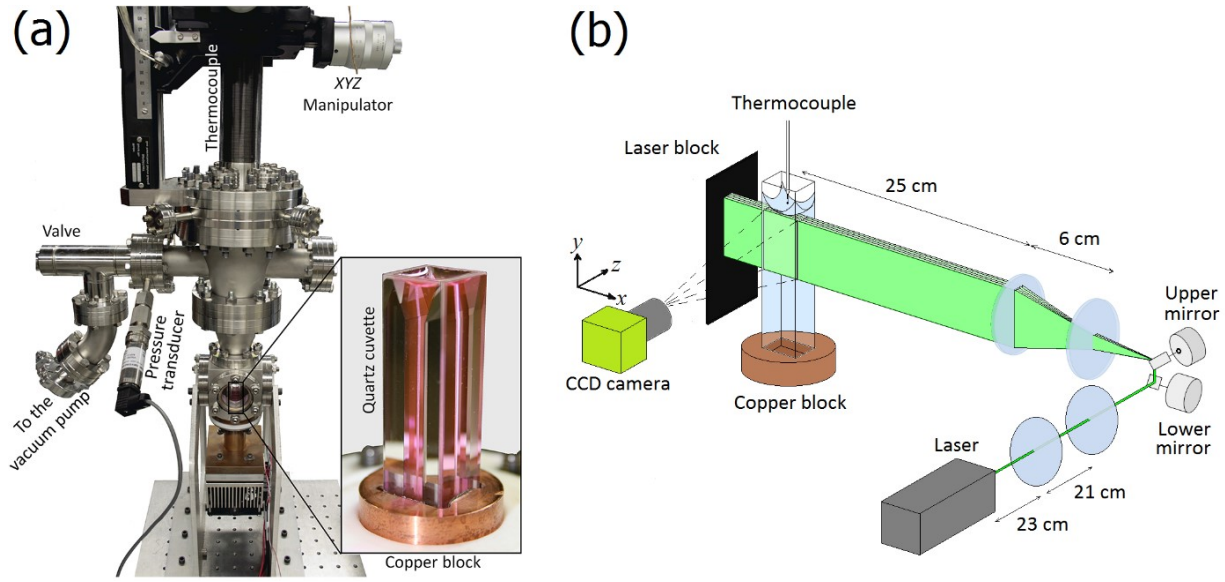

Figure 2-1 The experimental setup, (a) The vacuum chamber and other components used in evaporation experiments. The cuvette and copper block are magnified to enhance small details. (b) Schematic diagram of the scanning PIV experiment. The cuvette and optics are magnified for clarity. The distances between the parts are not to scale.

2.2.3 Material preparation for the scanning PIV

To prepare the suspension for a PIV experiment, one drop of a highly concentrated particle solution which contained 2% V/V of 2.0 μm solid fluorescent microspheres (Fluoro-Max R0200, Thermo Scientific) was mixed with 40 ml of distilled and deionized water. The suspension was mixed by shaking gently for a few minutes to achieve a uniform dilute suspension. Since the experiment was performed at a very low pressure (~ 200 Pa), the formation of gas bubbles in the liquid would confound the imaging. Therefore, the suspension was initially degassed in a vacuum jar for 15 minutes before being placed in the vacuum chamber. The cuvette was placed in a fitted cavity on the top of the copper block. The orientation of the cuvette was such that the wider side (10 mm wide wall) faced the camera. The pressure in the chamber was decreased gradually by manipulating the valve occasionally to remove the remaining dissolved gas from the liquid. The system was allowed to run for almost an hour so that the temperature of the liquid became stabilized and the system reached a pseudo steady-state. This was checked by measuring the

temperature at the center bottom of the field of view. When this condition was fulfilled, the investigation of the velocity field with PIV would begin.

2.2.4 Moving light sheet and data recording

The moving laser sheet was created by reflecting the narrowed laser beam through two orthogonal mirrors, which were connected to a galvanometer (Cambridge Technologies, 6210H, Lexington, MA). Two separate waveforms produced by the function generator controlled the oscillation of the mirrors. Figure 2-2 shows the waveforms and the timing diagram of control signals. The signal generated by channel 1 (Ch 1) consisted of many triangle functions which occurred at a high frequency (1250 Hz). This waveform controlled the position of the upper mirror and moved the reflected beam coming from the lower mirror up and down quickly. This way, the laser beam was seen as a light sheet by the camera. Each triangle in this waveform corresponds to two complete sweeps of the laser beam in the vertical direction (y). This leads to illuminating the in-plane particles during the period that the camera's shutter is open, making them visible to the camera.

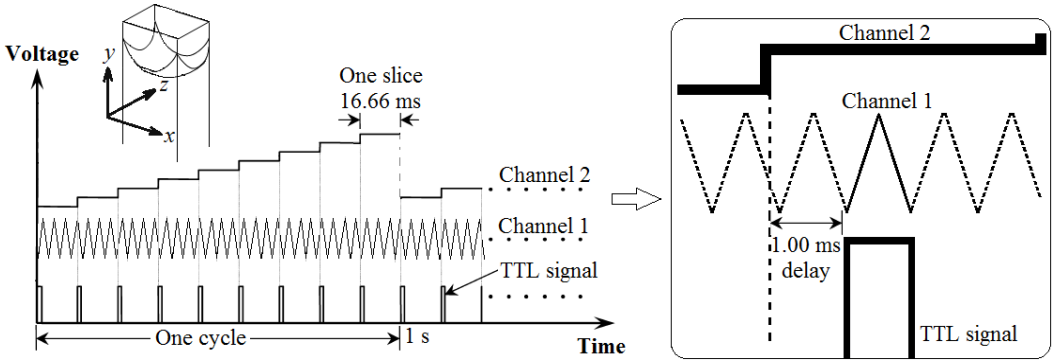

Figure 2-2 The timing diagram of control signals to trigger the camera in sync with the moving mirrors.

The waveform produced by channel 2 (Ch 2) of the function generator consisted of 60 successive rising step functions which was repeated once per second. This waveform controlled the orientation of the lower mirror and moved the laser beam in the depth of the liquid (z-direction). Each step corresponded to one step of the light sheet and the total 60 steps corresponded to one complete scan of the volume. At the end of this waveform, the light sheet would jump to its initial position for performing the next scan. A TTL signal from Ch 3 which was synchronized to Ch 2

triggered the camera. This led the camera to capture one image at each laser sheet scan. To make sure that the camera captured the images while the light sheet was not moving, a short delay of 1.00 ms between the TTL signals of Ch 3 and the step signals of Ch 2 was applied.

2.2.5 Calibration of the camera

To capture images of particles with a high magnification while keeping the particles in focus as the light sheet went far from the camera, a 60 mm SLR lens and three lens extension tubes were attached to the camera. This combination delivered a field of view (FOV) of 10.1 mm × 8.1 mm. An important concern when the images are taken at different distances from a single camera while the particles remain in focus is the change in magnification of the images. In this study, calibration of the closest/furthest images to/from the camera showed that the calibration factor varies between 253.2 pixels/mm and 255.1 pixel/mm which only corresponds to a maximum of 0.7% change in the magnification. Here, this small change was neglected and scaling of the images was not performed.

Another issue that should be dealt with is determination of the depth of the volume that was scanned by the light sheet. This was approximately obtained by performing a calibration and converting the corresponding voltage produced from Ch 2 of the function generator to distance in millimeters. Remember that the evaporation experiments needed an hour to reach a pseudo steady-state. During this period, the particles on the interface tended to move toward the contact lines and deposited on the side walls as the interface moved down (see Figure 2-3).

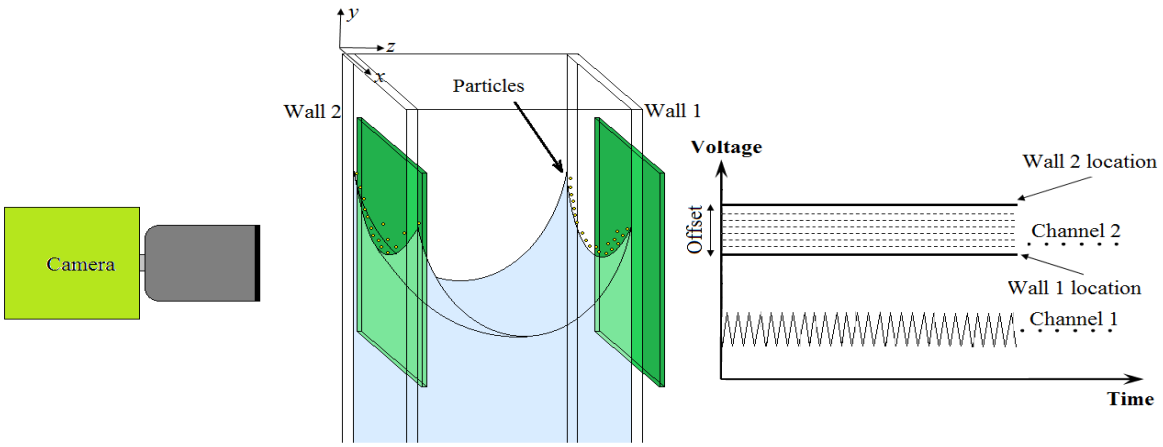

Figure 2-3 Calibration of the camera and measurement of the depth in which PIV is performed.

For performing a calibration, a constant voltage waveform was introduced to Ch 2 which resulted in generating a stagnant light sheet. The camera was set to the record mode at a maximum frame rate to observe the flow field and the laser operating at its maximum power. Starting from outside of the cuvette, the light sheet was manually adjusted to the edge of the cuvette by increasing the offset of the Ch 2 waveform in the function generator. As the particles on the wall appeared, the offset was recorded. The offset was further increased until the particles on the second wall appeared. Knowing the cuvette's depth (4 mm) and subtracting the two offsets, the calibration factor which converted the voltage of Ch 2 waveform to the distance in millimeters could be obtained. As a result, the thickness of the volume within which the scanning PIV was performed could be calculated. In addition, by knowing this calibration factor (voltage to millimeters), the laser sheet thickness could be approximated. The stagnant light sheet was approached to the first wall and passed the wall. The difference in Ch 2 offsets when the particles on one wall appeared and disappeared can give an approximation of the light sheet thickness by using the calibration factor stated above. The light sheet thickness obtained in this study was ~ 120 ± 20 μm.

2.2.6 Data processing

Two different methods of determining all three components of the velocity (u,v,w) are presented in this chapter. Figure 2-4 shows a schematic procedure of both methods. In the first method which can be seen in Figure 2-4a, each set of 60 images that were collected during one

scan of the volume were stacked together. This reconstructed a 3D volume which included the information about the 3D positions of the particles. By using a 3D algorithm in commercial software (DaVis 8.2, LaVision GmbH), the reconstructed volumes were cross-correlated and the average displacements of particles in x, y, and z directions in each interrogation region were calculated. The cross-correlation was performed in three passes using correlation window sizes of 24×24×24, 20×20×20, and 16×16×16 voxels with a 75% overlap. The velocity components were then determined by knowing the time between the successive scans of the volume. To get a near-instantaneous velocity vector field, the scan rate of the volume must be much faster than the characteristic velocity in the flow. Here, the scan rate is ~2000 μm/s and the maximum velocity is ~120 μm/s which was obtained in a separate experiment from a planar PIV at the center plane where the third velocity component $w \approx 0$.

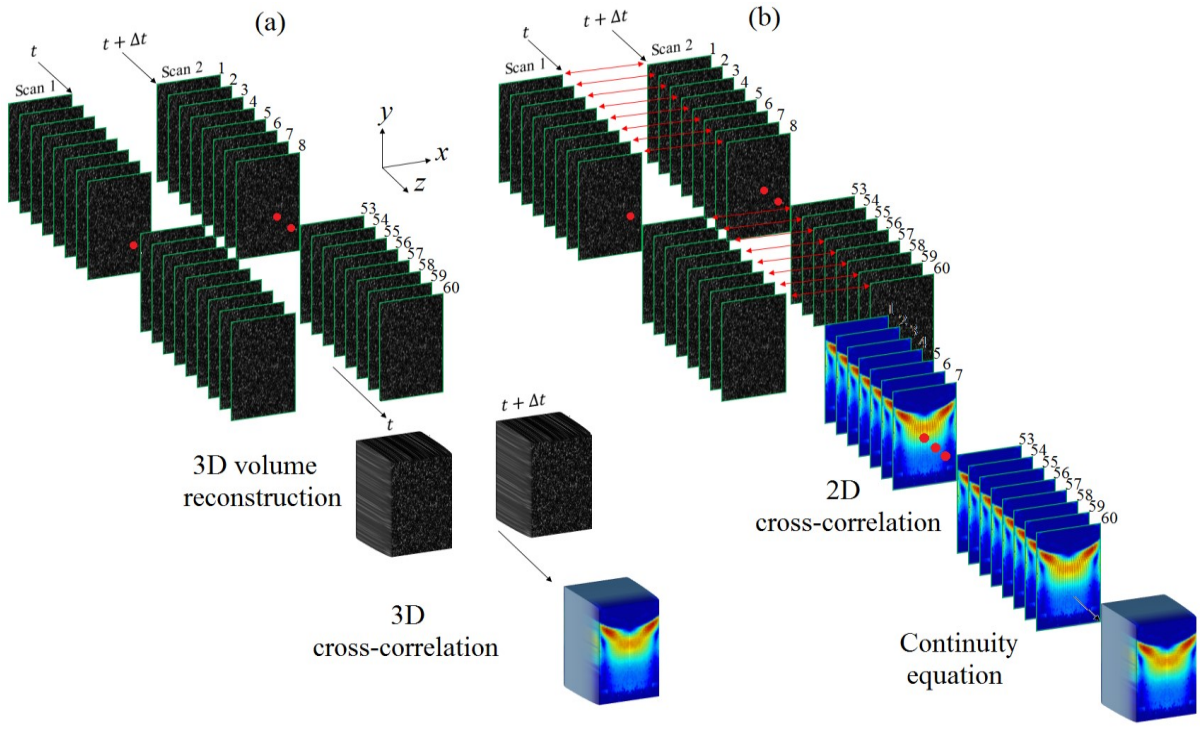

Figure 2-4 Two different methods of image processing to calculate the three components of velocity: (a) shows a 3D cross-correlation algorithm and (b) shows a 2D algorithm combined with the continuity equation.

In the second method which can be seen in Figure 2-4b, the in-plane components of the velocity were first determined from the usual planar PIV. For doing this, the available 2D images

of one scan were cross-correlated with the corresponding images in the next scan which was taken 1 sec later and the in-plane velocity components (u and v) in all 60 planes were obtained using a standard two-component PIV algorithm (DaVis 8.2, LaVision GmbH). The out-of-plane component, w, was then calculated using the continuity equation for incompressible liquids which gives the partial derivative of w in the z direction:

$$\frac{\partial w}{\partial z} = -\left(\frac{\partial u}{\partial x} + \frac{\partial v}{\partial y}\right). \tag{2-1}$$

The above differential equation may be solved numerically since the numerical values of u and v at discrete points in the volume are known. In this work, first and second order finite difference schemes were utilized to calculate the derivatives and the results are compared in the following section. The discretized equations for calculating the first and second order derivatives are summarized in Table 2-1.

Table 2-1 Discretized equations obtained from the 1st and 2nd order finite difference schemes.

1st order		2nd order	
$\left(\frac{\partial u}{\partial x}\right)_{i,j,k} = \frac{-u_{i,j,k} + u_{i+1,j,k}}{\Delta x}$	(2-2)	$\left(\frac{\partial u}{\partial x}\right)_{i,j,k} = \frac{-(3/2)u_{i,j,k} + 2u_{i+1,j,k} - (1/2)u_{i+2,j,k}}{\Delta x}$	(2-3)
$\left(\frac{\partial v}{\partial y}\right)_{i,j,k} = \frac{-v_{i,j,k} + v_{i,j+1,k}}{\Delta y}$	(2-4)	$\left(\frac{\partial v}{\partial y}\right)_{i,j,k} = \frac{-(3/2)v_{i,j,k} + 2v_{i,j+1,k} - (1/2)v_{i,j+2,k}}{\Delta y}$	(2-5)
$\left(\frac{\partial w}{\partial z}\right)_{i,j,k} = \frac{-w_{i,j,k} + w_{i,j,k+1}}{\Delta z}$	(2-6)	$\left(\frac{\partial w}{\partial z}\right)_{i,j,k} = \frac{-(3/2)w_{i,j,k} + 2w_{i,j,k+1} - (1/2)w_{i,j,k+2}}{\Delta z}$	(2-7)

The indices i and j refer to the discretization in x and y directions respectively, and index k shows the plane number. Since the values of u and v on all 60 planes are already obtained from the planar PIV, the partial derivative of u in the x direction ($\partial u/\partial x$), and v in the y direction ($\partial v/\partial y$) on all planes can be calculated from eq (2-2) and eq (2-4) (or eq (2-3) and (2-5)) in Table 2-1. Using eq (2-1), the partial derivatives of w in the z direction ($\partial w/\partial z$) are obtained. To be able to calculate the values of w in all planes, a boundary condition is required. The boundary values of w were obtained from a linear extrapolation toward the solid wall:

$$w_{i,j,1} = w_{wall} + \left(\frac{\partial w}{\partial z}\right)_{i,j,1} (\Delta z)_0, \tag{2-8}$$

where $w_{i,j,wall}$ is the out of plane component of velocity at the solid wall which is assumed to be zero according to the no-slip boundary condition, $(\partial w/\partial z)_{i,j,1}$ is the derivative in the first plane, and $(\Delta z)_0$ is the distance from the center of the first plane to the wall. It should be noted that if the second order scheme is used, the values of *w* cannot be calculated explicitly and a set of equations that contains 59 unknowns should be solved at each *x* and *y*.

2.3 Results and discussion

The 3D velocity vectors obtained from both methods are illustrated in Figure 2-5. The scanning PIV was performed only in half of the volume due to the limitation in bringing all of the cuvette's depth into focus. The flow in the cuvette, however, seems almost symmetric according to the velocity vectors obtained from both methods.

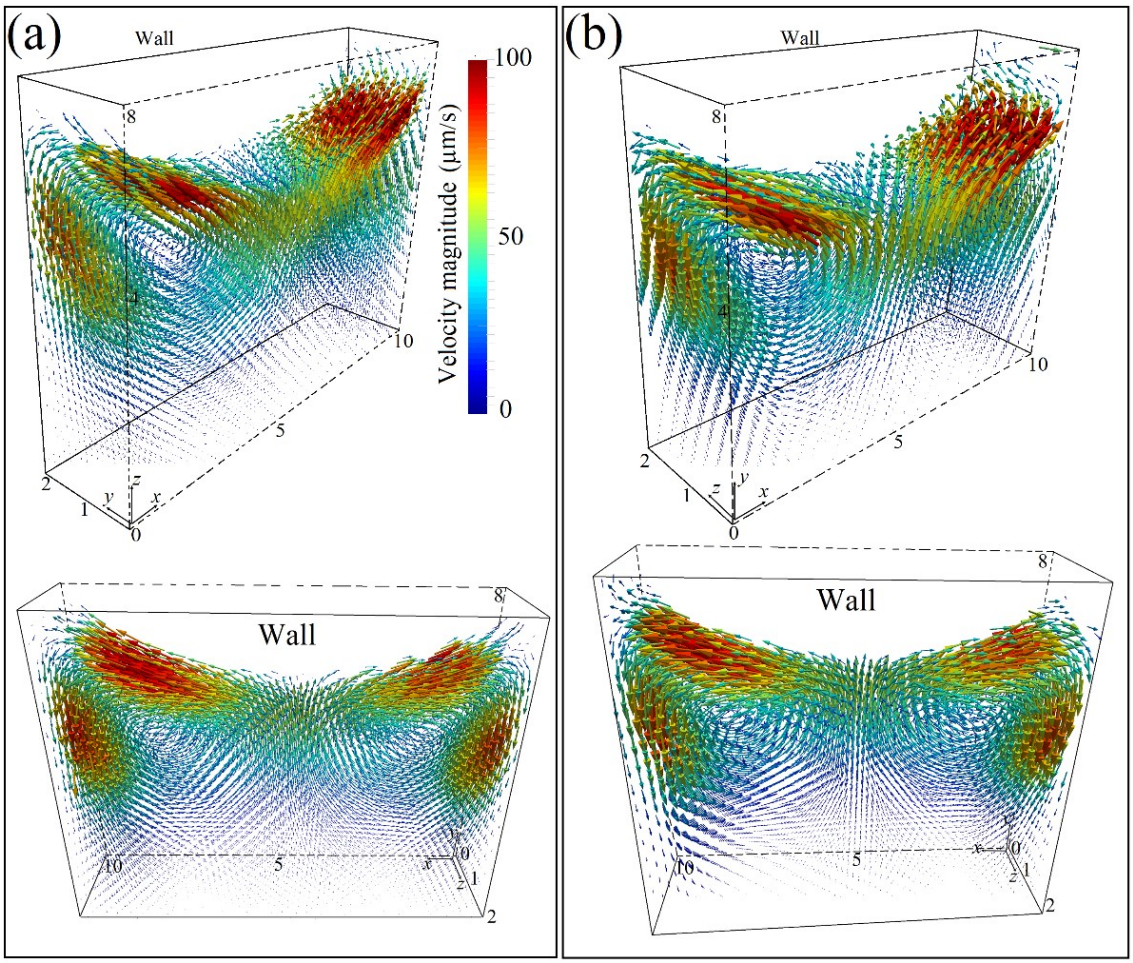

Figure 2-5 3D illustration of velocity vectors obtained from (a) a 3D algorithm and (b) 2D PIV combined with the continuity equation.

For a clear illustration, every 120th vector in Figure 2-5a and every 245th vector in Figure 2-5b are shown. The color and the arrow size show the local velocity magnitude. The arrows with a red color show the highest velocity regions, which are located close to the interface and near the corners where the walls meet. The 3D velocity field reveals the existence of a torus shaped vortex below the evaporating meniscus.

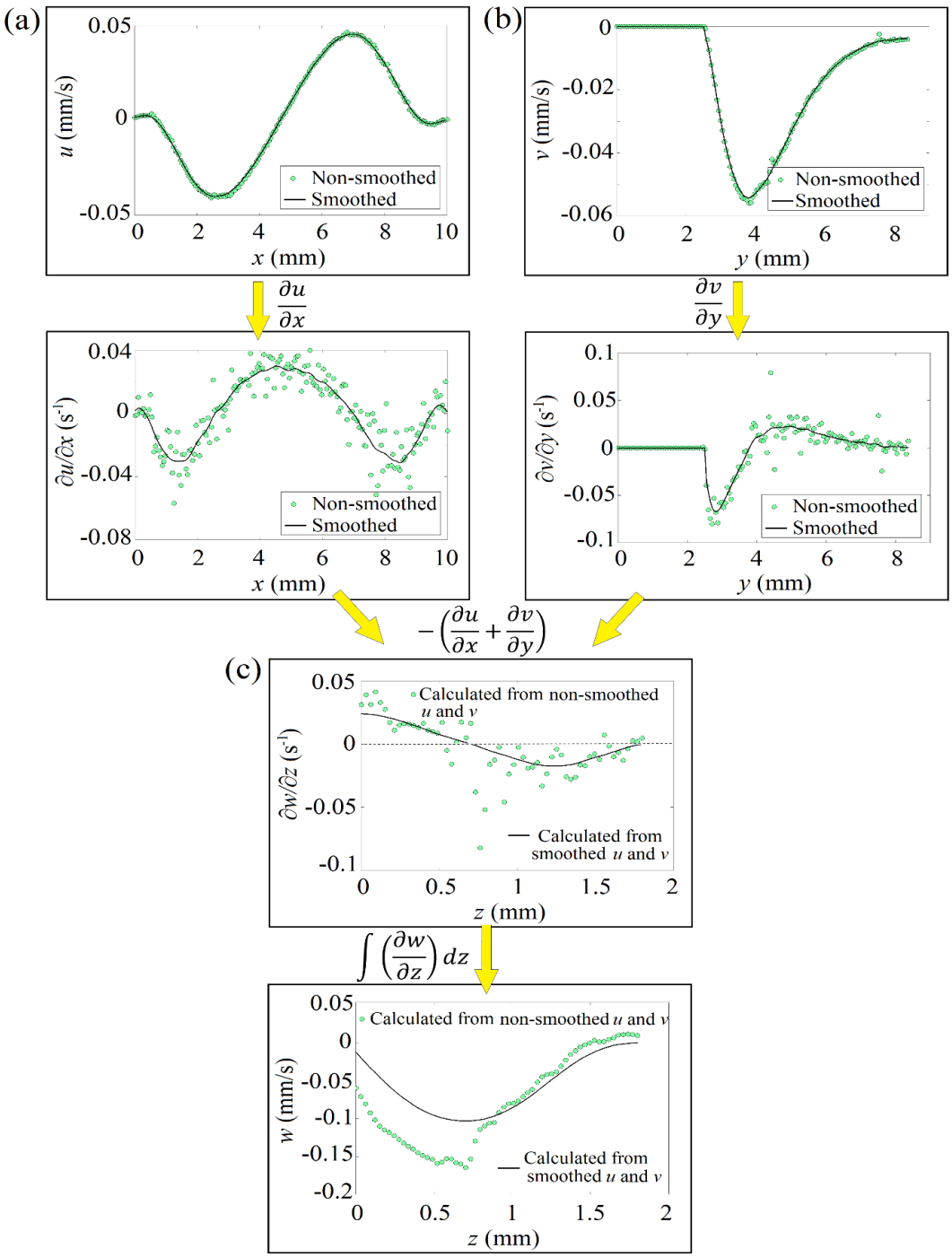

Figure 2-6 The effect of the smoothing of in-plane velocity components, u and v, on the calculated velocity component w from eq (2-2). (a) is shown at y = 5 mm and z = 0.3 mm. (b) is shown at x = 5 mm and z = 0.3 mm (c) is shown at x = 5 mm and y = 5 mm.

A typical procedure by which the third component of the velocity w was calculated from the results of 2D PIV is shown in Figure 2-6. To get consistent gradients $(\partial u/\partial x, \partial v/\partial y, \partial w/\partial z)$ to be used in the continuity equation, the in-plane velocity data should be smoothed. This was performed using a pre-defined smoothing function in MATLAB (MATLAB R2015a, The Mathworks Inc.). Figure 2-6 shows the smoothed and non-smoothed data and how this step affected the final result. As it appears from the figure, smoothing does not change the in-plane velocities (u and v) significantly. However, it has a notable effect on the calculated gradients, leading to obtaining remarkably different results. For instance, the value of the partial derivative of the out-of-plane component of velocity in the z-direction $(\partial w/\partial z)$ which is calculated from the non-smoothed velocities, has a relatively large negative value at z = 0.75 mm (Figure 2-6c). This results in a sudden drop in w since a large negative value is added to the previous value of w according to eq (2-6) (or eq (2-7) for 2nd order), and makes w deviate from the smoothed results.

A comparison between the out-of-plane components of the velocity obtained from the 3D algorithm with that calculated from the continuity equation is shown in Figure 2-7. As can be seen, the results of both methods are in good agreement. Another point that can be inferred from the figure is that using the second order finite difference scheme to discretize the derivatives does not make any significant difference in calculating w. Therefore, the first order finite difference scheme which is mathematically simpler, as it calculates w explicitly, and is computationally less expensive was used in this study.

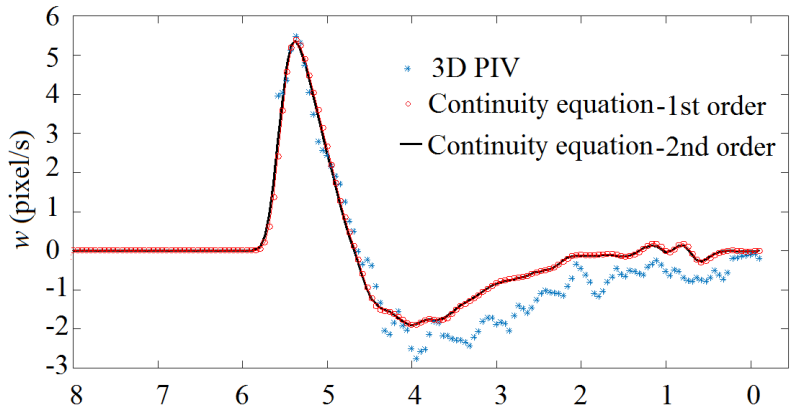

Figure 2-7 Comparison between the out-of-plane velocities w calculated from the continuity equation and the 3D PIV.

Figure 2-8 shows the effect of selecting the boundary condition on the out-of-plane velocity. Referring to Figure 2-5, the 3D velocity vectors indicate that the flow of the liquid looks almost symmetric. This means that the out-of-plane velocities at the center plane can be assumed to be zero (*i.e.* $w_{i,j,60} = 0$). The calculation of w from the continuity equation was repeated assuming $w_{i,j,60} = 0$ and results on three typical planes are shown in Figure 2-8. As can be seen from the figure, the values of w obtained by assuming a no-slip boundary condition at the wall are in better agreement with those of the 3D algorithm.

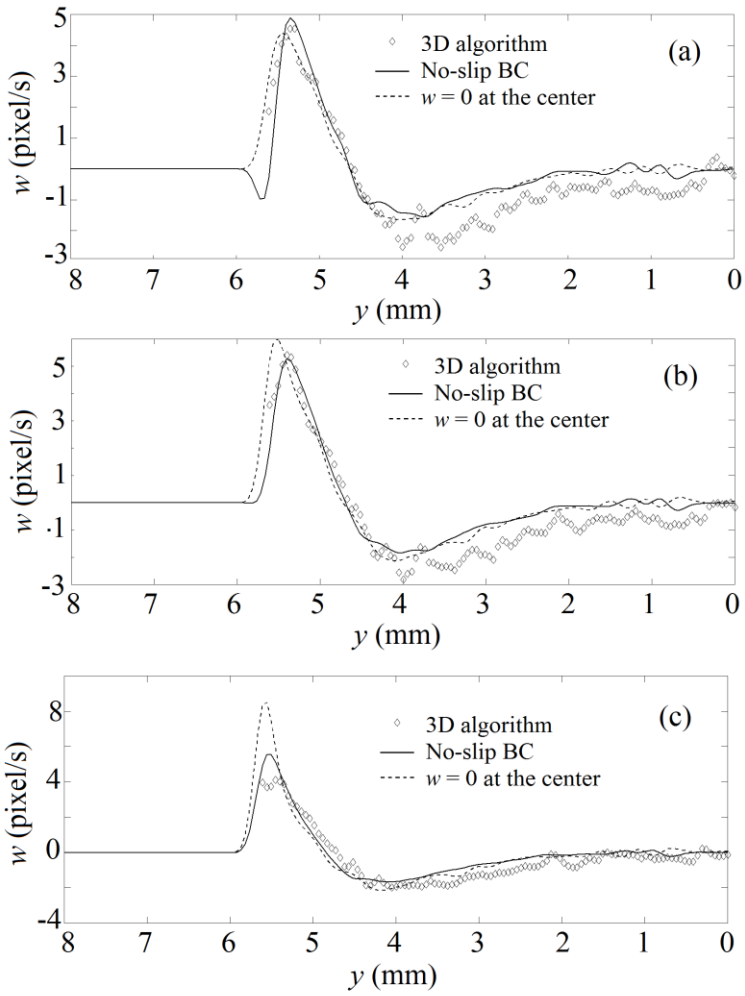

Figure 2-8 Comparison of w obtained from different boundary conditions using the continuity equation with those obtained from the 3D PIV. (a) shows w at x = 5 mm and z = 0.7 mm, (b) shows w at x = 5 mm and z = 1 mm, (a) shows w at x = 5 mm and z = 1.3 mm.

2.4 Conclusion

The 3D evaporation-driven flow beneath an evaporating meniscus was visualized and quantified using a scanning PIV technique. Two different image processing approaches were utilized to obtain the three components of the velocity within the scanned volume, one based on the cross-correlation of 3D images which were formed by stacking 2D images and using a 3D algorithm to calculate the 3D displacement of particles, and the other based on the cross-correlation of 2D images and employing the continuity equation to obtain the out-of-plane component. The

results obtained from both methods showed good agreement which gives confidence that the scanning PIV has been successfully used for the 3D representation of the velocity field in the evaporation-driven flow.

It was shown that when using the continuity equation, smoothing the in-plane velocity data improved the calculated out-of-plane velocity component. Also, both the first and the second order finite difference schemes in discretizing the derivatives gave almost the same answer. Therefore, the first order scheme is suggested due to its simplicity and a shorter computational time. The effect of boundary conditions on the calculated *w* from the continuity equation was also investigated and the results showed that the no-slip condition at the solid wall led to a better coherence of the calculated *w* with those of the 3D PIV.

2.5 References

(1) Block, M. Surface Tension as the Cause of Benard Cells and Surface Deformation in a Liquid Film. *Nature* **1956**, *178*, 650.

(2) Pearson, J. R. A. On Convection Cells Induced by Surface Tension. *J. Fluid Mech.* **1958**, *4* (5), 489–500.

(3) Bénard, H. Les Tourbillons Cellulaires dans une Nappe Liquide. - Méthodes Optiques D'observation et D'enregistrement. *J. Phys. Theor. Appl., 10* (1), **1901,** 254–266.

(4) Rayleigh, Lord. LIX. On Convection Currents in a Horizontal Layer of Fluid, When the Higher Temperature is on the under Side. *Philos. Mag. Ser. 6* **1916**, *32* (192), 529–546.

(5) Pan, X.; Jin, W.; Liu, Y.; Ai, F. Effect of Surface Tension-Driven Flow on BaB_2O_4 Crystal Growth from High Temperature Melt-Solution. *Cryst. Res. Technol.* **2008**, *43* (2), 152–156.

(6) Sutter, T.; Kim, N.; Kyu, T.; Golovaty, D. Crystal Nucleation and Motion in an Undercooled Binary Solution. *Curr. Opin. Chem. Eng.* **2015**, *7*, 1–5.

(7) Savino, R.; di Francescantonio, N.; Fortezza, R.; Abe, Y. Heat Pipes with Binary Mixtures and Inverse Marangoni Effects for Microgravity Applications. *Acta Astronaut.* **2007**, *61* (1–6), 16–26.

(8) di Francescantonio, N.; Savino, R.; Abe, Y. New Alcohol Solutions for Heat Pipes: Marangoni Effect and Heat Transfer Enhancement. *Int. J. Heat Mass Transf.* **2008**, *51* (25–26), 6199–6207.

(9) Cai, Y.; Newby, B. M. Z. Marangoni Flow-Induced Self-Assembly of Hexagonal and

Stripelike Nanoparticle Patterns. *J. Am. Chem. Soc.* **2008**, *130* (19), 6076–6077.

(10) Bhardwaj, R.; Fang, X.; Somasundaran, P.; Attinger, D. Self-Assembly of Colloidal Particles from Evaporating Droplets: Role of DLVO Interactions and Proposition of a Phase Diagram. *Langmuir* **2010**, *26* (11), 7833–7842.

(11) Xiao-Hu, Y.; Xi, C. Importance of Marangoni Convection in Laser Full-Penetration Welding. *Chinese Phys. Lett.* **2002**, *19* (6), 788–790.

(12) Lu, S.; Fujii, H.; Nogi, K. Marangoni Convection and Weld Shape Variations in Ar-O_2 and Ar-CO_2 Shielded GTA Welding. *Mater. Sci. Eng. A* **2004**, *380* (1), 290–297.

(13) Ganzevles, F. L. A.; Van Der Geld, C. W. M. Marangoni Convection in Binary Drops in Air Cooled from below. *Int. J. Heat Mass Transf.* **1998**, *41* (10), 1293–1301.

(14) Ghasemi, H.; Ward, C. A. Energy Transport by Thermocapillary Convection during Sessile-Water-Droplet Evaporation. *Phys. Rev. Lett.* **2010**, *105* (13), 136102.

(15) Pereira, F.; Gharib, M.; Dabiri, D.; Modarress, D. Defocusing Digital Particle Image Velocimetry: A 3-Component 3-Dimensional DPIV Measurement Technique. Application to Bubbly Flows. *Exp. Fluids* **2000**, *29* (7), S078–S084.

(16) Elsinga, G. E.; Scarano, F.; Wieneke, B.; Van Oudheusden, B. W. Tomographic Particle Image Velocimetry. *Exp. Fluids* **2006**, *41* (6), 933–947.

(17) Sheng, J.; Malkiel, E.; Katz, J. Using Digital Holographic Microscopy for Simultaneous Measurements of 3D near Wall Velocity and Wall Shear Stress in a Turbulent Boundary Layer. *Exp. Fluids* **2008**, *45* (6), 1023–1035.

(18) Burgmann, S.; Schröder, W. Investigation of the Vortex Induced Unsteadiness of a Separation Bubble via Time-Resolved and Scanning PIV Measurements. *Exp. Fluids* **2008**, *45* (4), 675–691.

(19) Gao, Q.; Wang, H.; Shen, G. Review on Development of Volumetric Particle Image Velocimetry. *Chinese Sci. Bull.* **2013**, *58* (36), 4541–4556.

(20) Wereley, S. T.; Meinhart, C. D. Recent Advances in Micro-Particle Image Velocimetry. *Annu. Rev. Fluid Mech.* **2010**, *42* (1), 557–576.

(21) Ward, C. A.; Duan, F. Turbulent Transition of Thermocapillary Flow Induced by Water Evaporation. *Phys. Rev. E* **2004**, *69* (5), 56308.

(22) Song, X.; Nobes, D. S. Experimental Investigation of Evaporation-Induced Convection in Water Using Laser Based Measurement Techniques. *Exp. Therm. Fluid Sci.* **2011**, *35* (6), 910–919.

(23) Christy, J. R. E.; Sefiane, K.; Ebeling, J. C.; Seewald, T.; Harmand, S. Flow Measurement Using Micro-PIV and Related Temperature Distributions within Evaporating Sessile Drops of

Self-Rewetting Mixtures of 1-Pentanol and Water. In the *4th Micro and Nano Flows Conference, University College London, 7th - 10th September* **2014**.

(24) Buffone, C.; Sefiane, K.; Christy, J. R. E. Experimental Investigation of Self-Induced Thermocapillary Convection for an Evaporating Meniscus in Capillary Tubes Using Micro-Particle Image Velocimetry. *Phys. Fluids* **2005**, *17* (5), 1–18.

(25) Dhavaleswarapu, H. K.; Chamarthy, P.; Garimella, S. V; Murthy, J. Y. Experimental Investigation of Steady Buoyant-Thermocapillary Convection near an Evaporating Meniscus. *Phys. Fluids* **2007**, *19* (8), 82103.

(26) Thokchom, A. K.; Swaminathan, R.; Singh, A. Fluid Flow and Particle Dynamics Inside an Evaporating Droplet Containing Live Bacteria Displaying Chemotaxis. *Langmuir* **2014**, *30* (41), 12144–12153.

(27) Thokchom, A. K.; Gupta, A.; Jaijus, P. J.; Singh, A. Analysis of Fluid Flow and Particle Transport in Evaporating Droplets Exposed to Infrared Heating. *Int. J. Heat Mass Transf.* **2014**, *68*, 67–77.

(28) Babaie, A.; Madadkhani, S.; Stoeber, B. Evaporation-Driven Low Reynolds Number Vortices in a Cavity. *Phys. Fluids* **2014**, *26* (3), 33102.

(29) Minetti, C.; Buffone, C. Three-Dimensional Marangoni Cell in Self-Induced Evaporating Cooling Unveiled by Digital Holographic Microscopy. *Phys. Rev. E - Stat. Nonlinear, Soft Matter Phys.* **2014**, *89* (1), 1–6.

(30) Brücker, C. Digital-Particle-Image-Velocimetry (DPIV) in a Scanning Light-Sheet: 3D Starting Flow around a Short Cylinder. *Exp. Fluids* **1995**, *19* (4), 255–263.

(31) David, L.; Jardin, T.; Braud, P.; Farcy, A. Time-Resolved Scanning Tomography PIV Measurements around a Flapping Wing. *Exp. Fluids* **2012**, *52* (4), 857–864.

(32) Pommer, M.; Meinhart, C. Shear-Stress Distributions Surrounding Individual Adherent Red Cells in a Microchannel Measured Using Micro-PIV. In *Proceedings of the 6th International Symposium on Particle Image Velocimetry*; 2005; pp 21–23.

(33) Kazemi, M. A.; Elliott, J. A. W.; Nobes, D. S. A 3D Flow Visualization in Evaporation of Water from a Meniscus at Low Pressures. In *The 10th Pacific Symposium on Flow Visualization and Image Processing, Naples, Italy, 15-18 June*; 2015.

Chapter 3: Evaporation of Water from a Meniscus in a Cylindrical Cuvette[‡]

In this chapter, a mathematical model is developed to describe the coupling of the heat, mass, and momentum transfer in the fluids with the transport phenomena at the interface. The model is used to understand the experimentally obtained velocity field in the liquid and temperature profiles in the liquid and vapor, in evaporation from a concave meniscus for various vacuum pressures. By using the model, we have shown that an opposing buoyancy flow suppressed the thermocapillary flow in the liquid during evaporation at low pressures in our experiments. As such, in the absence of thermocapillary convection, the evaporation is controlled by heat transfer to the interface, and the predicted behavior of the system is independent of choosing between the existing theoretical expressions for evaporation flux. Furthermore, we investigated the temperature discontinuity at the interface and confirmed that the discontinuity strongly depends on the heat flux from the vapor side, which depends on the geometrical shape of the interface.

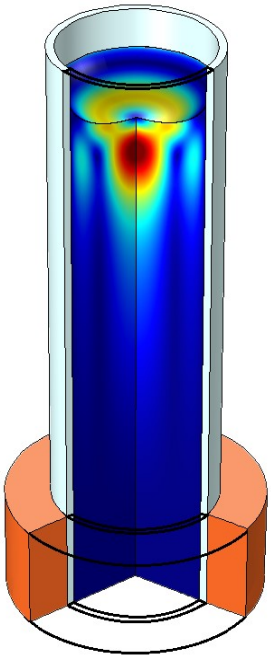

Graphical Abstract
Chapter 3

3.1 Introduction

Evaporation of a liquid is a fundamental phenomenon which has attracted a considerable amount of research attention as it pertains to a wide range of industrial and biological applications such as printing, particle self-assembly, electronic device cooling, drug discovery, and deposition of DNA/RNA microarrays. Despite extensive studies, this phenomenon has not been well understood mostly due to the complex nature of the evaporation process which involves intricate

[‡] This chapter with minor modifications has been published as Kazemi, M. A.; Nobes, D. S.; Elliott, J. A. W. Experimental and Numerical Study of the Evaporation of Water at Low Pressures. *Langmuir* 2017, 33 (18), 4578–4591.

couplings between hydrodynamic effects in the bulk fluids and transport phenomena at the liquid–vapor interface. The technical limitations of the current experimental techniques and devices is also another reason. The vast majority of the studies in this field have been devoted to the evaporation of a sessile droplet into a noncondensable gas such as air. Motivated by observation of the coffee ring by Deegan *et al*.[1] which was attributed to the flow pattern inside the drying drop, several studies moved toward understanding the internal flow inside a drop during evaporation.[2–5] To facilitate the analytical and numerical investigation of the flow pattern, Hu and Larson[6] derived a simple expression for the local evaporation flux based on the analytical and numerical solution of the steady-state diffusion equation for the vapor concentration in the gas phase. In addition to the flow field in the liquid, the effect of various parameters such as substrate thermal properties,[7–10] substrate wettability,[8,11,12] vapor concentration field,[13,14] and temperature field around the drop[15] on the evaporation rate have been studied extensively. Good reviews on the topic may be found in references.[16,17]

In contrast to evaporation into noncondensable gases, evaporation of a liquid into its own vapor has not received as much attention in the past. In 1999, Fang and Ward[18–20] performed a series of careful experiments on the steady-state evaporation of a water droplet into its vapor at low pressures. They measured the temperature distribution close to the evaporating surface with a 25 μm thermocouple and found that the temperature at the interface was discontinuous, and that the vapor side temperature was always greater than the liquid side temperature. The observed discontinuity was found to be as high as 7.8 °C under certain experimental conditions. In addition, they proposed a new expression describing the evaporation flux across the interface by using the statistical rate theory of interfacial transport (SRT) which relies on the transition probability concept of quantum mechanics and the Boltzmann definition of entropy. Several studies were carried out subsequently to investigate the evaporation of water in a vacuum and to examine the accuracy of the proposed expression. Ward and Stanga[21] studied the evaporation and condensation of deionized water in a vacuum chamber. By measuring the temperature profile on the vertical centerline of the drop, in addition to confirming the temperature discontinuity at the interface, they noticed the existence of a uniform temperature layer in the liquid within 0.5 mm below the interface. They attributed this layer to the mixing produced by a thermocapillary flow near the surface. Ward and Duan[22] repeated the same experiments, but this time, they measured the

interfacial liquid velocity at one point using a cantilevered probe that was inserted 40 μm into the liquid. By performing an energy balance at the interface, they concluded that the thermal conduction from the vapor and liquid to the interface could not provide sufficient energy for evaporation. However, by taking into account the convective energy transport at the interface which was calculated from the measured interfacial flow, the energy balance at the interface was satisfied. Meanwhile, the authors of references[18,23,24] did not notice a thermocapillary flow and a uniform temperature layer during evaporation of water in their low pressure experiments, and they found that the conduction heat transfer to the interface solely provided the energy required for evaporation. Song and Nobes[25] studied the flow field during evaporation of a suspension of water in a rectangular cuvette. They used particle image velocimetry (PIV) to quantify the velocity field in the center plane. Their PIV results revealed two large counter-rotating vortices below the meniscus. They also measured the temperature field in the same plane by temperature planar laser induced fluorescence (temp-PLIF). However, their measurements did not cover the temperatures very close to and on the interface.

There are few numerical studies on the evaporation of a liquid into its vapor. Most have simplified the physics involved in the evaporation process. For instance, Kuznetzov and Sitnikov[26] studied the evaporation of water in a heat pipe. They did not consider the interfacial resistances against evaporation in their model, nor did they take the thermocapillary and buoyancy effects into account. Kirillov *et al*.[27] studied the evaporation and condensation of liquids in an evaporator but they ignored the thermocapillary effects, buoyancy effects, and heat transfer to the interface. Qin *et al*.[28] performed a numerical simulation of the evaporation of a thin layer of a silicon oil into its vapor which was confined in a small cavity. They imposed two different temperatures on the vertical walls of the cavity. They compared their results with the case of evaporation into the air at atmospheric pressure[29] and found that the thermocapillary flow that was present in the liquid while it was evaporating into the air was completely suppressed in the case of evaporation into the pure vapor, even when a large horizontal temperature difference (30 °C) was applied. However, in their simulations they neglected the heat transfer to the interface by the thermocapillary mechanism.

Although all the studies described above provide valuable insight into the problem of evaporation of a liquid into its own vapor and have led to achieving significant advances in the

field, further theoretical and experimental studies are needed to understand these findings. Generally speaking, the studies which investigated the evaporation into vapor by relying upon the measurement of temperatures with a thermocouple near the interface and calculation of the local heat fluxes from the measured temperature profiles (despite the fact that they are using an intrusive technique) lack information on the velocity distribution in the liquid and vapor (especially that of the liquid at the interface, which plays a key role in the energy transport to the interface). Conversely, those studies which have investigated the flow field did not perform an experimental measurement of the temperature at the interface. Therefore, in our opinion, a more comprehensive study which includes a velocity measurement in the liquid, along with a temperature measurement near the interface is needed. Accordingly, we have carried out an experimental and theoretical study on unsteady-state evaporation of water into its vapor at low pressure. In the theoretical section, we develop a mathematical model of the system which accounts for mass, momentum, and heat transport in the liquid and vapor, as well as the phase change at the interface. The buoyancy effects in both phases and the thermocapillary effects, which are usually neglected in the thermal boundary condition at the interface, are both taken into account. Two existing theoretical expressions for evaporation flux which are derived from the kinetic theory of gases (KTG) and statistical rate theory (SRT) are investigated to describe the mass transfer across the interface. Experimentally, we measured the velocity field in the center plane of the evaporating water using PIV. Moreover, the temperature distribution on the vertical centerline in both the liquid and vapor was measured with a fine thermocouple. Once the simulation results showed good agreement with the experimental results, the model is used to reveal some facts about the evaporation phenomenon, which would be difficult to understand through the experiments alone.

3.2 Experimental investigation

A series of evaporation experiments on the evaporation of water at low pressures was carried out to understand the phenomena near the evaporating interface. In this section, the details of the experimental setup and velocity and temperature measurement techniques are presented.

3.2.1 Experimental apparatus and procedure

The experimental setup is described in Chapter 2 and is shown schematically in Figure 3-1. In this study, however, instead of a rectangular cuvette, a cylindrical borosilicate glass tube (514A-1PP-7, Wilmad) with an inner diameter of 11.050 ± 0.013 mm, outer diameter of 12.065 ± 0.008 mm, and height of 45.14 mm was chosen as the container to hold the liquid. This precision tube provided a smooth and consistent wall making it well suited for PIV. A cylindrical tube was selected rather than a rectangular one to simplify the system from three-dimensional to a two-dimensional axisymmetric problem which was much easier for the numerical study. The validity of the axisymmetric simplification was confirmed by obtaining a quite symmetric flow field in the PIV experiments at all pressures. The inside wall of the tube was hydrophilic and provided a partially-wetting surface (contact angle $\theta \approx 26°$) for water. To measure the temperature profiles in the liquid and vapor near the interface, a fine wire thermocouple, with a wire diameter of 25 μm and a spherical bead diameter of 50 μm was attached to an *XYZ* manipulator and installed at the top of the chamber. The thermocouple could access most of the liquid volume by being moved by the manipulator.

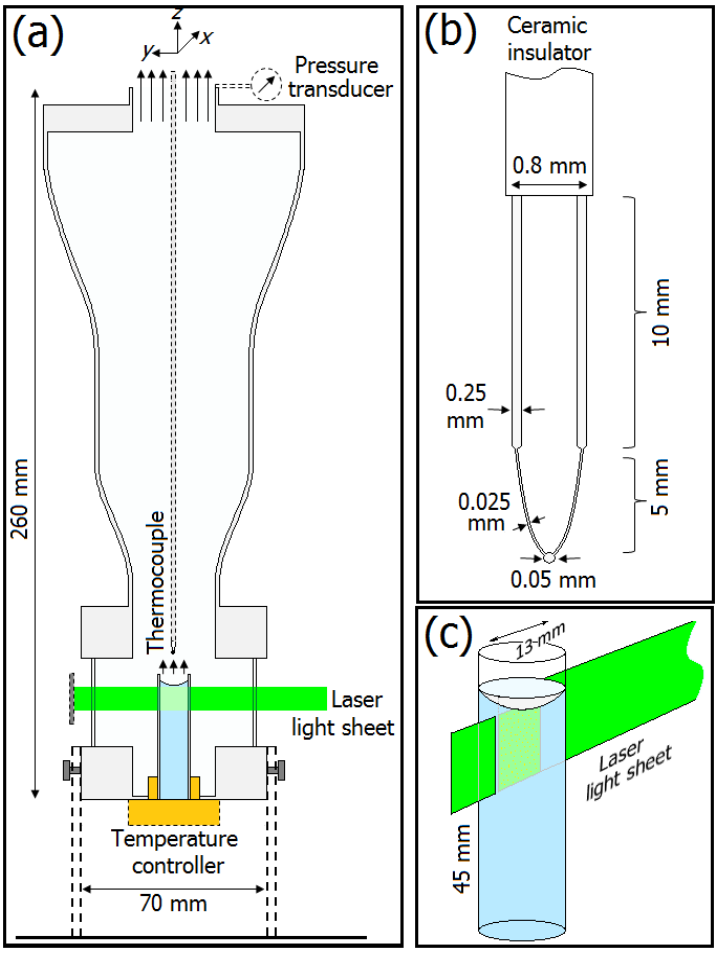

Figure 3-1 Schematic illustration of the experimental setup, (b) the thermocouple shape and dimensions, and (c) the illuminated center plane in which the PIV experiments were carried out.

3.2.2 Velocity measurement

In order to quantify the flow field in the liquid, particle image velocimetry (PIV) was utilized. The PIV experiments in the cylindrical tube were similar to those in performed the rectangular cuvette described in Chapter 2, with the difference being that the laser sheet was fixed at the center of the tube and didn't move during the PIV experiments. The suspension for the PIV experiments in the cylindrical tube was prepared by adding one drop of a concentrated particle solution to 100 ml of distilled, deionized water. The images were captured by the camera with a time interval of 1.00 s between successive images. The magnification factor of the recorded images was 190 pixel/mm resulting in a field of view of 13.44 mm × 10.75 mm. The images were corrected to

eliminate the cylindrical distortion effects using custom code (MATLAB, The MathWorks Inc.). The custom code by which the images were corrected is provided in Appendix A. The reference image was obtained by taking an image of a target that was placed in a filled tube. The sequential corrected images were analyzed using a double-frame cross-correlation algorithm in commercial software (DaVis 8.2, LaVision GmbH). The cross-correlation was performed in three passes, starting from a 64×64 pixel window with 50% overlap, followed by a 64×64 pixel window with 75% overlap, and finalized with a 32×32 pixel window with 75% overlap, which led to obtaining a displacement vector field with a resolution of 42 μm. Finally, the velocity vector field was calculated by dividing the displacement field by the known time interval between the images.

3.2.3 Temperature measurement

The temperatures were measured using a K-type micro-thermocouple (CHAL-001, OMEGA) with a wire size of 25.4 μm. The fine wires were welded to similar larger wires (CHAL-01, OMEGA), as shown schematically in Figure 3-1b. The bead size was approximately twice the size of the small wires ($\sim$ 50 μm), which was approximated by taking an image with the calibrated camera. The larger wires were passed through a ceramic insulator to reduce heat transfer from the ambient surroundings to the wires. To calibrate the thermocouple at temperatures below 0 °C, the measuring junction was placed into a mixture of ice, sodium chloride, and water. The calibration cell was insulated to minimize heat transfer to the cell. By changing the concentration of the sodium chloride, different values of negative temperatures could be achieved. To calibrate the thermocouple at temperatures above 0 °C, a water bath which could control the temperature was used. During the calibration procedure as well as the temperature measurement experiments, the cold junctions were placed in an ice point cell (TRC III Ice Point Reference Cell, OMEGA) to maintain the cold junction temperature at 0 °C. The thermocouple was calibrated in the calibrating liquid against a reference platinum resistance thermometer (935-14-95H, Isothermal Technology Ltd.) which provided an accuracy of better than 0.02 °C in the range of −50 °C to 50 °C. The readings of the thermocouple were plotted against those of the reference probe and a linear function was fitted to the data with a correlation coefficient of almost one ($R^2 = 0.99996$). Deviations of the thermocouple readings from the fitted line were found to be less than 0.03 °C. Therefore, by considering the uncertainties associated with the reference probe (± 0.02 °C) and the linear fit (±

0.03 °C), the absolute errors in the temperature measurements did not exceed ± 0.05 °C. The calibration curve of the thermocouple is shown in Appendix B.

For the temperature measurement experiments, a clean cuvette was filled with distilled, deionized water and was initially degassed in the vacuum jar for 15 minutes. Then it was moved to the vacuum chamber. The pressure in the chamber was decreased gradually by manipulating the angle valve to remove the remaining dissolved gas from the liquid. After the temperature of the liquid at the interface showed that the system had reached a pseudo steady-state (the temperature shown by the thermocouple varied by less than 0.01 °C), temperature measurement began. The horizontal position of the thermocouple was adjusted to the centerline by observing the thermocouple bead through the camera with a resolution of 5μm/pixel. For reference positioning of the bead at the interface in the liquid phase, the thermocouple tip was submerged about 1 mm in the liquid. Then it was moved up toward the interface by fine movements of the thermocouple using the traverse stepper motor. When the top of the bead contacted the interface without deforming it, the position was set to zero and the automated temperature measurement would start immediately. The traverse stepper motor was programmed to move the thermocouple in 62.5 μm increments in the first 500 μm, and 625 μm increments thereafter. At each point of interest, the thermocouple stopped and 10 measurements were collected, and the results were stored in a computer. The time constants of the thermocouple in the liquid and vapor were measured experimentally and found to be 0.37s and 0.65s, respectively (see Appendix C). The thermocouple started collecting temperatures after the elapse of four-time constants, to make sure that the 10 measurements were acquired when the temperature of the junction reached a steady-state condition.

For temperature measurement in the vapor, the thermocouple was first placed very close to the interface. Since the liquid formed a concave interface, it was not possible to observe the bead at the interface. To find the position of the interface, the thermocouple was moved in the smallest possible increments (5 μm) by the traverse stepper motor until the bead contacted the interface. This condition was detected by observing an abrupt change in the shape of the interface as well as a small jump in the continuous reading of the thermocouple. After the interface position was determined, the thermocouple was moved 500 μm up to make sure that the thermocouple detached from the liquid, and then quickly moved 495 μm down to reach to the interface without contacting

the liquid. Since the liquid interface was moving downward continuously, it was very difficult to find the exact distance between the interface and the edge of the bead at the beginning of each measurement. However, it was approximated by measuring the interface receding speed and the total time that the thermocouple took to move 500 μm up and return 495 μm down. The approximated distance between the interface and the edge of the bead when the thermocouple measured the interfacial temperature of the vapor has been calculated and will be shown in the following sections. The instantaneous interface position so determined was set to zero and the automated temperature measurement would start immediately. The stepper motor was programmed to measure the temperatures up to 25 mm above the interface with increasing increments of 62.5 μm, 125 μm, 250 μm, 625 μm, and 1250 μm. At each point of interest, the thermocouple stopped and 10 measurements were collected and the results were stored in a computer. Since the system was not fed by liquid, the interface would recede slowly during the temperature measurements. To account for this effect, the maximum interface receding speed corresponding to the lowest operating pressure was calculated to be ~ 0.28 μm/s. For the sampling time of 5 s for the thermocouple to collect 10 measurements at each point, the interface would move only 1.4 μm during the first measurement at the interface. This value corresponds to only 5.6% of the bead radius. It can be said that the distance between the center of the bead and the interface changed at most by 5.6% (*i.e.*, the maximum occurs when the bead just touches the interface) during the measurement at the first point. Note that the bead did not touch the interface. Therefore, this is the maximum percentage that this distance could change during the measurements. Similar calculations were repeated for other points in the vapor and in the liquid by taking into account both the time required for the thermocouple to move between the points and also the time that the thermocouple stopped at each point to collect data. For the second point and after, it was found that the change in the distance between the center of the bead to the interface due to the motion of the interface was smaller than that of the first point. For example, at the second, third, and fourth points, the distance between the bead and the interface would change at most by 3.5%, 3.2%, 3.0% respectively. Therefore, it can be said that the movement of the interface was much slower than the automated temperature measurements and had only a minor effect on the measured temperature profiles. Nevertheless, the experimental temperature profiles were corrected by taking the recession of the interface into account.

3.2.4 Evaporation flux measurement

The global evaporation rate at each pressure was measured by tracking the position of the interface with time, as shown in Figure 3-2.

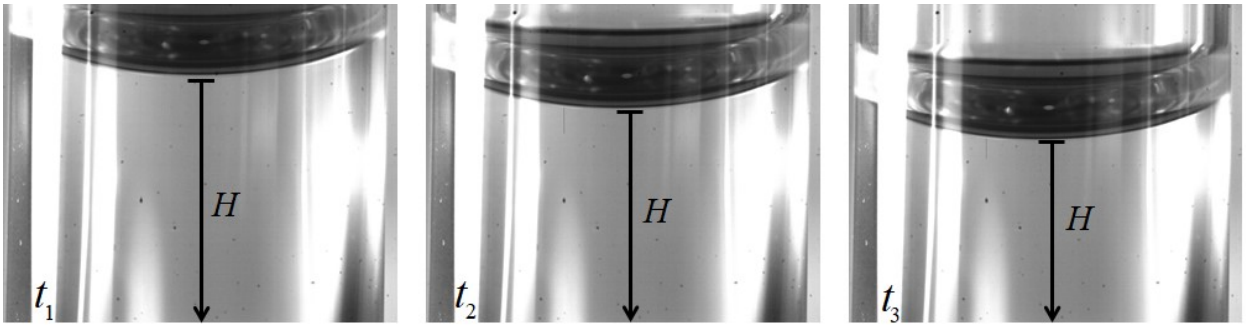

Figure 3-2 Recession of the interface during the measurement of the evaporation flux at three different times.

The average evaporation flux for each experiment was determined by calculating the slope of the plot of position *vs.* time and using the following mass balance equation:

$$m''_{exp} = -\bar{\rho}_l \left(\frac{A_c}{A_I}\right)\frac{dH}{dt}, \tag{3-1}$$

where m''_{exp} is the experimental evaporation flux (kg/m^{2}s), $\bar{\rho}_l$ is the liquid density at the average temperature between the surface and the bottom, A_c and A_I are the tube cross sectional area and the area of the liquid–vapor interface respectively, H is the interface position and was determined from images taken by the camera, and dH/dt is the slope of the plot of position with time. To calculate the area of the interface, A_I, the tube was partly filled with water and was placed in a cube of water. If we neglect the distortion of light as it passed through the thin wall (± 0.5 mm) of the tube, the undistorted shape of the interface could be approximated. The equation describing the interface was found by fitting a 6th order polynomial to 26 arbitrary points on half of the interface, with $R^2 = 0.99978$. The 6th order polynomial was then revolved around the vertical axis (z) and the area of the interface was determined by calculating the area of the revolved curve. The calculation of the area of the interface is demonstrated in Appendix D.

3.3 Formulation of governing equations

3.3.1 Model description

The schematic of the vacuum chamber to be considered in the model was shown in Figure 3-1a. All the elements shown in the figure including the liquid, vapor, glass cuvette, copper block and vacuum chamber wall are included in the model. However, the presence of the thermocouple in the vapor phase was disregarded. Since the Mach number ($M = U/c$) which corresponds to the ratio of the fluid velocity magnitude, U, to the speed of sound in the fluid, c, is very small ($M < 5\times10^{-3}$), the flow of the liquid can be considered incompressible. Therefore, the continuity equation in the liquid can be taken as $\nabla \cdot \boldsymbol{u} = 0$. However, this assumption may not hold in the vapor phase since under certain experimental conditions, the relative variation in the vapor density due to temperature change exceeds 15%. Therefore, the vapor flow is taken as compressible and the continuity equation in the vapor is written as:

$$\frac{\partial \rho}{\partial t} + \nabla \cdot (\rho \boldsymbol{u}) = 0, \tag{3-2}$$

where $\boldsymbol{u}$ is the fluid velocity vector (vector quantities are expressed by bold letters), and ρ denotes the density. In this study, as it was difficult to link the compressible flow of the vapor to the incompressible flow of the liquid in software, the liquid flow is also considered compressible to be consistent with the vapor, which is a more general assumption even though it might come at a higher computational cost.

The Navier–Stokes equations for laminar flow, which take into account the fluid compressibility, were utilized to describe the relationship between velocity, pressure, and density. In the case of a Newtonian fluid, neglecting the viscous dissipation, they are given by:

$$\rho \frac{\partial \boldsymbol{u}}{\partial t} + \rho(\boldsymbol{u} \cdot \nabla)\boldsymbol{u} = \nabla \cdot \left[-P\boldsymbol{I} + \mu(\nabla \boldsymbol{u} + (\nabla \boldsymbol{u})^T) - \frac{3}{2}\mu(\nabla \cdot \boldsymbol{u})\boldsymbol{I}\right] + \rho \boldsymbol{g}, \tag{3-3}$$

where P is the pressure, μ is the dynamic viscosity, $\boldsymbol{I}$ is the identity matrix, and $\boldsymbol{g}$ is the acceleration due to gravity. For the liquid the density is assumed to be only a function of temperature, and for the vapor the density is calculated from the ideal gas equation of state and hence is a function of temperature and pressure.

Heat transfer in the fluids was expressed by the following heat transfer convection–diffusion equation:

$$\rho C_p \left(\frac{\partial T}{\partial t} + \boldsymbol{u} \cdot \nabla T \right) = \nabla \cdot (k \nabla T), \tag{3-4}$$

where C_p is the constant pressure specific heat capacity, T is the absolute temperature, and k is the thermal conductivity which is assumed to vary with temperature. The heat fluxes in the liquid and vapor phases have been determined by Fourier's law of conduction. For the solids, the velocity is zero and the heat transfer equation reduces to:

$$\rho C_p \frac{\partial T}{\partial t} = \nabla \cdot (k \nabla T). \tag{3-5}$$

3.3.2 Initial and boundary conditions

Initially, the fluids are at rest ($\boldsymbol{u} = 0$), and the pressure distribution is assumed to be hydrostatic. The initial temperature distribution inside the liquid, vapor and solids is assumed to be uniform and equal to the room temperature ($T = T_\infty$).

3.3.2.1 Solid walls

A no-slip boundary condition was enforced at the solid walls that are in contact with the fluids which means that at the wall the fluids have zero velocity relative to the walls. However, when no-slip is applied to the inner wall of the tube, the Navier–Stokes equations coupled with the no-slip condition lead to a singularity in the contact line region[32–34] and make the motion of the contact line impossible. A common method to resolve this inconsistency is to allow the fluids to slip at the wall within a small region around the contact line. The slip velocity, as proposed by Navier[35] in 1823, might be assumed to be linearly related to the shear rate at the surface, so that:

$$\boldsymbol{u} \cdot \boldsymbol{n} = 0 \ , \ \boldsymbol{u} \cdot \boldsymbol{t} = -\frac{\beta}{\mu} (\boldsymbol{n} \cdot \boldsymbol{\tau}'), \tag{3-6}$$

where $\boldsymbol{n}$ is the unit normal vector, $\boldsymbol{t}$ is the unit tangent vector, $\boldsymbol{\tau}'$ is the stress tensor, and β is the slip length. For a compressible Newtonian fluid, the stress tensor is defined as:

$$\boldsymbol{\tau}' = -P\boldsymbol{I} + \mu(\nabla \boldsymbol{u} + (\nabla \boldsymbol{u})^T) - \frac{2}{3}\mu(\nabla \cdot \boldsymbol{u})\boldsymbol{I}. \quad (3\text{-}7)$$

The slip length β generally depends on the type of fluid and the surface properties of the solid substrate and has to be measured experimentally. For the case of hydrophilic surfaces which includes the tube used in this study ($\theta \approx 26°$), the typical slip lengths are within the range of 0 – 30 nm.[36] In this range, the model was not sensitive to the value of the slip length. This was verified by performing the simulation for several slip lengths and observing no changes in the predicted velocity, temperature, pressure and evaporation fluxes. Therefore, in the present work, the average value of β = 15 nm is selected for the slip length which is in agreement with the experimental values.

At the outside surface of the vacuum chamber, the temperature was fixed and assumed to be the same as the room temperature (*i.e.*, $T = T_\infty$). This is quite a reasonable assumption since in all experiments, the measured temperature in the vapor phase a few centimeters above the interface was very close to the room temperature. As there is no heat source in the chamber, it can be said that the outside wall temperature was near the ambient temperature. The temperature of the copper block is set to 4 °C which is the same as the experimental one that was monitored and controlled by a temperature controller. Finally, at all the internal solid–fluid boundaries, the temperatures and heat fluxes are considered to be continuous.

3.3.2.2 Exit boundary

At the outlet, the normal stress is specified as

$$\boldsymbol{\tau}_v' \cdot \boldsymbol{n} = -P_0 \boldsymbol{n}, \quad (3\text{-}8)$$

where P_0 is the absolute pressure at the boundary which is measured experimentally by a pressure transducer. Also, it is assumed that the temperature does not change across the boundary ($\nabla T = 0$) and the only mechanism of heat transfer at the exit boundary is by convection. This boundary condition was verified by measuring the temperatures in the vapor far from the interface with the thermocouple.

3.3.2.3 Liquid–vapor interface

At the liquid–vapor interface, we need to specify four boundary conditions to calculate the normal and tangential components of the velocities in both phases. The first condition is given by the mass balance at the interface as:

$$m'' = \rho_l(\boldsymbol{u_l} - \boldsymbol{u_i}) \cdot \boldsymbol{n} = \rho_v(\boldsymbol{u_v} - \boldsymbol{u_i}) \cdot \boldsymbol{n}, \tag{3-9}$$

where m'' is the local mass flux at the interface due to phase change and $\boldsymbol{n}$ is the unit normal vector at the interface which points toward the vapor. The indices *l*, *v*, and *i* denote the liquid, vapor, and interface respectively. The normal component of the velocity in the vapor can be related to that of the liquid by eliminating $\boldsymbol{u_i}$ from eq (3-9) and can be written as:

$$u_{l,n} = u_{v,n} + m''\left(\frac{1}{\rho_l} - \frac{1}{\rho_v}\right). \tag{3-10}$$

The second condition is obtained by assuming a no-slip condition at the interface which requires that the tangential components of velocities in liquid and vapor be equal. Thus:

$$\boldsymbol{u_{l,t}} = \boldsymbol{u_{v,t}} \tag{3-11}$$

The last two conditions are obtained from the momentum balance at the liquid–vapor interface as follows:

$$(\boldsymbol{\tau_l'} - \boldsymbol{\tau_v'}) \cdot \boldsymbol{n} = \sigma(\nabla_t \cdot \boldsymbol{n})\boldsymbol{n} - \nabla_t\sigma + m''(\boldsymbol{u_l} - \boldsymbol{u_v}), \tag{3-12}$$

where σ is the liquid surface tension which is a function of temperature, ∇_t is the surface gradient operator, and $\nabla_t \cdot \boldsymbol{n}$ is the curvature of the interface. The first term on the right hand side is due to capillary pressure, the second term is the Marangoni stress, and the last term is the momentum transfer due to inertia. The resulting vector from eq (3-12) can be decomposed into a part that is normal to the interface and a part that is tangential to the interface. The normal forces determine the local curvature and therefore the dynamic shape of the interface during evaporation which should be slightly different from the equilibrium shape as a result of being influenced by the fluid velocities. The disjoining pressure, which becomes significant in thin liquid films, was neglected in this study since the very slow recession of the interface due to the low evaporation rates along with imposing a slip condition near the contact line (eq (3-6)) would not allow the formation of a thin liquid film on the wall. The static contact angle at the contact line is assigned to be $\theta = \pi/7$

which was measured experimentally. The dynamic contact angles in the simulation, however, may deviate slightly from this value due to the motion of the contact line. The total energy balance at the interface is given by:[37]

$$(k^v \nabla T^v - k^l \nabla T^l) \cdot \boldsymbol{n} - (\boldsymbol{n} \cdot \boldsymbol{\tau_l}) \cdot (\boldsymbol{u_l} - \boldsymbol{u_i}) + (\boldsymbol{n} \cdot \boldsymbol{\tau_v}) \cdot (\boldsymbol{u_v} - \boldsymbol{u_i}) = m^{"} \left(h_{lv} + \frac{(\boldsymbol{u_v} - \boldsymbol{u_i})^2}{2} - \frac{(\boldsymbol{u_l} - \boldsymbol{u_i})^2}{2} \right), \quad (3\text{-}13)$$

where h_{lv} is the latent heat of evaporation and $\boldsymbol{\tau} = \boldsymbol{\tau}' + P\boldsymbol{I}$ is the stress tensor without the pressure term. Eq (3-13) is derived from the first law of thermodynamics and includes the heat transfer to the interface by the conduction mechanism, the work done by the normal and tangential stresses and the internal, flow, and kinetic energies in liquid and vapor. The heat transfer by radiation and the heat generated by viscous dissipation are ignored here. The second and the third terms are the work done by the normal and tangential stresses on the interface. Although these two terms are usually ignored in many studies, they are found to be significant in a number of experimental studies.[38,39] Therefore, we have kept them in the energy equation. The kinetic energy terms on the right side, however, are much smaller than the latent heat for typical maximum velocities in this study (≈ 0.1 m/s) and can be dropped from the boundary condition.

To compute the interfacial temperatures T^l and T^v, another thermal boundary condition is required at the interface. A simple approach is to assume that the interfacial temperatures are equal in both phases ($T^l = T^v$). Although this assumption is inconsistent with the experimental measurements,[21,23,40] we proceed with assuming a continuous temperature at the interface and a discussion regarding the validity of this assumption will be provided in the results section.

There are a number of theoretical models that have been developed to describe the mass flux across the liquid–vapor boundary. The flux at the interface might be calculated from the kinetic theory of gases (KTG), as proposed by Schrage[41] in the form:

$$m^{"}_{KTG} = \frac{2\psi}{2-\psi} \sqrt{\frac{1}{2\pi \bar{R}}} \left(\frac{P^{sat}(T^l)}{\sqrt{T^l}} - \frac{P^v}{\sqrt{T^v}} \right). \quad (3\text{-}14)$$

The constant ψ is the condensation coefficient and defines the fraction of the vapor molecules that are sorbed by the liquid after collision with the interface; P^{sat} is the saturation pressure at the

liquid temperature; M is molar mass, and $\bar{R} = R/M$ is the individual gas constant for water vapor. Ward and Fang[20] proposed a different expression for evaporation flux based on the statistical rate theory of interfacial transport (SRT) which uses the transition probability concept in quantum mechanics and the Boltzmann definition of entropy. The SRT mass flux across the interface is given by:

$$m''_{SRT} = \frac{P^{sat}\exp(v_\infty^l(P^l - P^{sat})/\bar{R}T^l)}{\sqrt{2\pi\bar{R}T^l}}\left(\exp(\Delta S/\bar{R}) - \exp(-\Delta S/\bar{R})\right), \tag{3-15}$$

where v_∞^l is the specific volume of the saturated liquid phase and ΔS is the change in the entropy due to phase change which is given in its most general form as:

$$\begin{aligned}\frac{\Delta S}{\bar{R}} = \Bigg\{ & 4\left(1 - \frac{T^v}{T^l}\right) \\ & + \left(\frac{1}{T^v} - \frac{1}{T^l}\right)\sum_{i=1}^{3}\left(\frac{\Theta_i}{2} + \frac{\Theta_i}{\exp(\Theta_i/T^v) - 1}\right) + \frac{v_\infty^l}{\bar{R}T^l}\left(P^l - P^{sat}(T^l)\right) \\ & + \ln\left[\left(\frac{T^v}{T^l}\right)^4 \frac{P^{sat}(T^l)}{P^v}\right] + \ln\left[\frac{q_{vib}(T^v)}{q_{vib}(T^l)}\right]\Bigg\}.\end{aligned} \tag{3-16}$$

Θ_i is the ith vibrational frequency of the water molecules, reported[42] to be 1590 cm^{-1}, 3651 cm^{-1}, and 3756 cm^{-1}, and q_{vib} denotes the vibrational partition function and is calculated from the following equation as:

$$q_{vib}(T) = \prod_{i=1}^{3}\frac{\exp(-\hbar\Theta_i/2k_BT)}{1 - \exp(-\hbar\Theta_i/k_BT)} \tag{3-17}$$

where k_B and $\hbar$ are the Boltzmann and the reduced Planck constants respectively.

3.4 Results and discussion

The fully coupled set of nonlinear equations in the previous section was solved using a commercial finite element software (COMSOL Multiphysics® version 5.2a, COMSOL Inc.),[43] subject to the given initial and boundary conditions. The physical properties of the fluids and solids are summarized in Table 3-1. The liquid, vapor, and solid domains were discretized using second order triangular elements as shown in Appendix E. To approximate the velocities and pressure in

the Navier–Stokes equations, P2+P1 elements were chosen in the software. An extensive convergence study was carried out to verify that the solutions were independent of the mesh size and time step (see Appendix E). To investigate how the velocities and the temperature in both the liquid and the vapor change with the applied pressure, the simulation was performed for the values of pressure corresponding to the available experimental data which ranged from 266 Pa to 815 Pa. Since the operating pressure is very small, the continuum assumption of the vapor phase needs to be verified. In the range of pressure used in this study, the Knudsen number ($Kn = \lambda / D$) in the vapor for all conditions was calculated and was found not to exceed 5×10^{-3}. The small values of Kn compared to unity indicate that the mean free path, λ of an individual molecule in the vapor is much smaller than the channel diameter, D, and the continuum assumption of the vapor flow is valid within the whole pressure range studied in this work. In addition, the assumption of laminar flow in both liquid and vapor was checked over the entire domain by calculating the Reynolds number. The local Reynolds number was calculated from the ratio of the inertial terms to the viscous terms in the Navier–Stokes equations (eq (3-3)) in each computational element and was found to be smaller than 9.6×10^{-3} and 1.7×10^{-2} everywhere in the liquid and vapor respectively. This indicates that the viscous forces always dominate and the assumption of laminar flow is reasonable.

Table 3-1 Thermodynamic properties of the liquid, vapor and solids used in the simulation

	Property value			Unit	Ref.
Liquid	$\mu_l(T) = 27.1\exp(-0.0352\,T)$			Pa s	44
	$\rho_l(T) = \dfrac{(999.84 + 16.945T - 7.99\times10^{-3}T^2 - 46.17\times10^{-6}T^3 + 105.56\times10^{-9}T^4 - 280.54}{1 + 16.88\times10^{-3}T}$			kg/m^3	45
	$\sigma(T) = 10^{-3}(114.81 - 0.1435T)$			N/m	46
	$k_l(T) = (T/228 - 1)^{0.18}$			W/(m K)	47
	$P^{sat}(T) = 611.2\exp\left(1045.85115 - \dfrac{21394.66626}{T} + 1.0969T - 1.300374\times10^{-3}T^2 + 7.747299\times10^{-7}T^3 - 2.1649\times10^{-12}T^4 - 211.3896\ln T\right)$			Pa	48
	$C_p^l = 2.98806\times10^7 - 548720\,T + 4031.78\,T^2 - 14.8134\,T^3 + 2.7215\times10^{-2}\,T^4 - 2\times10^{-5}\,T^5$			J/(kg K)	49
Vapor	$\mu_v(T) = \left(10^{-4}\sqrt{T/647.096}\right)\left(1.67752 + \dfrac{1426.601}{T} + \dfrac{2.6659\times10^5}{T^2} - \dfrac{6.5465\times10^7}{T^3}\right)^{-1}$			Pa s	50
	$C_p^v(T) = (1875.711 - 3.465\times10^{-1}T - 5.919\times10^{-4}T^2 + 7.240\times10^{-6}T^3)$			J/(kg K)	51
	$k_v(T) = 0.0088 - 10^{-5}T + 1.4\times10^{-7}T^2$			W/(m K))	50
	$h_{lv}(T) = T(1/\rho_v - 1/\rho_l)\times(dP^{sat}/dT)$			J/kg	48
	$\rho_v = P^V M/RT$			kg/m^3	
Solids	Copper	Aluminum	Borosilicate glass		
	$k = 386$ $\rho = 8930$ $C_p = 385$	$k = 230$ $\rho = 2700$ $C_p = 900$	$k = 1.14$ $\rho = 2210$ $C_p = 730$	W /(m K) kg/m^3 J/kg K	52

3.4.1 Flow pattern in liquid and vapor

A comparison of the experimentally obtained velocity field below the meniscus with that calculated from the numerical simulation for a typical pressure of 266 Pa is illustrated in Figure 3-3. The results show a qualitatively similar convective pattern in the liquid. As can be seen, the liquid in the middle region moves upward until it reaches the interface. Then it accelerates along the interface toward the wall due to the change in the direction and the magnitude of the velocity vector, providing a portion of the energy required for evaporation at the interface, and then strikes the solid wall. Separation of the flow occurs at this point on the wall and a small portion of the liquid goes up toward the contact line and most of the liquid turns back to the bulk. The return

flow, which has lost energy due to the energy exchange with the interface, moves downward as far as the inertial forces overcome the opposing viscous and buoyancy forces. Meanwhile, the fluid absorbs energy from the warmer solid wall. The liquid finally returns to the center as the buoyancy forces do not allow the light liquid to advance deeper into the dense liquid at the bottom (recall that colder water is less dense when $T < 4$ °C). This circulation of liquid forms a torus-shaped vortex below the interface whose size scales to the tube radius. The simulation results also show that there is a small counter rotating vortex near the contact line (see Figure 3-3 inset) which can be attributed to the surface tension effects. The small vortex vanishes if the surface tension in the simulation is assumed constant. This vortex is not visible in the experimental velocity since the peripheral area near the wall was not optically accessible due to the cylindrical distortion of the PIV images.

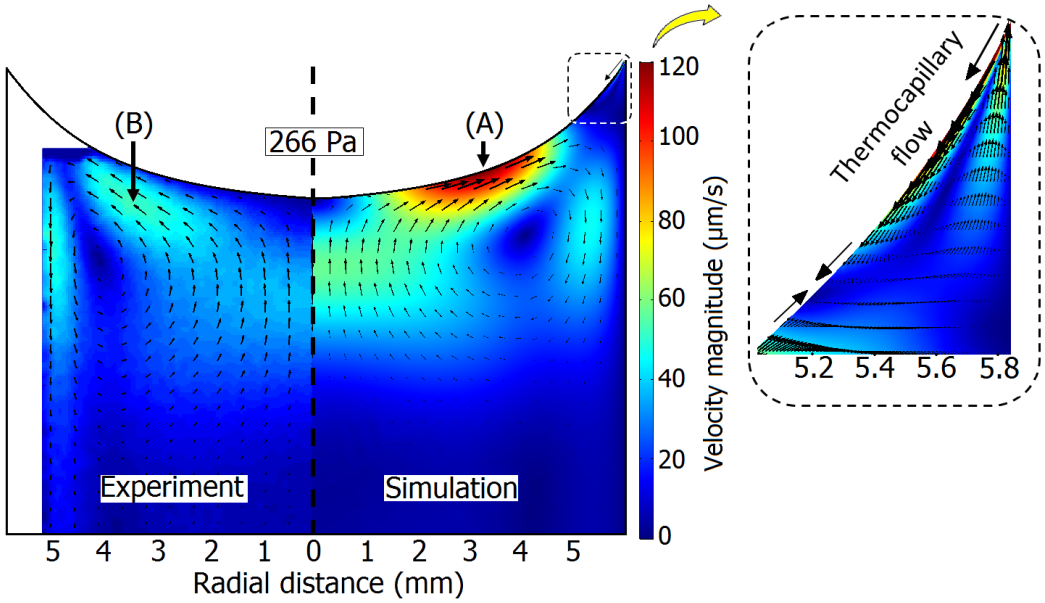

Figure 3-3 Comparison of the simulated velocities (right) with the experimental velocities obtained from PIV (left). (A) and (B) show the location of the maximum velocities. A small thermocapillary vortex (inset), which rotates in the opposite direction to the large buoyancy vortex, can be seen in in the simulation. This could not be captured experimentally.

It is worth mentioning that there is a distinguishable difference between the location and magnitude of the maximum velocities in the simulation and those in the experiments in Figure 3-3. The simulation results show that the maximum velocities are attained at the interface (A) while the experimental results demonstrate that the maximum velocities occur deeper in the liquid (B). In

addition to different locations, the magnitude of this velocity is different in the two cases with the simulation maximum velocity being almost twice as large as the experimental maximum velocity. One possibility for this discrepancy may be that the interfacial velocity vectors calculated during the PIV image processing algorithm are affected by the fuzzy region at the interface which resulted from the accumulation of particles in this region. To check if this is the issue, the velocity magnitude in a typical PIV experiment is superimposed on the images of particles and is shown in Figure 3-4a. The interrogation windows employed in the image processing, without considering the 75% overlap, are also shown in the figure as a white grid. As the figure illustrates, the location of the maximum velocity, which is marked with a white spot in the red region, is detected ~845 μm below the interface which corresponds to almost five interrogation windows away from the interface. Therefore, the intensities of the accumulated particles at the interface could not have affected this observation.

To gain a better understanding of how the particles behave while they move near the interface, the motion of the individual particles trapped at the surface was tracked with a higher magnification. For the concentration of particles used in the PIV experiments, it was difficult to distinguish between the accumulated particles at the interface due to the high scattering of light. To tackle this issue, the experiments were repeated using a 100 times diluted suspension. This leads to adsorbing fewer particles at the interface and distinguishing between the particles more easily. Figure 3-4c displays the track of some selected particles shown in Figure 3-4b in a typical experiment with the low concentration suspension.

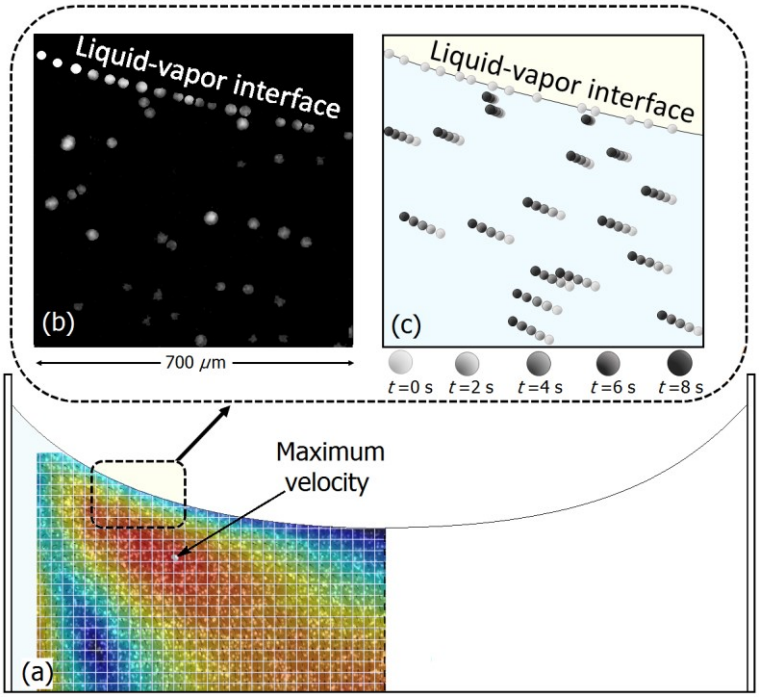

Figure 3-4 (a) Velocity magnitude and interrogation windows near the interface superimposed on the image of particles captured in a typical PIV experiment, (b) Magnified image of particles below the interface while a dilute suspension is used, and (c) position of selected particles in the dilute suspension over 8 seconds.

The position of particles is extracted from five consecutive images (not shown here) which are captured at intervals of 2 seconds. It can be seen from Figure 3-4c that the particles at the interface are completely stationary during this period and maintain their distances from the neighboring particles. A similar behavior of particles at the interface has been captured and reported in evaporation of a saline solution from a droplet[53,54] as well as in evaporation of water from a liquid film in a sealed cavity.[55] The suppression of the interfacial flows might be attributed to the presence of small quantities of surfactants in water[56–58] which were added to the purchased concentrated suspension to inhibit agglomeration, or from adsorbed particles acting as surfactants themselves. Therefore, we have found that during the velocity measurement by PIV, the particles trap and freeze at the interface and there is a *no-flow* condition at the free surface. As a result, a boundary layer in the liquid immediately below the interface would be developed which affects the velocity field near the interface. To verify this, the simulated velocities should match the experimental ones when the tangential velocity at the interface in the model is set to zero. However, implementation

of a zero velocity at the interface was not possible since it conflicted with the relaxation of the interface toward its equilibrium shape at the initial stages of the simulation. Alternatively, a *nearly* zero tangential velocity at the interface can be achieved by assuming a thin highly viscous layer beneath the interface. For this purpose, in the simulation, a 50 μm pseudo-layer with a viscosity of $\mu = 10^3 \mu_{water}$ was applied adjacent to the interface and the simulation was repeated for different pressures. A comparison between the results of the simulation including a viscous layer at the interface with the experimental velocity measured by PIV is provided in Figure 3-5. Interestingly, it can be seen that by adding the highly viscous layer into the model, the predicted velocity field in the liquid became very consistent with the experimental data in terms of the magnitude and the position of the maximum velocity below the interface. Therefore, it can be concluded that the disagreement between the experimental velocities and the simulation in Figure 3-3 can be attributed to the suppression of the interfacial flows in the presence of the particle suspension in the PIV experiment. Another conclusion that can be drawn here is that the observed flow in the experiment results from the buoyancy forces rather than thermocapillary forces. Otherwise, the maximum velocities would occur at the interface. The dimensionless Rayleigh number (*Ra*) and Bond number (*Bo*) in the liquid for different experiments are listed in Table 3-2.

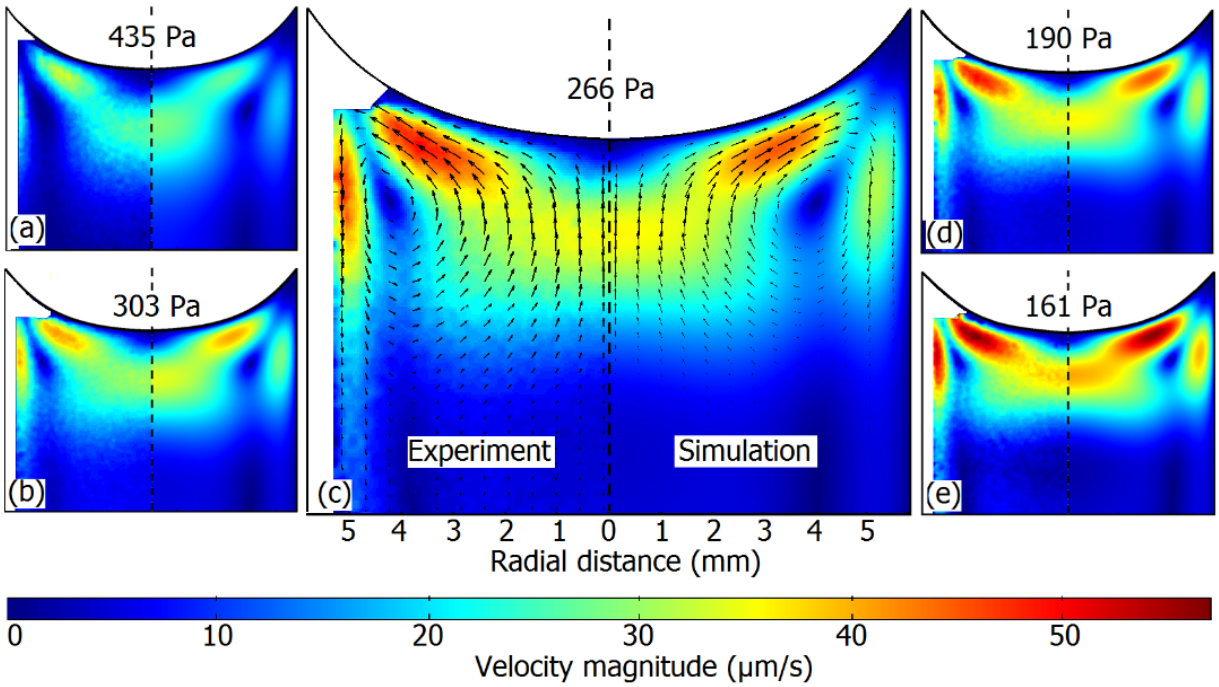

Figure 3-5 The experimental (left of each panel) and simulated (right of each panel) velocity field in the liquid at different pressures after imposing a zero tangential velocity on the interface.

It would be very difficult to capture the flow field in the vapor during evaporation experiments in a vacuum. However, they can be predicted from the numerical simulation. Figure 3-6 shows the simulated velocity field in the vapor for different operating pressures. It can be seen that the velocity in the vapor is almost four orders of magnitude larger than that in the liquid. The reason for this large difference is that the density of the vapor is very small at the pressures used in the experiments and to satisfy the conservation of mass (see eq (3-10)) the molecules have to accelerate when they enter the vapor phase. Figure 3-6 also shows that the flow of the vapor above the interface is strongly influenced by the geometry. At the interface, the vapor accelerates in the central region due to both a concave curvature of the interface and the presence of the wall. As soon as the solid wall ends, the velocity decreases rapidly due to the change in the cross-sectional area. The numerical results showed that the velocities of the vapor and subsequently the evaporation fluxes near the contact line were non-convergent due to the singularity of the contact line. However, we did not perform a detailed numerical study on this region since with the current mesh size, the simulated evaporation fluxes fairly matched the experimental fluxes although this region was not treated in further detail. This might be related to the fact that the thermocapillary

flow in the experiments was suppressed by a relatively stronger buoyancy driven vortex which was rotating in the opposite direction. As a result, the energy could hardly be distributed over the entire interface by means of the thermocapillary flow which made the high rate of heat transfer at the contact region almost ineffective. It should also be noted that the experimental study of the velocities near the contact line region in the round tube used in our experiments was impossible due to the optical inaccessibility of this region. We attempted to study this region separately using a rectangular cuvette. However, to be able to zoom in on the contact line, the camera lens needed to be very close to the cuvette wall. This was not possible due to the presence of the viewing windows of the vacuum chamber. The temperatures of the fluid adjacent to the solid wall were also difficult to measure with the current thermocouple with a bead diameter of ~50 μm. Such a thermocouple size could not provide a good resolution to capture the temperature variation in this region.

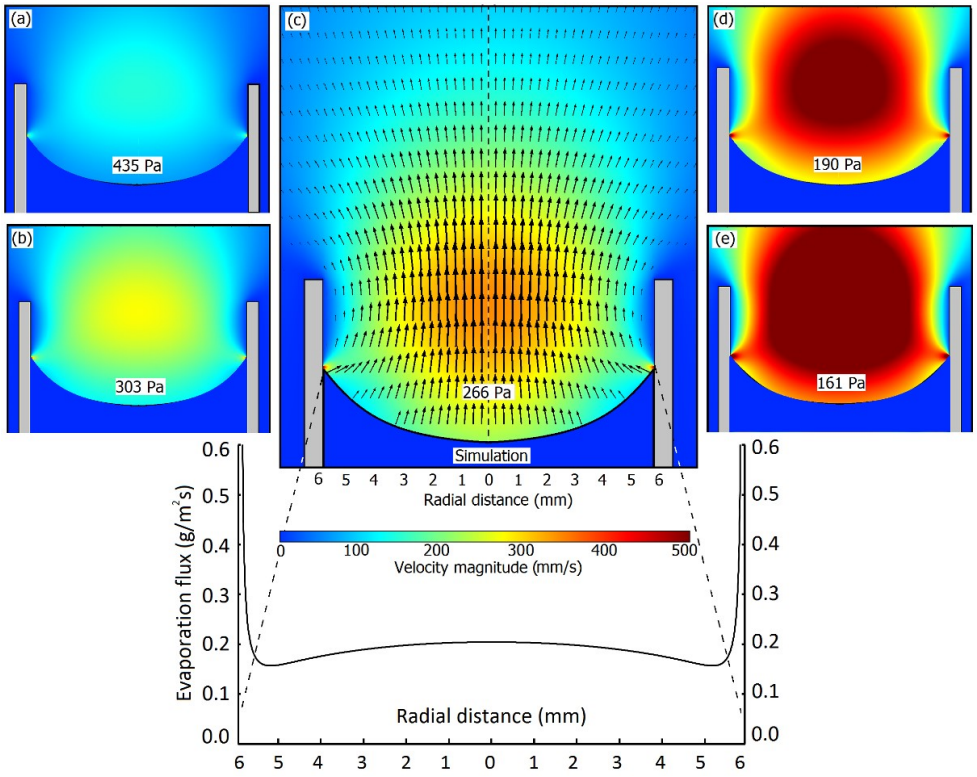

Figure 3-6 Simulated velocity magnitude and direction above the interface at different pressures. The evaporation flux distribution at the interface for P^V = 266 Pa is shown. The velocities in the vapor and the evaporation fluxes exhibit a singular behavior near the contact line.

3.4.2 Interfacial temperatures

The temperatures along the centerline in the liquid and vapor were measured separately using a fine thermocouple. A comparison between the measured temperatures and the results obtained from the numerical simulation for different pressures is shown in Figure 3-7. As expected, both the experimental and the simulation results show that the minimum temperature occurred at the interface for all pressures due to the evaporative cooling effects. As the figure illustrates, in the liquid phase, the simulated curves match the measured data quite well. The temperature profiles in the liquid show that the experimental temperatures increase monotonically with depth. In previous steady-state evaporation experiments in a stainless steel funnel,[21,22] a uniform-temperature layer in the liquid just below the interface was measured. The authors attributed this uniform-temperature layer to the mixing of the liquid by the thermocapillary flow at the interface. This uniform temperature layer did not occur in our experiments because the thermocapillary convection was overwhelmed by a large buoyancy vortex. By looking at the temperature profiles in the liquid, it can be understood that most of the heat required for evaporation is supplied from the vapor in contact with the vertical wall rather than the copper block in contact with the bottom of the tube. For instance, at 815 Pa, the simulated temperature of the liquid in the middle region is higher than those of the interface and the bottom. This indicates that the heat transfer through the vapor to the wall is significant although the thermal conductivity of the vapor ($k_v \sim 0.015$ W/m K) is much smaller than that of the copper ($k_{Cu} \sim 385$ W/m K). At the lower pressures, the amount of heat transfer to the liquid from outside is expected to become more pronounced since the temperature driving force becomes stronger and also the instabilities in the liquid become more vigorous.

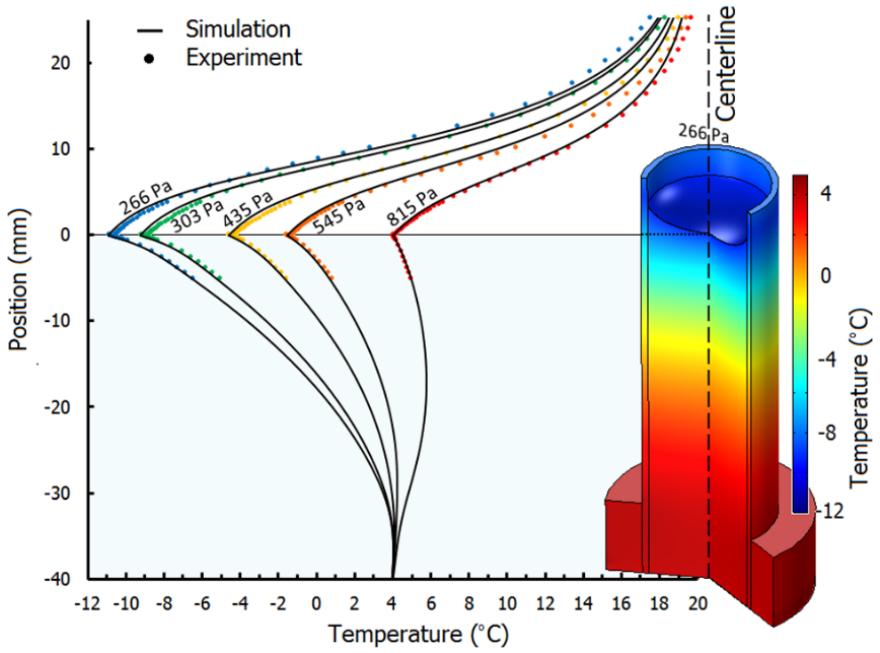

Figure 3-7 Temperature distribution near the interface along the vertical centerline for various pressures. The uncertainty associated with the temperature measurement is ± 0.05 °C. The error bars for this value are covered by the size of the data points. The 3D temperature illustration represents the simulated results at $P^V = 266$ Pa. The experimental temperatures in the liquid are not available below 5 mm since submerging the thermocouple deeper would stimulate the formation of bubbles on the bead which would expand rapidly and confound the measurements and sometimes the whole experiment.

In the vapor phase in Figure 3-7, the simulated temperature profiles match the measured data reasonably well. However, there is a noticeable deviation between the simulation and the experiment far from the interface in the vapor. One may argue that this deviation comes from the distortion of the velocity field in the vapor due to ignoring the presence of the thermocouple mount in the simulation (see Figure 3-1a). It is very unlikely that this is the reason since if it was, it would distort the flow near the interface as well and the temperatures would not match near the interface. The deviation probably originated either from assuming a fixed temperature (20 °C) as a boundary condition at the chamber outside wall for all simulations, or from simplifying the lower part of the vacuum chamber and assuming it to be symmetric, which results in a different flow field and a different temperature field respectively. Regardless of what the main reason is, this small deviation has only a minor effect on the results since, according to the simulation results, the vapor phase contribution in supplying the energy for evaporation to the interface is within the range of 8.6% –

10.8%, and most of the energy is supplied from the liquid side of the interface. To verify that the deviation does not play a significant role, the simulations were repeated by choosing a different temperature at the vacuum chamber outside wall so that the deviation became very small. The results showed that this small change in the vacuum chamber wall temperature had an insignificant effect on the evaporation rate and the velocity field. For instance, at 266 Pa, decreasing the wall temperature by 1 °C made only a 0.12% decrease in the evaporation flux, which is a negligible amount and left the velocity fields almost unchanged.

3.4.3 Temperature discontinuity

In all of the experiments, there was a discontinuity (jump) in the interfacial temperatures measured by the thermocouple on both sides of the interface, and the interfacial temperatures measured in the vapor were greater than those of the liquid (Table 3-2).

Table 3-2 Interfacial temperatures in liquid and vapor at the centerline measured by the thermocouple.

Pressure (Pa)	Experiment		$[T^V - T^L]$ (°C)	d_{TC} (μm)†	$Ra^{\S}$	$Bo^{\S}$
	T^L (°C)	T^V (°C)			$g\beta\Delta T\, L^3/\nu\alpha$	$\Delta\rho g\, D^2/\sigma$
265.7±1.3	−10.82 ± 0.05	−10.46 ± 0.05	0.36	12.1 ± 2.5	4,003,010	15.3
303.2±1.5	−9.15 ± 0.05	−8.82 ± 0.05	0.33	11.5 ± 2.5	3,175,250	15.4
369.4±1.8	−6.69 ± 0.05	−6.40 ± 0.05	0.29	11.6 ± 2.5	2,122,521	15.6
435.7±2.2	−4.52 ± 0.05	−4.28 ± 0.05	0.24	11.0 ± 2.5	1,362,071	15.5
544.6±2.7	−1.61 ± 0.05	−1.40 ± 0.05	0.21	10.0 ± 2.5	598,206	15.6
672.5±3.4	1.39 ± 0.05	1.56 ± 0.05	0.17	9.8 ± 2.5	130,576	15.7
815.5±4.1	4.08 ± 0.05	4.22 ± 0.05	0.14	9.7 ± 2.5	58	15.8

†d_{TC} is the approximated distance between the edge of the bead and the interface which is approximated as decribed in the experimental section

§ In calculation of *Ra* and *Bo* numbers, g is the gravitational acceleration (9.81 m/s^2), β is the coefficient of thermal expansion, ΔT is the difference between the temperature of the liquid at the bottom and that at the interface in the center, L is the height of the liquid at the center, ν is the kinematic viscosity, α is the thermal diffusivity, $\Delta\rho$ is the difference between the density of the liquid and the density of the vapor at the interface in the center, D is the tube diameter, and σ is the surface tension at the center of the meniscus. The physical properties used in calculation of *Ra* are the average between the bottom and the interface. For calculation of *Bo*, the properties at the interface are used.

The magnitude of the temperature discontinuity increased with decreasing pressure. It is worth mentioning that the temperature discontinuities observed in the present study were much smaller than those reported in the previous studies[18,19,21–24,59] at similar pressures. The maximum observed temperature discontinuity in our experiments was 0.36 °C which corresponded to the lowest operating pressure. One of the possible explanations for such a small temperature jump is that the vapor side heat flux in our study with a concave interface is much smaller than those obtained in

the previous studies at a convex interface, as shown in Figure 3-8a. In fact, the concave interface of the liquid in this study was surrounded by a solid wall and as was shown in Figure 3-6, the vapor velocity increases above the interface to satisfy mass conservation. This strong convection forms a temperature profile above the interface so that the interfacial temperature gradients and consequently the vapor heat flux to the interface become small. As was shown in references,[23,60] the temperature jump is proportional to the vapor side heat flux. Therefore, it is expected that we should observe a smaller jump in the current study compared to the previous ones.

To analyze the possible role of temperature discontinuity in the simulation results, the measured values of jumps were applied to the model as a new boundary condition at the interface and the simulations were repeated for all pressures. The results are illustrated in Figure 3-8b.

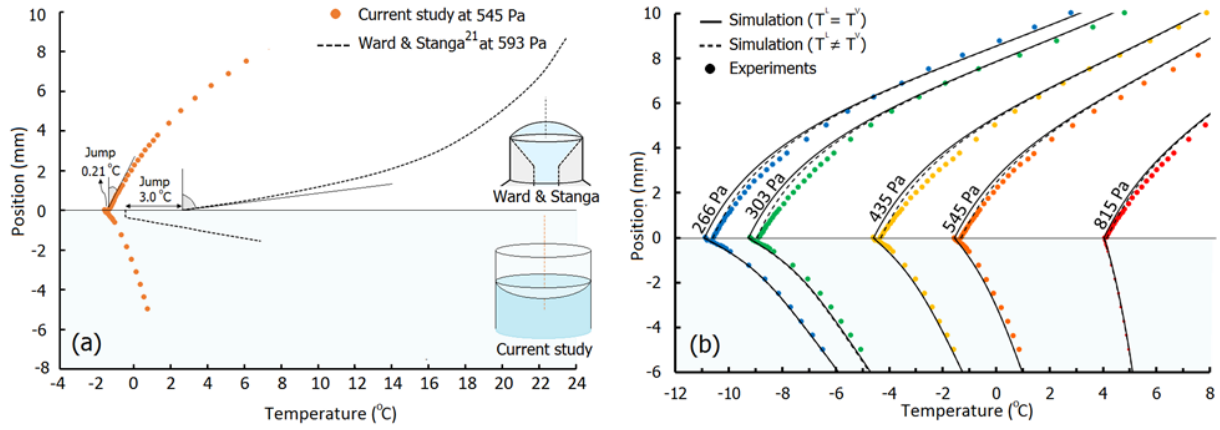

Figure 3-8 (a) The difference between the vapor side heat flux to the interface in this study and a typical study by Ward and Stanga.[21] (b) The effect of temperature discontinuity on the simulated temperatures in the liquid and vapor. The uncertainty associated with our temperature measurement is ± 0.05 °C. The error bars for these values are covered by the size of the data points.

As can be seen in Figure 3-8b, no detectable change was noticed in the temperature profiles in the liquid phase after using the new boundary condition. The main reason lies in the fact that the interfacial temperature of the liquid during evaporation in its vapor is very close to the saturation temperature corresponding to the pressure in the vapor phase (see ref. 28 for a mathematical proof), and since the pressure in the vapor is the same for the two cases, so is the saturation temperature and consequently the liquid interfacial temperature. In the vapor phase, however, there is a small difference between the temperature profiles for the two cases. This difference is at a maximum at

the interface and vanishes above 7 mm from the interface. Although the results obtained from the new boundary condition match the measured interfacial temperatures of the vapor, they seem to overestimate the temperature gradients in the vapor compared to the results obtained from a continuous temperature boundary condition. A comparison between the simulated evaporation fluxes with and without a temperature discontinuity at the interface is listed in Table 3-3. It can be seen that the effect of jump boundary condition on the evaporation fluxes is not remarkable. Therefore, assuming a discontinuous temperature at the interface does not produce a significant improvement in the simulation results.

Table 3-3 Comparison of the evaporation fluxes calculated in the simulation with and without the temperature jump at the interface.

Pressure (Pa)	$m''_{no\text{-}jump}$(kg/m^{2}s)	m''_{jump}(kg/m^{2}s)	$100\times(m''_{jump} - m''_{no\text{-}jump})/ m''_{no\text{-}jump}$
266	3.3906×10^{-4}	3.3984×10^{-4}	0.23%
303	3.1374×10^{-4}	3.1446×10^{-4}	0.23%
435	2.4158×10^{-4}	2.4202×10^{-4}	0.18%
545	1.9530×10^{-4}	1.9562×10^{-4}	0.16%
815	1.1337×10^{-4}	1.1143×10^{-4}	−1.7 %

3.4.4 Evaporation flux *vs.* pressure

The variation of the experimental and simulated evaporation fluxes with applied pressure is presented in Figure 3-9a. As expected, both the experimental and the simulation results show that the rate of evaporation increases as the pressure in the vacuum chamber decreases. According to Figure 3-9a, the evaporation fluxes calculated from both theoretical expressions are identical. Moreover, the evaporation fluxes calculated from KTG using different values of ψ are the same. This implies that the evaporation process in the current experimental setup is not controlled by the interfacial resistances to the molecular transport across the interface, but rather it is controlled by the rate of energy transport to the molecules at the interface. The thermal conductivity of the solid plays an important role in the rate of heat transfer to the interface. For evaporation of a droplet in atmospheric pressures, the thermal conductivity of the substrate has been found to have a significant effect on the rate of evaporation.[8–10] In the current study, the thermal conductivity of the borosilicate glass of which the cuvette is made is relatively small ($k \approx 1.14$ W/m K) compared to other materials such as metals. Thus, the low conductivity wall of the cuvette cannot keep up with the energy demand by the interface and limits the evaporation rate. In order to better

understand the effect of thermal conductivity on the evaporation rate of water at low pressures, the evaporation fluxes measured in the present experiments are compared to those obtained in several studies by the research groups of Ward and Durst in two different experimental setups. Figure 3-9b shows a comparison of the dependencies of the evaporation fluxes on the vacuum pressure.

Two different behaviors can be seen in the figure. In the experiments in which the funnel is made up of stainless steel ($k \approx 16$ W/m K), the evaporation flux increases rapidly with decreasing pressure. This means that the energy transport to the interface is fast enough and the controlling mechanism is more likely the interfacial resistances at the interface. However, when the thermal conductivity of the material is small, even in the same geometrical shape, the evaporation flux increases only slightly with decreasing pressure, pointing to the fact that the heat transfer to the interface is the controlling mechanism. This effect can result in underestimating the value of the condensation coefficient (ψ) for pure water. For instance, the values of ψ calculated based on the experimental conditions in this study and using eq (3-14) fall within the range of $0.0228 \leq \psi \leq 0.0802$. For the experiments in,[20,23] both of which are believed to be dominated by heat transfer to the interface as well, this value is reported to be in the range of $0.0586 \leq \psi \leq 0.1247$ and $0.03 \leq \psi \leq 0.15$ respectively. However, several studies have reported ψ to be close to unity.[61–63] Due to the small evaporation rates in the experiments dominated by heat transfer, the term $\left(P^{sat}/\sqrt{T^l} - P^v/\sqrt{T^v}\right)$ in eq (3-14) is small. The current thermocouples used for the measurements of the interfacial temperatures T^v, T^l (and P^{sat}), and the transducers used for the measurements of the pressure in the vapor (P^v) may not provide a good precision to calculate this term accurately. As a result, the obtained condensation coefficient, ψ, may differ from the true value. However, if the heat transfer limitation is removed, the evaporation flux increases significantly (see Figure 3-9b) and so does $\left(P^{sat}/\sqrt{T^l} - P^v/\sqrt{T^v}\right)$. Under this circumstance, the errors in the measurements have less effects on the calculation of ψ.

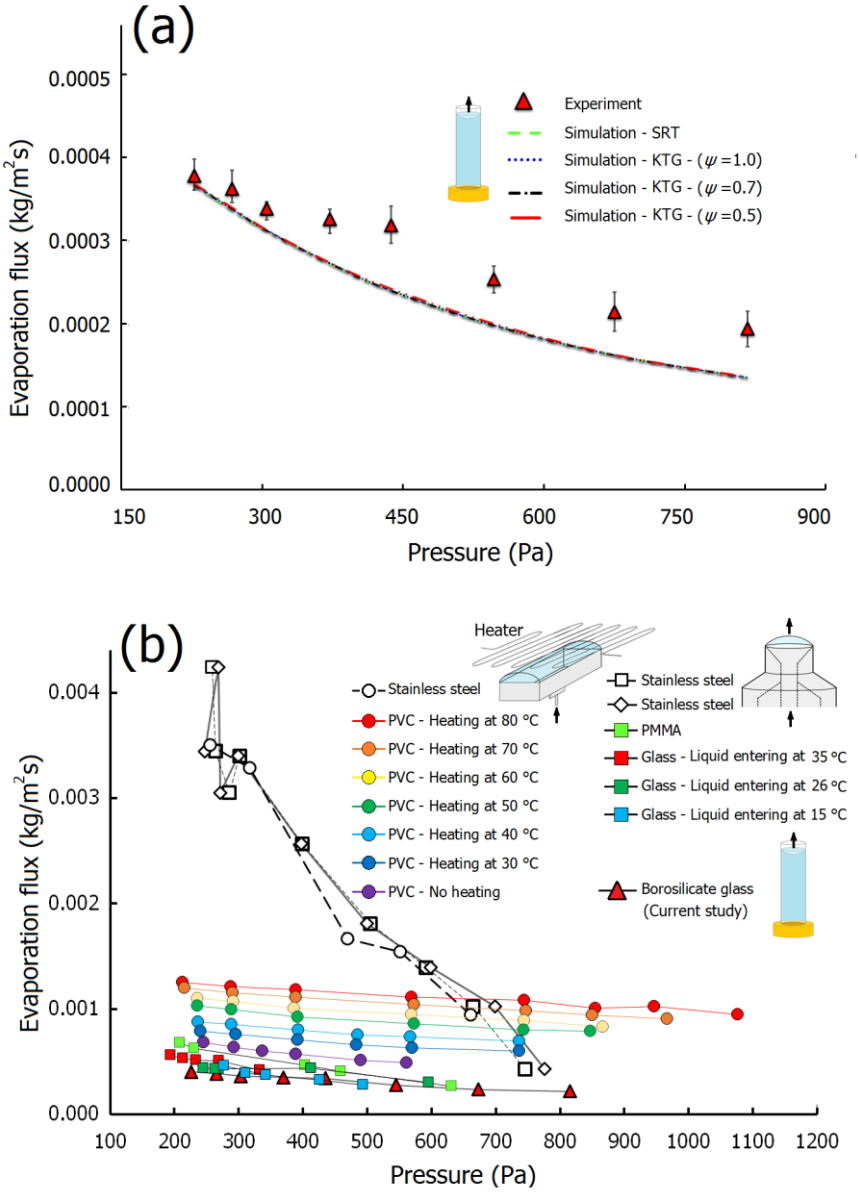

Figure 3-9 (a) Comparison of the simulated evaporation flux using two different theoretical expressions for flux with the experimental data. The experimental data show the evaporation flux of pure water in the absence of particles. The experimental data show the average of three experiments. The corresponding error bars show the minimum and the maximum values of the measured fluxes. The simulated curves show the predicted evaporation fluxes of pure water without implementation of a zero velocity at the interface. (b) Comparison of the evaporation fluxes obtained in this study with those obtained in previous studies.

In studies in which the evaporation seems not to be affected by the heat transfer limitation,[22,39,59] the presence of a thermocapillary flow close to the interface was reported. The detection of this flow was done either by a direct measurement of the interfacial liquid velocity with a fine deformable cantilever or from the energy balance at the interface and calculating the required interfacial velocity which satisfies the conservation of energy. However, in the experiments in which the evaporation flux seems to be dominated by heat transfer,[18,23,24] such as those of the present study, there was no evidence of the existence of a thermocapillary flow at the interface. Therefore, it is reasonable to conclude that a thermocapillary flow at the interface significantly reduces (perhaps eliminates) the limitations against the transport of molecules from the liquid to the vapor that are caused by the heat transfer.

It also appears from Figure 3-9b that equipping a heating element as close as 3 mm above the evaporating surface and increasing the element's temperature up to 80 °C in reference[23] was not effective in eliminating the heat transfer limitation. This is probably due to the fact that the contribution of the vapor in supplying the energy for evaporation was insignificant. Figure 3-9b also shows that increasing the amount of energy to the interface from the liquid side by increasing the feed temperature from 15 °C to 35 °C in reference[18] had a minor effect on the evaporation rate, and the evaporation flux still remained dominated by the heat transfer.

3.5 Conclusion

The evaporation of water from a concave meniscus was investigated under a controlled pressure and temperature condition. A mathematical model incorporating the mass, momentum and heat transfer in the liquid and vapor as well as the heat transfer in the solids was developed and solved using a finite element method. The velocity field in the center plane near the evaporating meniscus was measured using PIV. It was found that during the PIV measurement, the interfacial flows were suppressed at least for the slow buoyancy flow occurring in our evaporation experiments with typical velocities on the order of 100 μm/s. This was captured both experimentally, by observing the particles freezing at the interface, and theoretically, by the matching of the simulated velocities with the experimental velocities after the tangential velocity at the interface in the model was set to zero. Furthermore, the variation of temperatures in the

liquid and vapor along the vertical centerline of the tube was measured using a fine thermocouple. The measured temperature showed a discontinuity at the interface which was much smaller than those found in similar experiments at the same operating conditions. When these experimentally measured discontinuities were imposed in the mathematical model, no significant change was detected in the simulation results compared to when continuous temperatures were assumed.

The simulation results revealed that the evaporation process was dominated by heat transfer to the interface rather than the molecular transfer across the interface. This was concluded from the fact that imposing two different theoretical expressions of evaporation flux and also using different values of condensation coefficient in KTG gave the same value of evaporation flux in the simulation. Thus, it can be said that if the evaporation takes place in a container with a low thermal conductivity such as borosilicate glass which was used in this study, heat transfer to the interface controls the evaporation rate. In this case, all the existing theoretical expressions for evaporation flux, including SRT and KTG give the same result. Moreover, the condensation coefficient calculated from the experimentally measured temperatures and pressures in such studies is much smaller than unity, as it was in this study, while several studies have reported values close to 1 for the condensation coefficient of water,[61] and also several experiments are in excellent agreement with the SRT expression for evaporation flux, in which the condensation coefficient of water is assumed to be unity.[62] Therefore, in the experiments with heat transfer control of evaporation such as in this study, a careful heat balance analysis at the interface (similar to what was done in this study or the procedure followed by Ward and his coworkers)[38,39,59,64–66] needs to be done to compensate for the uncertainties associated with the temperature measurement by the thermocouple at the interface and pressure measurement by the pressure transducer in the vapor phase. Otherwise, the assessment of the theories of molecular transport across the interface does not guarantee a correct conclusion. However, if a material with a thermal conductivity much larger than that of the working liquid is used (*i.e.*, stainless steel), a thermocapillary flow at the interface occurs. As a result, the heat transfer limitation diminishes and becomes negligible compared to the interfacial resistances to the molecular transfer. In this case, the comparison between different evaporation flux theories is meaningful. Thus, we suggest that future experiments which aim to investigate the theoretically derived expressions for evaporation flux employ the highest available thermal conductivity materials such as aluminum ($k \approx 200\,\mathrm{W/(m\,K)}$), copper[66] ($k \approx$

400 W/(m K)), graphite ($k \approx 470$ W/(m K)), and graphene (k up to ≈ 5000 W/(m K)), to eliminate the restrictions created by the heat transfer.

3.6 References

(1) Deegan, R. D.; Bakajin, O.; Dupont, T. F.; Huber, G.; Nagel, S. R.; Witten, T. A. Capillary Flow as the Cause of Ring Stains from Dried Liquid Drops. *Nature* **1997**, *389* (6653), 827–829.

(2) Hu, H.; Larson, R. G. Marangoni Effect Reverses Coffee-Ring Depositions. *J. Phys. Chem. B* **2006**, *110* (14), 7090–7094.

(3) Bhardwaj, R.; Fang, X.; Attinger, D. Pattern Formation during the Evaporation of a Colloidal Nanoliter Drop: a Numerical and Experimental Study. *New J. Phys.* **2009**, *11* (7), 75020.

(4) Maki, K. L.; Kumar, S. Fast Evaporation of Spreading Droplets of Colloidal Suspensions. *Langmuir* **2011**, *27* (18), 11347–11363.

(5) Thokchom, A. K.; Majumder, S. K.; Singh, A. Internal Fluid Motion and Particle Transport in Externally Heated Sessile Droplets. *AIChE J.* **2016**, *62* (4), 1308–1321.

(6) Hu, H.; Larson, R. G. Evaporation of a Sessile Droplet on a Substrate. *J. Phys. Chem. B* **2002**, *106* (6), 1334–1344.

(7) David, S.; Sefiane, K.; Tadrist, L. Experimental Investigation of the Effect of Thermal Properties of the Substrate in the Wetting and Evaporation of Sessile Drops. *Colloids Surfaces A Physicochem. Eng. Asp.* **2007**, *298* (1–2), 108–114.

(8) Talbot, E. L.; Berson, A.; Brown, P. S.; Bain, C. D. Evaporation of Picoliter Droplets on Surfaces with a Range of Wettabilities and Thermal Conductivities. *Phys. Rev. E* **2012**, *85* (6), 61604.

(9) Dunn, G. J.; Wilson, S. K.; Duffy, B. R.; David, S.; Sefiane, K. The Strong Influence of Substrate Conductivity on Droplet Evaporation. *J. Fluid Mech.* **2009**, *623* (2009), 329–351.

(10) Bazargan, V.; Stoeber, B. Effect of Substrate Conductivity on the Evaporation of Small Sessile Droplets. *Phys. Rev. E* **2016**, *94* (3), 33103.

(11) Chandra, S.; di Marzo, M.; Qiao, Y. M.; Tartarini, P. Effect of Liquid-Solid Contact Angle on Droplet Evaporation. *Fire Saf. J.* **1996**, *27* (2), 141–158.

(12) McHale, G.; Aqil, S.; Shirtcliffe, N. J.; Newton, M. I.; Erbil, H. Y. Analysis of Droplet Evaporation on a Superhydrophobic Surface. *Langmuir* **2005**, *21* (24), 11053–11060.

(13) Fukatani, Y.; Orejon, D.; Kita, Y.; Takata, Y.; Kim, J.; Sefiane, K. Effect of Ambient Temperature and Relative Humidity on Interfacial Temperature during Early Stages of Drop Evaporation. *Phys. Rev. E* **2016**, *93* (4), 43103.

(14) Dehaeck, S.; Rednikov, A.; Colinet, P. Vapor-Based Interferometric Measurement of Local Evaporation Rate and Interfacial Temperature of Evaporating Droplets. *Langmuir* **2014**, *30* (8), 2002–2008.

(15) McGaughey, A. J. H.; Ward, C. A. Temperature Discontinuity at the Surface of an Evaporating Droplet. *J. Appl. Phys.* **2002**, *91* (10), 6406–6415.

(16) Erbil, H. Y. Evaporation of Pure Liquid Sessile and Spherical Suspended Srops: A Review. *Adv. Colloid Interface Sci.* **2012**, *170* (1–2), 67–86.

(17) Cazabat, A.-M.; Guéna, G. Evaporation of Macroscopic Sessile Droplets. *Soft Matter* **2010**, *6* (12), 2591.

(18) Fang, G.; Ward, C. A. Temperature Measured close to the Interface of an Evaporating Liquid. *Phys. Rev. E* **1999**, *59* (1), 417–428.

(19) Fang, G.; Ward, C. A. Examination of the Statistical Rate Theory Expression for Liquid Evaporation Rates. *Phys. Rev. E* **1999**, *59* (1), 441–453.

(20) Ward, C. A.; Fang, G. Expression for Predicting Liquid Evaporation Flux: Statistical Rate Theory Approach. *Phys. Rev. E* **1999**, *59* (1), 429–440.

(21) Ward, C. A.; Stanga, D. Interfacial Conditions during Evaporation or Condensation of Water. *Phys. Rev. E* **2001**, *64* (5), 51509.

(22) Ward, C. A.; Duan, F. Turbulent Transition of Thermocapillary Flow Induced by Water Evaporation. *Phys. Rev. E* **2004**, *69* (5), 56308.

(23) Badam, V. K.; Kumar, V.; Durst, F.; Danov, K. Experimental and Theoretical Investigations on Interfacial Temperature Jumps during Evaporation. *Exp. Therm. Fluid Sci.* **2007**, *32* (1), 276–292.

(24) Thompson, I.; Duan, F.; Ward, C. A. Absence of Marangoni Convection at Marangoni Numbers above 27,000 during Water Evaporation. *Phys. Rev. E* **2009**, *80* (5), 56308.

(25) Song, X.; Nobes, D. S. Experimental Investigation of Evaporation-Induced Convection in Water Using Laser Based Measurement Techniques. *Exp. Therm. Fluid Sci.* **2011**, *35* (6), 910–919.

(26) Kuznetzov, G. V; Sitnikov, A. E. Numerical Modeling of Heat and Mass Transfer in a Low-Temperature Heat Pipe. *J. Eng. Phys. Thermophys.* **2002**, *75* (4), 840–848.

(27) Kirillov, Y. P.; Shaposhnikov, V. A.; Kuznetsov, L. A.; Shiryaev, V. S.; Churbanov, M. F. Modeling of the Evaporation of Liquids and Condensation of Their Vapor during Distillation. *Inorg. Mater.* **2016**, *52* (11), 1183–1188.

(28) Qin, T.; Tuković, Z.; Grigoriev, R. O. Buoyancy-Thermocapillary Convection of Volatile Fluids Under Their Vapors. *Int. J. Heat Mass Transf.* **2015**, *80*, 38–49.

(29) Qin, T.; Tuković, Z.; Grigoriev, R. O. Buoyancy-Thermocapillary Convection of Volatile Fluids Under Atmospheric Conditions. *Int. J. Heat Mass Transf.* **2014**, *75*, 284–301.

(30) Kazemi, M. A.; Elliott, J. A. W.; Nobes, D. S. Determination of the Three Components of Velocity in an Evaporating Liquid from Scanning PIV. In *The 18th International Symposium on the Application of Laser and Imaging Techniques to Fluid Mechanics, July 4 – 7*; Lisbon Portugal, 2016.

(31) Kazemi, M. A.; Elliott, J. A. W.; Nobes, D. S. A 3D Flow Visualization in Evaporation of Water from a Meniscus at Low Pressures. In *The 10th Pacific Symposium on Flow Visualization and Image Processing, Naples, Italy, 15-18 June*; 2015.

(32) Koplik, J.; Banavar, J. R.; Willemsen, J. F. Molecular Dynamics of Fluid Flow at Solid Surfaces. *Phys. Fluids A Fluid Dyn.* **1989**, *1* (5), 781–794.

(33) Dussan, E. B. On the Spreading of Liquids on Solid Surfaces: Static and Dynamic cContact Lines. *Annu. Rev. Fluid Mech.* **1979**, *11* (1), 371–400.

(34) de Gennes, P. G. Wetting: Statics and Dynamics. *Rev. Mod. Phys.* **1985**, *57* (3), 827–863.

(35) Navier, C. L. M. H. Mémoire Sur Les Lois du Mouvement des Fluides. *Mémoires l'Académie R. des Sci. l'Institut Fr.* **1823**, *6*, 389–440.

(36) Lauga, E.; Brenner, M.; Stone, H. Microfluidics: The No-Slip Boundary Condition. In *Springer Handbook of Experimental Fluid Mechanics*; Springer Berlin Heidelberg: Berlin, Heidelberg, 2007; pp 1219–1240.

(37) Faghri, A.; Zhang, Y. *Transport Phenomena in Multiphase Systems*, 1st ed.; Academic Press, 2006.

(38) Duan, F.; Ward, C. A. Surface-Thermal Capacity of D_2O from Measurements Made during Steady-State Evaporation. *Phys. Rev. E* **2005**, *72* (5), 56304.

(39) Duan, F.; Ward, C. A. Surface Excess Properties from Energy Transport Measurements during Water Evaporation. *Phys. Rev. E* **2005**, *72* (5), 56302.

(40) Popov, S.; Melling, A.; Durst, F.; Ward, C. A. Apparatus for Investigation of Evaporation at Free Liquid–Vapour Interfaces. *Int. J. Heat Mass Transf.* **2005**, *48* (11), 2299–2309.

(41) Schrage, R. W. *A Theoretical Study of Interface Mass Transfer*; New York, Columbia University Press, 1953.

(42) McClelland, B. J. *Statistical Thermodynamics*; Chapman and Hall: London, 1973; Vol. 92.

(43) *COMSOL Multiphysics® v. 5.2a,*; AB, Stockholm, Sweden, 2016.

(44) Kestin, J.; Sokolov, M.; Wakeham, W. A. Viscosity of Liquid Water in the Range −8 °C to 150 °C. *J. Phys. Chem. Ref. Data* **1978**, *7* (3), 941.

(45) Kell, G. S. Density, Thermal Expansivity, and Compressibility of Liquid Water from 0 °C to 150 °C. Correlations and Tables for Atmospheric Pressure and Saturation Reviewed and Expressed on 1968 Temperature Scale. *J. Chem. Eng. Data* **1975**, *20* (1), 97–105.

(46) Vinš, V.; Fransen, M.; Hykl, J.; Hrubý, J. Surface Tension of Supercooled Water Determined by Using a Counterpressure Capillary Rise Method. *J. Phys. Chem. B* **2015**, *119* (17), 5567–5575.

(47) Benchikh, O.; Fournier, D.; Boccara, A. C.; Teixeira, J. Photothermal measurement of the thermal conductivity of supercooled water. *J. Phys.* **1985**, *46* (5), 727–731.

(48) Duan, F.; Thompson, I.; Ward, C. A. Statistical Rate Theory Determination of Water Properties below the Triple Point. *J. Phys. Chem. B* **2008**, *112* (29), 8605–8613.

(49) Archer, D. G.; Carter, R. W. Thermodynamic Properties of the NaCl + H_2O System. 4. Heat Capacities of H_2O and NaCl(aq) in Cold-Stable and Supercooled State. *J. Phys. Chem. B* **2000**, *104* (35), 8563–8584.

(50) Wagner, W.; Pruß, A. The IAPWS Formulation 1995 for the Thermodynamic Properties of Ordinary Water Substance for General and Scientific Use. *J. Phys. Chem. Ref. Data* **2002**, *31* (2), 387–535.

(51) Liley, P. E. Thermophysical Properties of Ice/Water/Steam from -20°C to 50°C. *Int. J. Mech. Eng. Educ.* **2005**, *33* (1), 45–50.

(52) Rohsenow, W. M.; Hartnett, J. P.; Cho, Y. I. *Handbook of Heat Transfer*; New York: McGraw-Hill, 1998; Vol. 3.

(53) Kang, K. H.; Lim, H. C.; Lee, H. W.; Lee, S. J. Evaporation-Induced Saline Rayleigh Convection inside a Colloidal Droplet. *Phys. Fluids* **2013**, *25* (4), 42001.

(54) Lee, S. J.; Hong, J.; Choi, Y. Evaporation-Induced Flows inside a Confined Droplet of Diluted Saline Solution. *Langmuir* **2014**, *30* (26), 7710–7715.

(55) Li, Y.; Yoda, M. Convection Driven by a Horizontal Temperature Gradient in a Confined Aqueous Surfactant Solution: The Effect of Noncondensables. *Exp. Fluids* **2014**, *55* (1), 1663.

(56) Farley, R. W.; Schechter, R. S. Retardation of Surface Velocities by Surfactants. *Chem. Eng. Sci.* **1966**, *21*, 1079–1093.

(57) Cuenot, B.; Magnaudet, J.; Spennato, B. The Effects of Slightly Soluble Surfactants on the Flow around a Spherical Bubble. *J. Fluid Mech.* **1997**, *339*, 25–53.

(58) Wu, T.-C.; Yang, Y.-M.; Maa, J.-R. Surfactant-Induced Retardation of the Thermocapillary Flow at a Gas/Liquid Interface. *Int. Commun. Heat Mass Transf.* **2000**, *27* (5), 655–666.

(59) Duan, F.; Badam, V. K.; Durst, F.; Ward, C. A. Thermocapillary Transport of Energy during Water Evaporation. *Phys. Rev. E* **2005**, *72* (5), 56303.

(60) Bond, M.; Struchtrup, H. Mean Evaporation and Condensation Coefficients Based on

Energy Dependent Condensation Probability. *Phys. Rev. E* **2004**, *70* (6), 61605.

(61) Eames, I. W.; Marr, N. J.; Sabir, H. The Evaporation Coefficient of Water: A Review. *Int. J. Heat Mass Transf.* **1997**, *40* (12), 2963–2973.

(62) Persad, A. H.; Ward, C. A. Expressions for the Evaporation and Condensation Coefficients in the Hertz-Knudsen Relation. *Chem. Rev.* **2016**, *116* (14), 7727–7767.

(63) Julin, J.; Shiraiwa, M.; Miles, R. E. H.; Reid, J. P.; Pöschl, U.; Riipinen, I. Mass Accommodation of Water: Bridging the Gap Between Molecular Dynamics Simulations and Kinetic Condensation Models. *J. Phys. Chem. A* **2013**, *117* (2), 410–420.

(64) Duan, F.; Ward, C. A. Investigation of Local Evaporation Flux and Vapor-Phase Pressure at an Evaporative Droplet Interface. *Langmuir* **2009**, *25* (13), 7424–7431.

(65) Das, K. S.; Ward, C. A. Surface Thermal Capacity and its Effects on the Boundary Conditions at Fluid-Fluid Interfaces. *Phys. Rev. E* **2007**, *75* (6), 65303.

(66) Ghasemi, H.; Ward, C. A. Energy Transport by Thermocapillary Convection during Sessile-Water-Droplet Evaporation. *Phys. Rev. Lett.* **2010**, *105* (13), 136102.

Chapter 4: Effect of the Thermocouple on Measuring the Temperature Discontinuity at the Liquid–Vapor Interface[§]

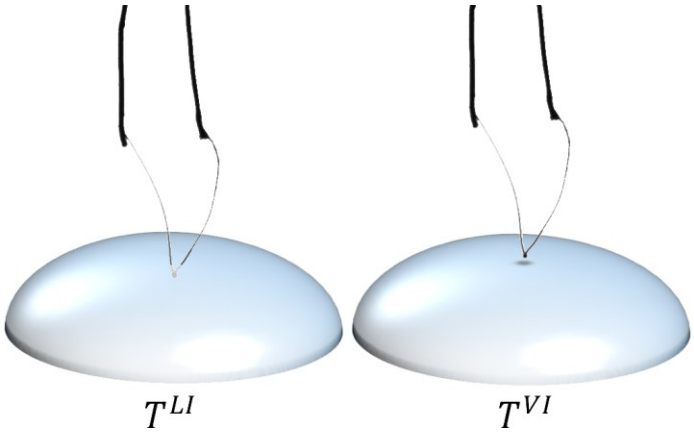

Graphical Abstract
Chapter 4

The coupled heat and mass transfer that occurs in evaporation is of interest in a large number of fields such as evaporative cooling, distillation, drying, coating, printing, crystallization, welding, atmospheric processes, and pool fires. The temperature jump that occurs at an evaporating interface is of central importance to understanding this complex process. Over the past three decades, thermocouples have been widely used to measure the interfacial temperature jumps at a liquid–vapor interface during evaporation. However, the reliability of these measurements has not been investigated so far. In this study, a numerical simulation of a thermocouple when it measures the interfacial temperatures at a liquid–vapor interface is conducted to understand the possible effects of the thermocouple on the measured temperature and features in the temperature profile. The differential equations of heat transfer in the solid and fluids as well as the momentum transfer in the fluids are coupled together and solved numerically subject to appropriate boundary conditions between the solid and fluids. The results of the numerical simulation showed that while thermocouples can measure the interfacial temperatures in the liquid correctly, they fail to read the actual interfacial temperatures in the vapor. As the results of our numerical study suggest, the temperature jumps at a liquid–vapor interface measured experimentally by using a thermocouple are larger than what really exists at the interface. For a typical experimental study of evaporation of water at low pressure, it was found that the temperature jumps measured by a thermocouple are

[§] This chapter as well as Appendix F and Appendix G with minor modifications have been published as Kazemi, M. A.; Nobes, D. S.; Elliott, J. A. W. Effect of the Thermocouple on Measuring the Temperature Discontinuity at a Liquid–Vapor Interface. *Langmuir* 2017, *33* (28), 7169–7180.

overestimated by almost 50%. However, the revised temperature jumps are still in agreement with the statistical rate theory of interfacial transport. As well as addressing the specific application of the liquid–vapor temperature jump, this chapter provides significant insight into the role that heat transfer plays in the operation of thermocouples in general.

4.1 Introduction

The temperature jump that occurs at the interface of an evaporating liquid is of great interest[1–24] due to its relationship to understanding the physics of evaporation. A temperature discontinuity at a liquid–vapor interface during evaporation has been shown to exist by both theoretical[1,2] and experimental[3,4] studies. However, a substantial disagreement between the magnitude and the direction of the theoretical and experimental temperature discontinuities at the interface has been reported.

Shankar and Deshpande[5] performed the first experiments to investigate the interfacial temperature discontinuities at a liquid–vapor interface. They studied the evaporation of three liquids, namely, water, mercury, and Freon 113 and used ten thermocouples epoxied to the vacuum chamber wall to measure the temperature profiles in the liquid and vapor. The wire size of the thermocouples was ~ 300 μm, and the size of the resulting junction was not mentioned. They found a large temperature jump at the interface of the evaporating mercury (~12 °C) but reported a very small jump (~1 °C) at the water and Freon 113 surfaces. Although the distance between the adjacent thermocouples on both sides of the interface was given in their study, the relative distance of the interface to thermocouples at either side was undetermined, which left some degree of ambiguity about the existence of a temperature jump at the water and Freon 113 surfaces. Hisatake *et al.*[6] used a thermocouple with a wire diameter of 127 μm to measure the temperature profile across the interface of water while it was evaporating into the air at atmospheric pressure. Although the scatter plot of the temperature profiles they reported showed a discontinuity at the interface, they drew a smooth curve among the scattered data and assumed a continuous temperature at the interface.

To study the interfacial temperatures at a higher resolution, Fang and Ward[3] measured the temperature profiles across the liquid–vapor interface of distilled, deionized water during steady-

state evaporation at low pressures. By using a 25 μm thermocouple with a bead diameter of ~50 μm, they could reach as close as one mean free path to the interface and noticed a relatively large temperature discontinuity at the interface, which was not detected earlier. In all of their experiments, they found that the vapor temperature was greater than the liquid temperature at the interface. The direction of the measured temperature jumps contradicted the prediction of the classical kinetic theory of gases (KTG) which indicated that the vapor at the interface should be colder than the liquid during evaporation. The magnitude of the jumps that they measured also differed significantly from the KTG prediction. For instance, at the highest evaporation rate, they measured a jump as large as 7.8 °C, while the jump predicted by KTG was only 0.027 °C in the opposite direction. Further investigations and repeated experiments on evaporation of water,[7–12] ethanol,[13–15] octane and methylcyclohexane[16] with an identical thermocouple confirmed the magnitude and the direction of the jumps found by Fang and Ward. To fill in this significant gap between the theory and experiments, Ward and Fang developed a new theoretical expression for the evaporation flux at the interface based on the statistical rate theory (SRT) of interfacial transport of molecules.[16,17] The new SRT expression could predict the pressure in the vapor (P^V) within the experimental uncertainty of the measuring instrument by using the measured interfacial temperatures (T^{LI}, T^{VI}) and evaporation fluxes.

By generalizing the Hertz–Knudsen and Schrage equations for the evaporation mass and energy fluxes at a liquid–vapor interface, Bond and Struchtrup[18] showed that the values of the interfacial temperature jump strongly depend on the heat flux from the vapor side of the interface. Motivated by this theoretical study, Badam *et al.*[4,19] experimentally investigated the effect of the vapor side heat flux on the temperature jumps at the interface of an evaporating water at low pressures using a thermocouple with a wire diameter of 25 μm. By heating the vapor from above, they could measure a temperature jump of up to 27.83 °C. They suggested that a larger jump could be achieved by further increasing the vapor heating rate. They examined the results of the temperature jumps with two theories, KTG, and nonequilibrium thermodynamics (NET). The temperature jumps predicted by KTG were in the same direction as the experimentally measured jumps, but were 10–20 times smaller in magnitude. Kazemi *et al.*[20] studied the interfacial temperatures at a liquid–vapor interface during a pseudo steady-state evaporation of water at low pressures. The vapor heat fluxes in their experiments were very small due to the concave shape of

the interface. Therefore, the 25 μm thermocouple they used to measure the temperatures showed a relatively small temperature jump (up to 0.36 °C). They also studied the system mathematically and found that neglecting the temperature jump at the interface had minor effects on the simulated temperatures profiles, velocities, and evaporation fluxes. McGaughey and Ward[21] measured the temperature discontinuity at the surface of an evaporating water droplet while it was hanging from a thermocouple. To make their measurements less intrusive, they measured the temperature of the vapor at a point far from the interface and used this temperature to find the solution of the heat diffusion equation in the vapor. By doing so, they calculated a temperature jump in the range of 0.63–1.04 °C at the interface. They also reported that by taking the measured jumps into account better agreement was obtained with a D^2 law (which states that the surface area of an evaporating droplet with a diameter of D decreases linearly with time as it evaporates into a noncondensable gas). However, we note that by manipulating the measured temperatures and position of the interface within the experimental uncertainties, the calculated jumps at the interface could decrease, and for certain experiments, they could vanish and even become negative (see Appendix F).

While the studies discussed have reported a positive jump at the interface ($T^{VI} > T^{LI}$), some others have shown a negative jump ($T^{VI} < T^{LI}$). Zhu *et al.*[22,23] measured the temperature profiles close to the interface of silicon oil evaporating into the air at atmospheric pressure using a thermocouple with a wire diameter of 50 μm. Depending on the applied horizontal temperature difference to the side walls, they obtained interfacial temperature jumps ranging from −0.28 °C to 0.34 °C. Gatapova *et al.*[24] used a specially manufactured thermocouple with a bead size of 4 μm to study the temperature distribution across an evaporating water film into the air at atmospheric pressures. By changing the heating rate of the liquid film from the bottom, they could measure interfacial jumps ranging from −0.031 °C to 0.192 °C. They compared their results with those predicted by KTG and found that the predicted values were 3–4 orders of magnitude smaller. As one of the possible explanations for this disagreement, they suggested that the accuracy of the thermocouple measurement might not be sufficient to provide precise information inside the Knudsen layer.

As reviewed above, the magnitudes of the temperature jumps determined experimentally from the thermocouple measurements are in strong disagreement with KTG. The two other

theoretical expressions (SRT and NET) predict P^V within the experimental uncertainty when the measured T^{LI} and T^{VI} are introduced into them. However, they would also do so by using different values of T^{VI} and therefore different values of the jumps. Thus, to date, the magnitude (and perhaps the direction) of the temperature jump at the interface does not have a firm theoretical grounding and is open to question.

It should be noted that in all of the experimental studies in the past three decades on the temperature jumps at a liquid–vapor interface, thermocouples have been used to measure the interfacial temperatures. Since thermocouples measure a voltage difference rather than the temperatures, they require a standard calibration process to find the relation between the voltage and the temperature at the junction when it is submerged in a calibrating liquid. When the calibrated thermocouple is used to measure the temperature of an object (including fluids) of a certain temperature T^f, it is assumed that the temperature of the junction is identical to its temperature when it measured the temperature of the calibrating liquid at T^f. However, this usually does not happen due to the different heat transfer conditions in the measurements compared to the calibration process. The different conditions generally arise from: (i) heat conduction through the wires to the bead (or vice versa),[25–28] (ii) radiative heat exchange between the thermocouple and the environment,[29–31] and (iii) poor contact between the bead and the object whose temperature is to be measured.[32,33] In the measurements of the interfacial temperatures at a liquid–vapor interface, in addition to these three factors, two more issues may arise: (iv) the difficulty in measuring the temperatures in the Knudsen layer due to the relatively large size of the thermocouple bead (recall that KTG predicts a sharp temperature variation in this layer) and, (v) the difference between the thermocouple and the vapor temperatures due to the rarefaction effects, where the number of collisions between the molecules and the solid thermocouple becomes comparable to the number of collisions between the vapor molecules. This creates a discontinuity between the solid and the vapor temperature. The rarefaction effects become more pronounced at low pressures and have not yet been considered or quantified as a source of uncertainty in the previous evaporation studies at low pressures.

By examining the results of the existing studies on the interfacial temperature measurements using a thermocouple, two intriguing questions remain unanswered. First of all, why are the jumps measured at atmospheric pressures much smaller than those measured at low pressures? A possible

justification for this is provided by KTG which indicates that the jump is directly proportional to the mass flux at the interface and since the mass flux is higher at low pressures, the measured jumps are larger. However, one may argue that this can also be as a result of rarefaction effects in the vapor at low pressures, which cause the thermocouple readings to deviate from the true temperature of the vapor. Secondly, why are the jumps measured at high temperature gradients above the interface significantly larger than those obtained at small temperature gradients? To answer this question based on the existing theories, we can mention the prediction of KTG which indicates that the jump is directly proportional to the heat flux from the vapor to the interface and since a higher heat flux occurs at a higher temperature gradient, the measured jumps should be larger. However, one may argue that this can also be due to the higher conduction heat transfer to the bead from the wires when the bare parts of the thermocouple are exposed to a large temperature gradient above the interface. Therefore, a quantitative study is required to isolate the sources of errors mentioned above during the temperature measurement experiments and determine what portion of the reported temperature jumps exist at the interface and what portion are only a spurious effect of the thermocouple. Accordingly, this chapter seeks to address these questions by presenting a mathematical model of a thermocouple when it is being utilized in a typical temperature measurement experiment across an evaporating liquid–vapor interface. The experimental study of Badam *et al.*[4,19] is selected for our numerical study since their work covers a broad range of temperature jumps (1.83–27.83 °C) at the interface. Also, due to their inclusion of vapor–phase heating, the magnitudes of the jumps are quite large compared to those reported by other researchers for the same liquid. This will give more confidence to the conclusions drawn from the simulation results as the conclusions made from the simulation results of small jumps are prone to be misleading due to the possible influence of simplification of the real system and the errors associated with the numerical simulation. To simulate the system, the differential equations of heat transfer in the thermocouple, as well as the heat and momentum transfers in the fluids, are coupled and solved numerically subject to appropriate boundary conditions. The results are used to estimate the contribution of the thermocouples in the determination of the temperature jumps at the interface during evaporation experiments.

4.2 Description of the experimental setup of Badam *et al.*[4,19]

A schematic representation of the experimental setup used by Badam *et al.*[4,19] that we will use for our numerical model is outlined in Figure 4-1. The original evaporation experiments were performed in a vacuum chamber at low pressures in the range of 213–1077 Pa. Mass transfer occurred at the convex liquid–vapor interface which was formed above a rectangular PVC channel at a steady-state condition. Liquid from the bottom supplied the interface continuously to keep the interface position at a constant level. In the experiment, a heating element was placed 3 mm above the interface to increase the temperature (and heat flux) in the vapor phase. A 25 μm (wire diameter) K-type thermocouple consisting of two different wires (alumel and chromel) was moved vertically along the centerline and measured the temperatures in the vapor and liquid. The thermocouple wires were shaped as shown in Figure 4-1 to minimize the effect of conduction heat transfer from the wires to the bead. The thermocouple was positioned at the interface by monitoring through a cathetometer with an accuracy of ± 10 μm. When a steady-state condition was achieved (the interface height would change within ± 10 μm), the temperatures were collected. At each measuring point, they recorded a minimum of 30 temperatures and took the average as the temperature of that point. The standard deviation of the collected data at each point was reported to be less than 0.07 °C. Since the exact distance of the thermocouple to the interface was not determined in their work, we performed our study for a range of distances ranging from 0.2 μm to 30 μm. The results in the following sections are demonstrated for a typical distance of 5 μm unless otherwise a different distance is noted. The possible effect of this assumption on our conclusion about the temperature jumps at the interface will be discussed later. The domains taken into account in the modeling included the vapor in the top half of the vacuum chamber, the liquid, and the thermocouple. The presence of the heating element was not considered in the simulation. However, the effect of this part was applied as a temperature boundary condition in the model.

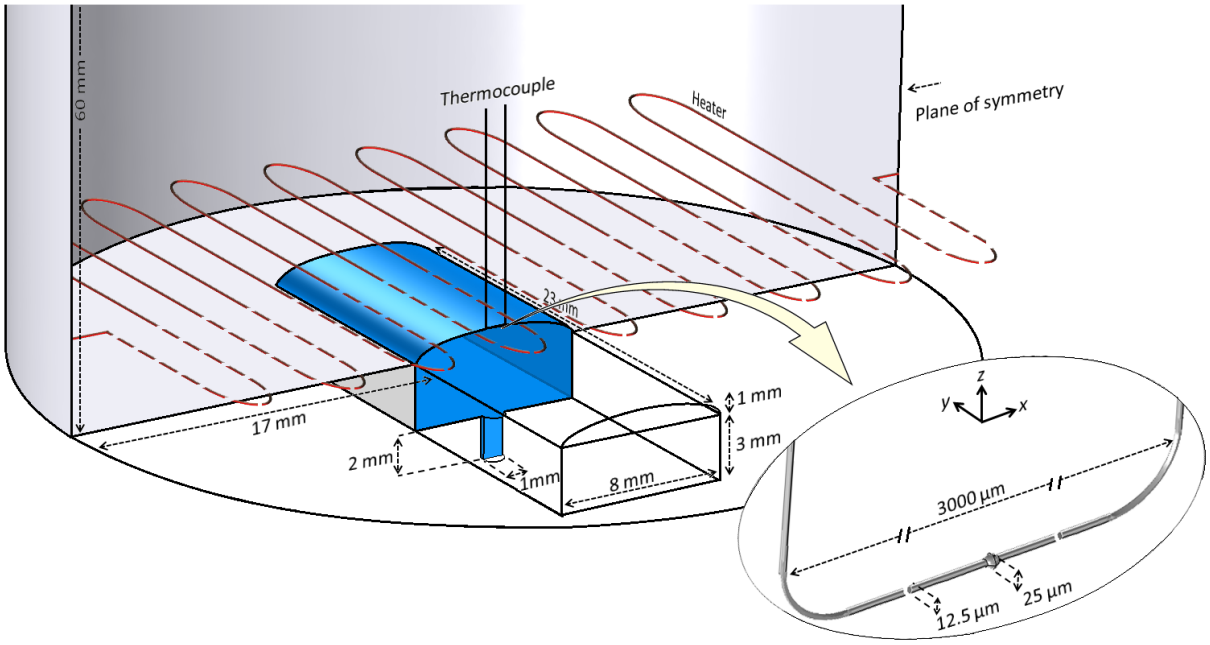

Figure 4-1 Schematic representation of the experimental setup used in the Badam *et al*. studies. The schematic diagram is drawn based on the available information in refs.4,19. The bottom plane shown here did not exist in the real setup and was only considered for facilitating the numerical simulation. The heating element was not considered in the simulation of the vapor flow. The inset shows the dimensions of the thermocouple used in our numerical simulations.

4.3 Mathematical modeling

4.3.1 Determination of the vapor flow regime

Before we proceed to describe the relevant governing equations, we need to determine which of statistical mechanics or continuum mechanics better characterizes the vapor flow. Since the selected experiments were carried out at moderately low pressures (200–800 Pa), it is possible that the continuum mechanics assumption breaks down. The degree of rarefaction of the vapor is quantified by the dimensionless Knudsen number (Kn) defined as the ratio of the molecular mean free path (λ) to the characteristic length scale of the system (l_c). Based on the values of the Knudsen number, the flow of gas is classified into four different regimes. For $Kn < 10^{-2}$ (continuum regime), the continuum assumption holds and the flow can be described by the Navier–Stokes equations with the traditional no-slip and isothermal boundary conditions. For $10^{-2} < Kn <$

10^{-1} (slip flow regime), the rarefaction effects start to become important, and the no-slip and isothermal conditions are no longer valid on the wall. In this regime, the applicability of the continuum assumption can be extended to describe the gas flow, provided that a slip velocity and a temperature jump are imposed to the wall. At intermediate Knudsen numbers, $10^{-1} < Kn < 10$ (transition regime), the rarefaction effects become dominant, and continuum assumptions (*i.e.*, the Navier–Stokes equations) become inapplicable. In this range, the molecule–molecule and molecule–wall interactions are both important. The Boltzmann equation should be used and solved with either the Direct Simulation Monte Carlo (DSMC) method, or the Discrete Velocity Method (DVM). Since these methods are computationally expensive at the early stages of the transition regime, the extended Navier–Stokes equations have also been investigated by many researchers.[34,35] At $Kn > 10$ (free molecular regime), the intermolecular collisions become negligible compared to the wall−molecule collisions and the flow of the gas is described by the collisionless Boltzmann equation in which the molecular interactions are neglected. One should note that the flow in the gas for any *Kn* may be described from the solution of the Boltzmann equation.

For the experimental conditions that are simulated in the present study, the maximum Knudsen number based on the diameter of the vacuum chamber is 8.8×10^{-4}, which falls within the continuum regime. Thus, the continuum assumption with no–slip and isothermal condition between the chamber wall and the vapor is valid. However, for the flow in the vicinity of the thermocouple which is of primary interest in this study, the choice of the vacuum chamber diameter is not the appropriate length scale. To calculate the Knudsen number based on the thermocouple dimensions, we assume that the flow around the thermocouple bead is similar to the flow past a small sphere with a diameter of d_p. By taking the bead diameter as the characteristic length, the Knudsen number may be calculated as:[36]

$$Kn_p = \sqrt{\frac{\pi\gamma}{2}}\left(\frac{M_p}{Re_p}\right), \tag{4-1}$$

where γ is the ratio of heat capacity of the vapor at constant pressure to that of the vapor at constant volume, and M_p and Re_p are the Mach number and Reynolds number which are defined as:

$$M_p = \frac{U}{\sqrt{\gamma \bar{R} T}}, \tag{4-2}$$

$$Re_p = \frac{\rho U d_p}{\mu}, \tag{4-3}$$

where U is the magnitude of the far field velocity, $\bar{R}$ is the individual gas constant (for water vapor $\bar{R}$ = 461.5 J/kg K), T is temperature, ρ is the density, and μ is the viscosity, which may be found in Table 4-1.

Combining eqs (4-1), (4-2), and (4-3), the Knudsen number simplifies to:

$$Kn_p = \frac{\mu}{\rho d_p}\sqrt{\frac{\pi}{2\bar{R}T}}. \tag{4-4}$$

The Knudsen numbers calculated based on the diameter of the bead for the selected experiments vary in the range of $0.3 < Kn < 0.8$, which falls within the early transition regime. The flow in this regime can neither be considered an absolutely continuous nor a free molecular flow. As Kn increases from 0.1 to 10, the behavior of the vapor deviates from continuum flow and approaches free molecular flow. Since the calculated values are much closer to the lower limit of the transition regime ($Kn = 0.1$), the rarefaction degree of the vapor may still be small. Herein, we will use the governing equations for the slip flow regime (the so-called Navier–Stokes–Fourier equations with a slip velocity and a temperature discontinuity at the solid–vapor boundaries). We will show in the results and discussion section that this assumption does not affect our conclusions about the simulated temperatures in liquid and vapor.

4.3.2 Governing equations

The Navier–Stokes–Fourier equations are used to describe the flow field and temperature distribution in the fluids. The maximum Mach number in the liquid phase, calculated by using the maximum estimated velocity in the liquid which occurs in the small liquid entrance, is on the order of $M \approx 10^{-6}$. Therefore, the flow of the liquid is assumed to be incompressible, and the continuity equation becomes:

$$\nabla \cdot \boldsymbol{u}^L = 0, \tag{4-5}$$

where $\boldsymbol{u}$ is the velocity vector and superscript L denotes the liquid. Although the maximum Mach number in the vapor flow (using eq (4-2)) is small ($M \approx 2 \times 10^{-3}$), the flow of the vapor may not be incompressible since the density variation in the vapor in certain experimental conditions was 46%. Thus, the continuity equation in the vapor assuming a steady-state compressible flow is:

$$\nabla \cdot (\rho^V \boldsymbol{u}^V) = 0, \tag{4-6}$$

where superscript V denotes the vapor. Based on the above arguments, the momentum transfer equations in the liquid and vapor are given respectively by:

$$\rho^L (\boldsymbol{u}^L \cdot \nabla)\boldsymbol{u}^L = \nabla \cdot [-P\boldsymbol{I} + \mu^L(\nabla \boldsymbol{u}^L + (\nabla \boldsymbol{u}^L)^{tr})] + \rho^L \boldsymbol{g}, \tag{4-7}$$

$$\rho^V (\boldsymbol{u}^V \cdot \nabla)\boldsymbol{u}^V = \nabla \cdot \left[-P\boldsymbol{I} + \mu^V(\nabla \boldsymbol{u}^V + (\nabla \boldsymbol{u}^V)^{tr}) - \frac{2}{3}\mu^V(\nabla \cdot \boldsymbol{u}^V)\boldsymbol{I}\right] + \rho^V \boldsymbol{g}, \tag{4-8}$$

where P is the pressure, $\boldsymbol{I}$ is the identity matrix, $\boldsymbol{g}$ is the gravitational acceleration vector. The superscript *tr* means transposed. Eqs (4-7) and (4-8) are derived for laminar flow of a viscous fluid. To check the validity of the laminar assumption, the local Reynolds number (*Re*) in each computational element everywhere in the liquid and vapor was calculated using the ratio of the inertial terms to the viscous terms in the Navier–Stokes equations. It was found that the *Re* was always smaller than 0.018 in the liquid and 0.025 in the vapor. Therefore, the flows in both phases are dominated by viscous terms, and the assumption of laminar flow is reasonable. It should be mentioned that the *Re* number could also be calculated by using the diameter of the thermocouple junction as the characteristic length. The maximum values of Re_p based on this assumption were calculated as well and found to be 7×10^{-3} in the liquid and 5×10^{-3} in the vapor, which confirms that the flow in the fluids is laminar.

Heat transfer in the fluids is assumed to occur by conduction and convection mechanisms and is given by:

$$\rho C_P \boldsymbol{u} \cdot \nabla T = \nabla \cdot (k \nabla T), \tag{4-9}$$

where C_P is the heat capacity at constant pressure and k is the thermal conductivity. In the solid domain, heat propagates only through the conduction mechanism, thus:

$$\nabla \cdot (k \nabla T) = 0. \tag{4-10}$$

In eqs (4-9) and (4-10), the heat flux is related to the temperature gradients via Fourier's law of heat conduction.

4.3.3 Boundary conditions

The system of differential equations should be supplemented with appropriate boundary conditions.

4.3.3.1 The thermocouple

For the part of the thermocouple which is in contact with the vapor, the velocity slip condition proposed by Maxwell[37] is applied:

$$\boldsymbol{u}^V - \boldsymbol{u}^W = \left(\frac{2-\alpha}{\alpha}\right)\frac{\lambda}{\mu^V}\boldsymbol{\tau}_{n,t} + \frac{\alpha_T \mu^V}{\rho^V T^V}\nabla_t T^V, \tag{4-11}$$

where $\boldsymbol{u}^W$ is the velocity of the wall (in our case, the wall velocity is zero), α is the tangential momentum accommodation coefficient (assumed to be 1 in this study), λ is the mean free path of the vapor molecules, $\boldsymbol{\tau}_{n,t}$ is the tangential component of the normal shear stress, α_T is the thermal slip coefficient (assumed to be 1 in this study), and ∇_t denotes the tangential gradient. The mean free path of the vapor molecules may be calculated by:

$$\lambda = \frac{\mu^V}{\rho^V}\sqrt{\frac{\pi}{2\bar{R}T^V}}. \tag{4-12}$$

In a similar fashion, a temperature jump at the solid–vapor boundaries may be imposed based on the Smoluchowski[38,39] temperature jump condition:

$$T^V - T^W = \left(\frac{2-\sigma_T}{\sigma_T}\right)\frac{2\gamma\lambda}{(\gamma+1)Pr}\nabla_n T^V, \tag{4-13}$$

where T^W is the solid temperature at the solid–vapor boundary, σ_T is the energy accommodation coefficient, $Pr = C_P^V \mu^V / k^V$ is the Prandtl number of the vapor, and ∇_n is the normal gradient at the solid–vapor boundary. The radiation heat transfer between the thermocouple and the environment, including the radiation from the hot heating element to the thermocouple and the radiation from the thermocouple to the colder liquid interface, are neglected (see Appendix G for a quantitative proof that radiation can be neglected). At the part of the thermocouple that is submerged in the liquid, a no-slip ($\boldsymbol{u}^V = \boldsymbol{u}^W$) and isothermal ($T^V = T^W$) condition is assumed. However, it is well recognized that an interfacial thermal resistance (also known as the Kapitza resistance) exists at solid–liquid boundaries which results in a temperature discontinuity. The Kapitza resistances at the metal water surfaces, including nickel (which makes up more than 90% of the thermocouple wire) are on the order of 10^{-9} ($\mathrm{m^2K/W}$).[40,41] In the simulation, the heat fluxes between the solid and the liquid were on the order of 10 ($\mathrm{W/m^2}$). This will create a negligible temperature discontinuity ($\sim 10^{-8}$ K) between the thermocouple and the liquid. Therefore, we assumed thermal equilibrium between the liquid and the thermocouple.

At the end of the thermocouple wires, the temperature was set to zero since the thermocouple cold junctions were connected to an ice point cell in the experiments of Badam *et al.*[4,19]. As the thermocouple wire length is much larger than the wire diameter and the length of the horizontal section, this boundary condition may be written as:

$$z \to \infty \ , \ T = T_0, \tag{4-14}$$

where z is the vertical direction along the wire and T_0 is the temperature at the end of the wires. However, we need to define a finite length to be able to implement this condition in the simulation. Thus, only a small portion of the wire length is considered in the simulation and the boundary condition in eq (4-14) becomes:

$$z = z_\infty \ , \ T = T_0. \tag{4-15}$$

The value of z_∞ in this study is found such that beyond this length, the average temperature of the thermocouple bead doesn't change (numerically changes less than 0.01 °C).

Finally, at the insulated part of the thermocouple, the heat flux is set to zero ($-k\nabla T = 0$). The analysis of the results showed that this boundary condition had no effect on the simulated temperatures shown by the thermocouple, neither when the bead was in the liquid nor when was it in the vapor. In fact, the analysis was performed for two limiting cases, completely bare wires ($-k\nabla T \neq 0$), and absolutely insulated wires ($-k\nabla T = 0$) and no remarkable changes (less than 0.01 °C) were detected in the thermocouple reading. Therefore, the latter was selected in this study.

4.3.3.2 Vapor and vacuum chamber

At the chamber wall, the velocity slip condition shown by eq (4-11) was imposed. Also, it was assumed that no heat transfer between the environment and the inside vapor flow occurred. This assumption is reasonable since the chamber was made up of Perspex which has a very small thermal conductivity (~ 0.18 W/(m K)). The possible low heat transfer from/to the outside would not change the results since our focus is on the thermocouple bead temperature which is placed far away from the chamber wall.

At the vapor side of the liquid–vapor interface, the temperature and the normal component of the velocity are specified:

$$T^V = T_{sim}^{VI}, \tag{4-16}$$

$$u_n^V = m_0^{"}/\rho^V, \tag{4-17}$$

where T_{sim}^{VI} is the simulated temperature of the vapor at the interface, u_n^V is the normal component of the vapor velocity at the interface, and $m_0^{"}$ is the local evaporation flux. As will be explained in more detail in the following sections, finding T_{sim}^V is the main purpose of this study and will be accomplished using an iterative procedure. At the outlet, the normal stress and the temperature are:

$$\left(-P\boldsymbol{I} + \mu^V(\nabla \boldsymbol{u}^V + (\nabla \boldsymbol{u}^V)^{tr}) - \frac{2}{3}\mu^V(\nabla \cdot \boldsymbol{u}^V)\boldsymbol{I}\right) \cdot \boldsymbol{n} = -P^V \boldsymbol{n}, \tag{4-18}$$

$$T^V = T^{out}, \tag{4-19}$$

where $\boldsymbol{n}$ is the unit normal vector, P^V is the pressure in the vapor at the transducer, and T^{out} is the temperature of the vapor at the exit boundary.

4.3.3.3 Liquid

A detailed understanding of the flow field in the liquid during evaporation is difficult since several factors including buoyancy effects, surface tension forces, and non-uniform evaporation at the interface, determine the flow pattern in the liquid. However, since the purpose of the simulation of the liquid flow is to estimate the heat transfer between the thermocouple and the liquid, a unidirectional flow of the liquid where it enters the channel from the bottom and exits at the interface is considered. The velocity at the liquid entrance is implemented so that the mass flow entering the domain is equal to the evaporation loss. Therefore, the exit velocity at the interface is:

$$u_{out}^L = m_0^{"}/\rho^L, \tag{4-20}$$

where u_{out}^L is the normal component of the liquid velocity at the interface. The superscript L indicates the liquid phase. The entering flow should compensate the evaporating liquid at the interface, thus, from the mass balance:

$$u_{in}^L = \left(m_0^{"}/\rho^L\right)(A_I/A_{in}), \tag{4-21}$$

where u_{in}^L is the normal component of the liquid velocity at the entrance, A_I is the area of the interface, and A_{in} is the area of the liquid entrance. The entering liquid temperature was controlled in the experiments and was fixed at a constant value in the simulation:

$$T^L = T_{in}. \tag{4-22}$$

The temperature of the liquid at the interface is:

$$T^L = T_{sim}^{LI}, \tag{4-23}$$

where T_{sim}^{LI} is the simulated temperature of the liquid at the interface which should be found iteratively as explained in the next section.

4.4 Solution procedure

Figure 4-2 provides a schematic illustration to better understand the solution procedure. An iterative method was used to find T_{sim}^{LI} and T_{sim}^{VI} corresponding to each experiment. For each iteration, the experimental temperatures T_{exp}^{LI} and T_{exp}^{VI} were used to calculate the temperatures at the liquid–vapor interface.

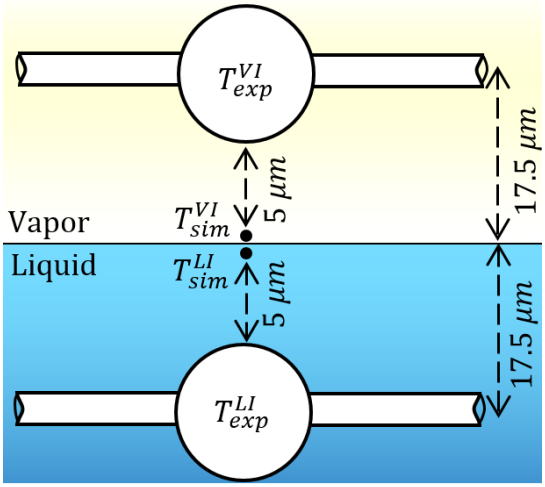

Figure 4-2 The position of the bead in the simulation when the thermocouple measures the interfacial temperatures.

Since the non-wetted part of the thermocouple exchanges heat with the vapor when the thermocouple is in the liquid, T_{sim}^{VI} was required to be able to calculate T_{sim}^{LI}. Therefore, the iterative solution started with finding T_{sim}^{VI}. In the vapor, it was assumed that the edge of the bead was as close as 5 μm to the interface so that the center of the bead was 17.5 μm above the interface. The same distance from the interface was considered for simulation of the thermocouple in the liquid. An initial value for T_{sim}^{VI} was assumed and changed until T_{exp}^{VI} equated to the experimentally measured temperature in the vapor. Then the thermocouple was moved to 3 mm above the interface where the experimental temperature was known, and the temperature at the top boundary, T^{out}, was changed until the bead temperature equated to the experimental value at 3 mm. The thermocouple was brought back and forth between these two points and the values of T_{sim}^{VI} and T^{out} were updated at each iteration, until no further changes in T_{sim}^{VI} and T^{out} were observed. In this case, T_{sim}^{VI} was considered as the interfacial temperature at the vapor side. To find T_{sim}^{LI}, the

calculated temperatures in the vapor were used and T_{sim}^{LI} was found iteratively in a similar manner to the vapor temperatures. The physical properties of the liquid, vapor, and solids used in the simulations are provided in Table 4-1. Also, the experimental pressures, temperatures, and evaporation fluxes used in the simulation are listed in Table 4-2.

Table 4-1 Physical properties used in the simulation

Property value			Unit	Ref.
$\mu^L(T) = 27.1\exp(-0.0352\,T)$			Pa s	42
$\rho^L(T) = \frac{(999.84 + 16.945T - 7.99\times10^{-3}T^2 - 46.17\times10^{-6}T^3 + 105.56\times10^{-9}T^4 - 280.54}{1 + 16.88\times10^{-3}T}$			kg/m^3	43
$k^L(T) = (T/228 - 1)^{0.18}$			W/(m K)	44
$C_p^L = 2.98806\times10^7 - 548720\,T + 4031.78\,T^2 - 14.8134\,T^3 + 2.7215\times10^{-2}\,T^4 - 2\times10^{-5}\,T^5$			J/(kg K)	45
$\mu^V(T) = \left(10^{-4}\sqrt{T/647.096}\right)(1.67752 + 1426.601/T + 2.6659\times10^5/T^2 - 6.5465\times10^7/T^3)^{-1}$			Pa s	46
$C_P^V(T) = (1875.711 - 3.465\times10^{-1}T - 5.919\times10^{-4}T^2 + 7.240\times10^{-6}T^3)$			J/(kg K)	46
$k^V(T) = 0.0088 - 10^{-5}T + 1.4\times10^{-7}T^2$			W/(m K)	46
$\rho^V = P/\bar{R}T$			kg/m^3	
Alumel	Chromel	Junction†		
$k = 29.7$ $\rho = 8600$ $C_P = 523.3$	$k = 19.2$ $\rho = 8730$ $C_P = 448.0$	$k = 24.4$ $\rho = 8665$ $C_P = 485.6$	W/(m K) kg/m^3 J/(kg K)	47

† The physical properties of the junction are assumed to be the average of Alumel and Chromel.

Table 4-2 Experimental conditions extracted from ref. 19.

Experiment No.	Heater Temperature (˚C)	P^V (Pa)	$m_0^{"}$ (kg/m^2 s)‡	T_{exp}^{VI} (°C)	T_{exp}^{LI} (°C)	Jump (°C)
1	off	561.0	2.686×10^{-4}	0.73	−1.10	1.83
2	30	569.5	3.679×10^{-4}	2.93	−0.91	3.84
3	50	572.4	5.007×10^{-4}	6.37	−0.92	7.29
4	80	569.2	7.792×10^{-4}	10.84	−0.77	11.61
5	100	760.3†	5.310×10^{-4}	13.76	3.09	10.67
6	150	676.3†	8.940×10^{-4}	20.3	1.54	18.76
7	175	394.0†	2.271×10^{-3}	20.84	−5.62	26.46
8	200	510.9†	1.918×10^{-3}	25.68	−2.14	27.82

† The pressures are corrected by SRT due to the pressure transducer failure in the experiments. See ref. 48 for details.
‡ Local evaporation fluxes are extracted from ref. 48.

4.5 Results and discussion

Using the finite element method provided in a commercial software (COMSOL Multiphysics®, COMSOL Inc.),[49] the governing equations were solved numerically subject to the boundary conditions. To make sure that the results were not dependent on the mesh size, a mesh convergence test was carried out for each numerical study. The mesh refinement continued until the average temperature of the bead would change by less than 0.01 °C.

4.5.1 Model validation

During the iterative procedure, only the experimental temperatures at the interface and those at 3 mm above the interface were used to find T_{sim}^{LI} and T_{sim}^{VI}. Although studying the temperature profiles in the vapor is not the main purpose of this study, the vapor temperature profile is required to calculate the heat transfer between the thermocouple and the vapor when the thermocouple bead is at the interface. As a result, it is not important that the temperature profiles in the middle region exactly match the experimental temperatures. However, we can see how close the simulation predicts the middle temperatures in the vapor by using the calculated T_{sim}^{VI} as a boundary a condition. The simulated temperatures of the bead at different distances from the interface are shown in Figure 4-3. As can be seen, the simulated and experimental temperatures are in fairly good agreement. It should be noted that the experimental data in the middle for the intermediate points were extracted from the plots in ref. 4 using plot digitizing software. However, the numerical values of T_{exp}^{LI} and T_{exp}^{VI}, which were used in calculating T_{sim}^{LI} and T_{sim}^{VI} iteratively in the previous section, were reported in ref. 4.

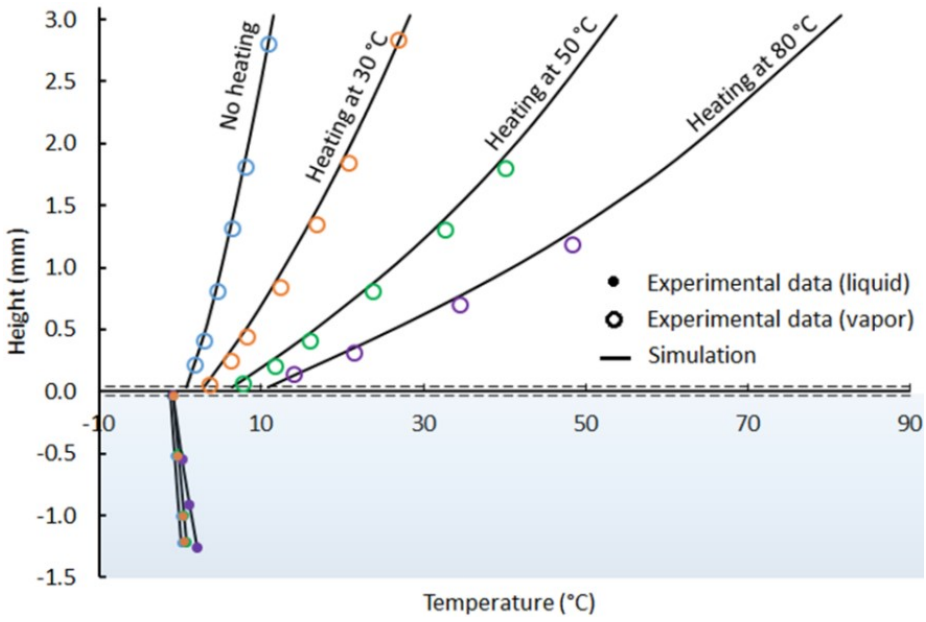

Figure 4-3 Comparison between the experimental and simulated temperatures of the bead.

4.5.2 Velocity field

Figure 4-4 shows the effect of the thermocouple on the simulated velocities of the liquid and vapor in a typical evaporation experiment. The panels on the left show the undistorted simulated velocities in liquid and vapor. The panels on the right show the distorted velocity fields in the presence of the thermocouple. As shown in Figure 4-4a and Figure 4-4b, the thermocouple changes the velocity in the vapor significantly. In the presence of the solid wires, the velocity of the vapor decreases near the leads but does not vanish completely due to the rarefaction and thermal creep effects (see eq (4-11)). This leads to developing a boundary layer around the thermocouple wires as vapor travels upward. Figure 4-4c and Figure 4-4d show that the velocity field in the liquid is also affected when the thermocouple is immersed. As noted earlier, the velocity of the liquid may differ from the simulated velocities to some extent in our study due to several factors. It is worth evaluating the effect of the distorted flow of the liquid and vapor on the temperature measurements. The dimensionless Péclet number (*Pe*), which is defined as the ratio of the convective heat transfer to the conductive heat transfer in a flowing fluid, provides a quantitative estimate of the contribution of each mechanism of heat transfer in the fluids. At low *Pe*, conduction heat transfer predominates. The values of *Pe* in all simulations were calculated in each computational element

everywhere in the liquid and vapor by calculating the ratio of the conductive heat transfer $\left(\nabla \cdot (k\nabla T)\right)$ to the convective heat transfer $\left(\rho C_p \boldsymbol{u} \cdot \nabla T\right)$ in eq (4-9). The maximum Péclet numbers in the liquid and vapor corresponding to the highest evaporation rate experiment were found to be 0.11 and 0.025 respectively. The value of 0.11 in the liquid occurred in the entrance channel far from the thermocouple due to the high velocity in that region. The *Pe* decreases rapidly at the end of the entrance channel and almost vanishes in the vicinity of the thermocouple. Thus, it can be said that most of the energy transfer in the fluids occurred through the conduction mechanism, and the convection heat transfer by the fluid flows plays a minor role in the distribution of the temperature field.

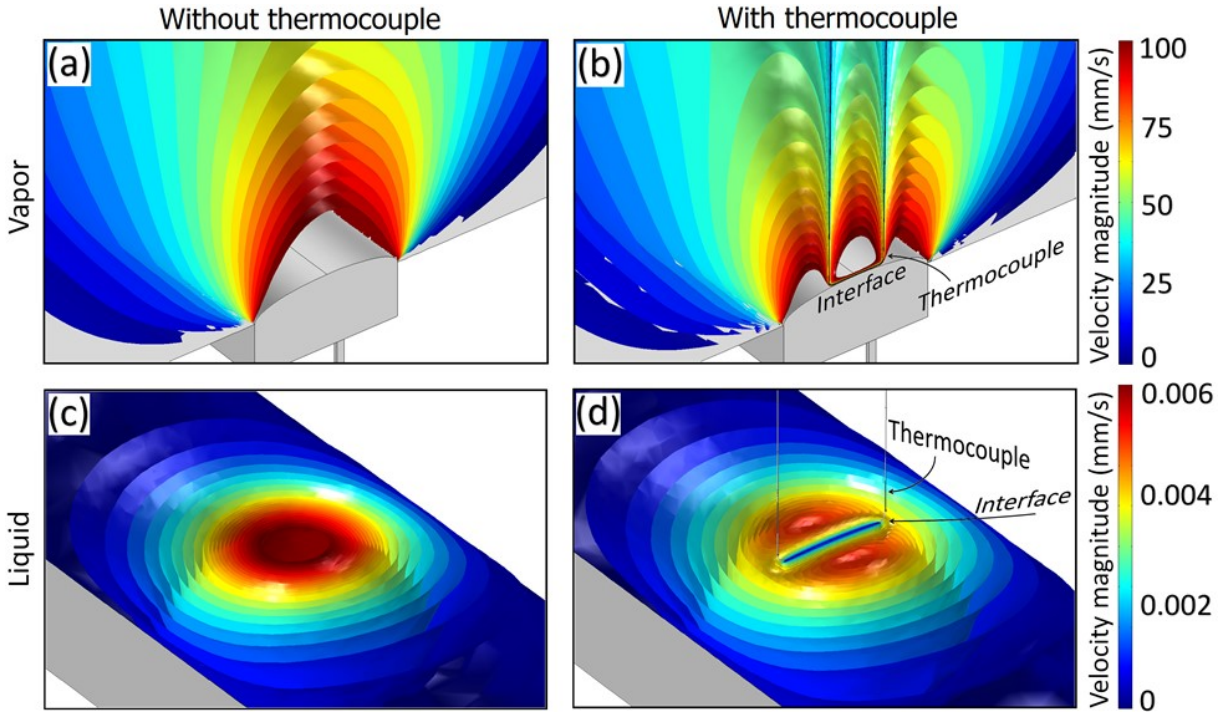

Figure 4-4 The effect of the thermocouple on the simulated velocity distribution in the vapor (a,b) and in the liquid (c,d) when the thermocouple measures the interfacial temperatures. Only half of the vapor is shown in (a,b) for a better illustration. Note the different scales of the velocity magnitudes in liquid and vapor.

4.5.3 Interfacial temperatures

The main concern regarding temperature measurements at the liquid−vapor interfaces by a thermocouple is to understand whether the temperature of the bead when it measures the temperature of the fluids at T^f is the same as the temperature of the bead if it was placed in the calibrating liquid at T^f. This may not happen, especially in the vapor phase, due to several reasons. First, it is probable that the thermocouple readings are affected by conduction heat transfer through the wires. The temperature profiles in the vapor in the Badam *et al.* experiments have undergone a sharp variation in a small distance above the interface (up to 58.1 °C/mm). As was shown earlier, the conduction heat transfer in all phases determines the temperature distribution in the fluids and solid. Since the thermal conductivities of the metals are much larger than those of the fluids, heat can propagate through the wires more easily than it can through the fluids and causes the bead temperature to differ significantly from the temperature of the surrounding fluid. Second, the rarefaction effects, which become conspicuous at low pressures, may prevent a thermal equilibrium between the solids and the vapor and lead to an incorrect measurement in the vapor. Third, in practice, the bead can not get too close to the interface due to the vibration of the interface (in the Badam *et al.* experiments, the interface position was controlled within an accuracy of ±10 μm) which requires a small distance always be maintained between the edge of the bead and the interface while measuring the interfacial vapor temperatures. Otherwise, the liquid sticks to the bead and disturbs the measurements in the vapor. Also, even if the bead could just reach the interface without contacting the liquid, a temperature difference between the top and the bottom of the bead might disturb the results.

By taking all of the mentioned factors into account, the interfacial temperatures of the liquid and vapor (T_{sim}^{LI}, T_{sim}^{VI}) are obtained from the simulation and are shown in Figure 4-5. Figure 4-5a shows the difference between the experimental readings of the thermocouple (T_{exp}^{LI}) and the simulated temperatures of the liquid at the interface (T_{sim}^{LI}). The horizontal axis in Figure 4-5a shows the temperature of the heater above the interface which was controlled at each experimental condition. Therefore, each data point corresponds to a specific experiment. As can be seen in Figure 4-5a, when the thermocouple bead is submerged in the liquid, the difference between T_{exp}^{LI} and T_{sim}^{LI} is negligible (~ 0.01 °C). Moreover, as the temperature of the heating element in the

vapor rises up to 200 °C, the difference between the bead temperature and the liquid temperature does not change. This implies that the thermocouple readings in the liquid are not influenced by the heat transfer from the hot vapor to the portion of the thermocouple which is not submerged in the liquid. This is reasonable since at the chamber pressures, the density and the thermal conductivity of the liquid are much larger than those of the vapor ($\rho^L/\rho^V \approx 10^6$, $k^L/k^V \approx 35$). As a result, heat transfer between the liquid and the thermocouple dominates the heat transfer between the vapor and the thermocouple.

Figure 4-5b shows the difference between the experimental temperature of the bead T_{exp}^{VI} and the predicted temperature of the vapor at the interface, T_{sim}^{VI}. When the thermocouple is at the interface, the bead shows a higher temperature due to the reasons discussed earlier. The blue data include the combined effects of rarefaction in the vapor, heat conduction through the wires, and inaccessibility of the interface by the thermocouple during the measurements. As the heating element becomes warmer, the difference between T_{exp}^{VI} and T_{sim}^{VI} becomes larger. If all of these effects are taken into account (blue data), the simulation predicts that the experimentally obtained temperatures of the vapor at the interface may differ by up to 10 °C from the real temperature of the vapor at the interface. To split the contribution of each factor in this erroneous reading, the following procedure was performed respectively in the simulation. First, the rarefaction effects (eq (4-13)) were applied and the blue data which include all three effects were calculated. Second, the rarefaction effects were ignored and thermal equilibrium between the solid–vapor boundaries was assumed. By doing this, the simultaneous effect of heat conduction through the wires and the distance of the bead from the interface could be found. This gave the red data points. Finally, the thermocouple was eliminated from the model and the temperatures of the vapor 17.5 μm above the interface, where the center of the bead would be, were calculated and the yellow data were obtained. This gave an estimate of how much the bead temperature would have differed from T_{sim}^{VI} due to measuring the temperature at a distance which is 17.5 μm far from the interface. As Figure 4-5b suggests, all three factors, although not equally, play a role in the erroneous temperature measurements in the vapor. The rarefaction effects contributed almost half of the incorrect reading of the vapor temperature. By increasing the heater temperature, the contribution of the rarefaction effects became even more pronounced.

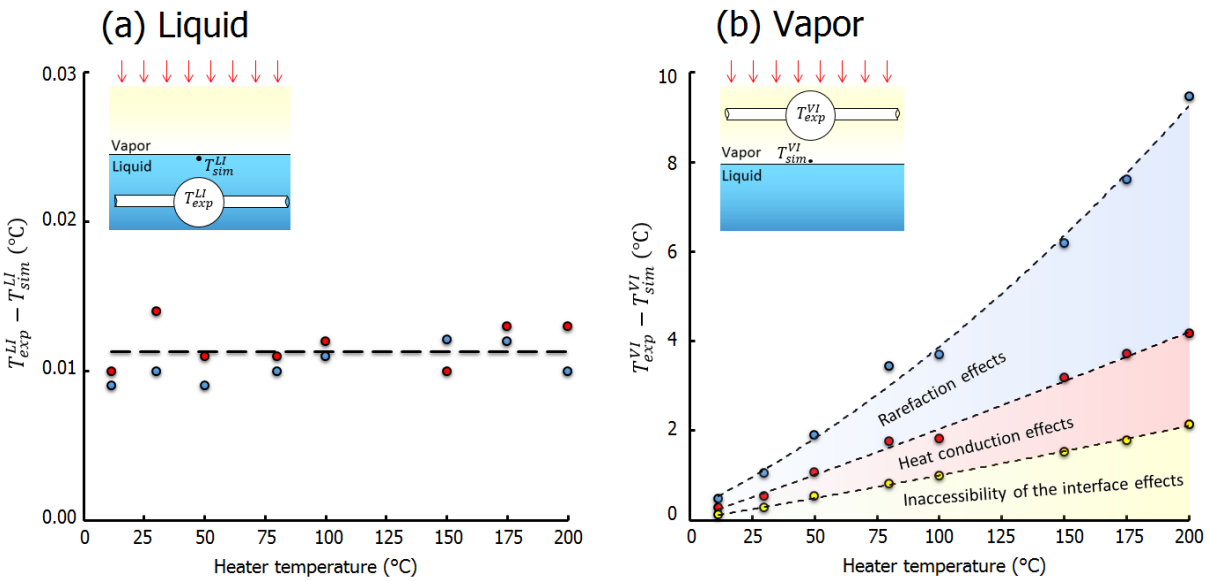

Figure 4-5 Comparison of the interfacial temperatures obtained from the experiments and simulations. (a) Deviation of the simulated temperatures from the experimental readings of the thermocouple when the thermocouple is in the liquid at the interface. The red data show the deviation when thermal equilibrium is assumed between the vapor and the portion of the thermocouple which is outside the liquid. The blue data show the deviation when the temperature at the solid–vapor boundary is not continuous, as described in eq (4-13). The dashed line shows the average of all data points. (b) Deviation of the simulated temperatures of the vapor at the interface from the experimental readings of the thermocouple when the thermocouple is in the vapor at the interface. The blue data show the deviation when the temperature at the solid–vapor boundary is not continuous, as described in eq (4-13). The red data show the deviation when thermal equilibrium is assumed at solid–vapor boundaries. The yellow data show the difference between the temperature exactly at the interface and that at some distance above the interface where the center of the bead would be located if the thermocouple were in the vapor.

To demonstrate the effect of the thermocouple on the temperature jumps measured by the thermocouple, a parity plot which compares the experimentally measured jumps ($T_{exp}^{VI} - T_{exp}^{LI}$) against the predicted jumps ($T_{sim}^{VI} - T_{sim}^{LI}$) is provided in Figure 4-6. It can be seen that for all experiments, the predicted jumps fall under the identity line, which means that the predicted jumps are smaller than those measured experimentally by the thermocouple. The slope of the best-fit line to the data (assuming $\sigma_T = 1$) is 0.68. This suggests that the measured temperature jumps have been overestimated by at least 32% as a result of incorrect temperature readings in the vapor, and that the real jumps should be 68% of those measured in the experiments. It should be noted that

this approximation is constructed based on simulation results in which the energy accommodation coefficient, σ_T, was assumed to be unity. This is the condition that holds for a completely diffuse reflection of molecules at the solid walls.

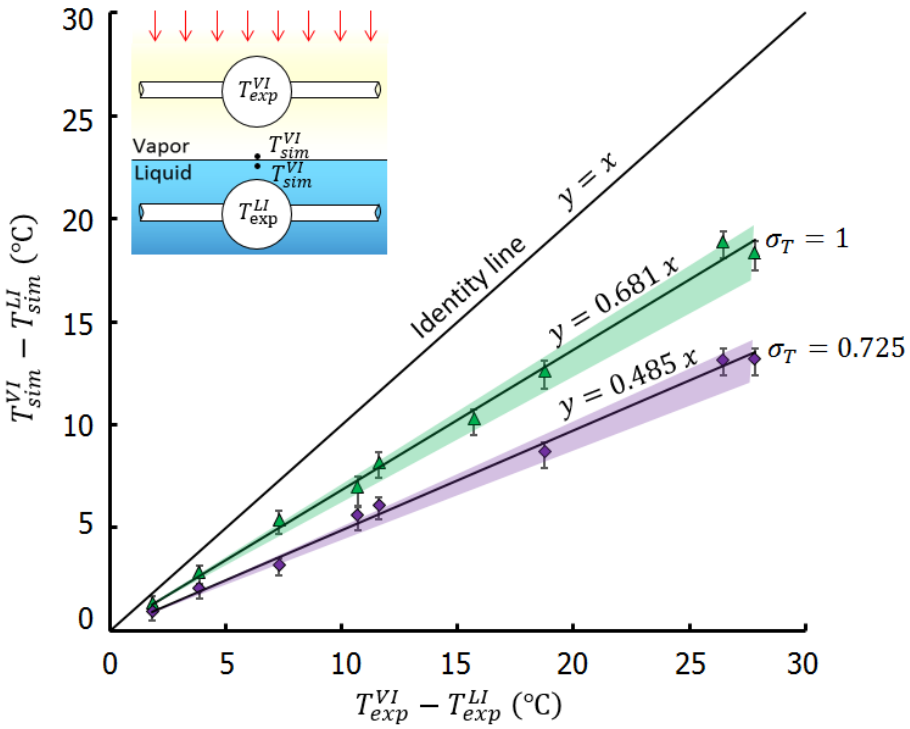

Figure 4-6 Comparison between the experimental and predicted temperature jumps at the interface for two values of energy accommodation coefficient, σ_T. As σ_T becomes smaller, the temperature jumps obtained from the simulation deviate further from the temperature jumps experimentally measured by the thermocouple. The inset shows the location of the temperatures $T_{exp}^{VI}, T_{exp}^{LI}, T_{sim}^{LI}, T_{sim}^{VI}$. The data points show the simulated temperature jumps when the thermocouple bead is 5 μm above the interface. The error bars show the range within which the simulated temperature jumps fall as the position of thermocouple in the simulation was varied between 0.2–30 μm from the interface. The green and the purple areas show how much the slopes of the fitted line change as a result of this variation. The minimum and maximum slopes of the fitted lines for $\sigma_T = 1$ are 0.623 and 0.710, and for $\sigma_T = 0.725$ are 0.437 and 0.509, respectively. The smallest slope in each region corresponds to the farthest distance of the thermocouple from the interface (30 μm).

The simulated interfacial temperatures in the vapor (T_{sim}^{VI}) deviate further from the experimental temperatures measured by the thermocouple (T_{exp}^{VI}) if the specular reflection of the vapor molecules plays a role ($\sigma_T < 1$). By reviewing several studies based on the solution of the

Boltzmann equation, Sharipov[50,51] suggested a minimum value for $(2/\sigma_T + 0.83)\sqrt{\pi}\gamma/(\gamma+1)Pr = 1.95$ to be used for polyatomic gases in practical calculations. By taking Pr = 1 assuming the vapor is an ideal gas and $\gamma = 1.33$ for water vapor, the maximum value of σ_T suggested by Sharipov is 0.725. The results for $\sigma_T = 0.725$ are also plotted in Figure 4-6. It can be seen that as σ_T is decreased from 1 to 0.725, the predicted jumps at the interface become smaller which results from the fact that the bead temperature deviates further from the surrounding vapor temperature due to the rarefaction effects. The slope of the fitted line to the data in Figure 4-6 for $\sigma_T = 0.725$ is 0.485. This means that the measured temperature jumps at the interface ($T_{exp}^{VI} - T_{exp}^{LI}$,) are overestimated by 51.5% due to the intrusion of the thermocouple in measuring the vapor temperature, and the predicted jumps at the interface ($T_{sim}^{VI} - T_{sim}^{LI}$) are estimated to be 48.5% of the measured values. It should be noted that even smaller values of the temperature jumps could be predicted by decreasing σ_T.

It was shown above that the thermocouple might not read the interfacial temperatures in the vapor correctly. It is necessary to determine whether the predicted temperatures from the simulation are in agreement with the existing theories of mass transfer, namely, KTG, NET, and SRT. The NET expression has previously been shown to be not sensitive to the interfacial vapor temperatures (see the appendix of ref. 19). For assessing the KTG, we used the equation for temperature jump which was originally proposed in ref. 2 and restated in ref. 4. Table 4-3 compares the temperature jumps predicted by KTG and those obtained from the numerical simulation after taking all influencing factors into account. As it can be seen, the simulated temperature jumps are still much larger than those calculated from KTG.

Table 4-3 Comparison between the experimental and simulated temperature jumps and the prediction of KTG.

Exp. No.	P_{exp}^{V} (Pa)	Experimental jump (°C)	Simulated jumps (°C)		Predicted jump by KTG (°C)
			$\sigma_T = 1$	$\sigma_T = 0.725$	
1	561.0±13.3	1.83	1.37	0.91	0.07
2	569.5±13.3	3.84	2.81	2.09	0.19
3	572.4±13.3	7.29	5.39	3.20	0.38
4	569.2±13.3	11.61	8.19	6.09	0.59
5	514.0±13.3†	10.67	6.98	5.59	0.47
6	306.0±13.3†	18.76	12.58	8.69	0.82
7	308.7±13.3†	26.46	18.86	13.16	1.49
8	306.5±13.3†	27.82	18.35	13.17	1.51

† The pressures in the vapor were probably measured incorrectly due to the failure of the transducer (See ref. 48).

To evaluate the compatibility of SRT with the corrected temperatures, we followed the procedure in ref. 48 and used the predicted values of the interfacial temperatures ($T_{sim}^{LI}, T_{sim}^{VI}$) and the local evaporation fluxes ($m_0^{"}$) to predict the pressure in the vapor (P^V). As listed in Table 4-4, we only noticed a slight change in the pressures calculated by SRT and all pressures fell within the experimental uncertainty of the measuring device. Therefore, the corrected temperatures did not have any discrepancy with SRT.

Table 4-4 The predicted pressures by SRT before and after applying the simulated interfacial temperatures.

Exp. No.	P_{exp}^V (Pa)	P_{SRT}^V (Pa) without correction (Duan *et al.*[48])	P_{SRT}^V (Pa) after correction (this study)
1	561.0±13.3	563.4	563.5
2	569.5±13.3	571.1	571.1
3	572.4±13.3	570.0	569.8
4	569.2±13.3	575.0	574.1
5	514.0±13.3†	760.3	758.7
6	306.0±13.3†	676.3	673.2
7	308.7±13.3†	394.0	390.5
8	306.5±13.3†	510.9	506.4

† The pressures in the vapor were probably measured incorrectly due to the failure of the transducer (See ref. 48)

4.6 Further remarks

As discussed in the mathematical modeling section, the Knudsen numbers for the experimental conditions of Badam *et al.*, fall within the range of $0.3 < Kn < 0.8$. We used the Navier–Stokes equations, subject to the slip and temperature jump condition at the walls, to describe the mass, momentum, and heat transfer in the vapor. Although these equations typically provide reasonable results in the continuum and slip flow regimes ($Kn < 0.1$), it is possible that they break down in the range of Knudsen numbers used in this study. Therefore, the validity of our results needs to be justified. First, we should note that the limits between the different flow regimes are obtained based on experimental and empirical information which is strongly dependent on the flow geometry;[52] in an analogous way the transition between laminar and turbulent flows occurs at two different Reynold numbers in a pipe and on a plate. Most of the studies based on which the classification of Knudsen numbers has been done, were performed in

microchannels. There are several studies[34,35,53] which confirm the validity of the Navier–Stokes equations combined with slip boundary conditions beyond the slip flow regime ($Kn > 0.1$). Therefore, one can not pinpoint an exact limit for Kn above which the Navier–Stokes equations become invalid and generalize it to all geometries.[54] Second, in our study, even if the Navier–Stokes equations break down, our results and conclusions about the temperature jumps measured by the thermocouple do not change since the convective heat transfer in the vapor played almost no role compared to the conduction heat transfer as the calculated Péclet number was found to be very small. This was verified by the simulation as well. For instance, in a typical study, increasing the wall slip velocity from 0.04 m/s to 0.1 m/s by manipulating α_v and α_T in eq (4-11) decreased the bead temperature by only 3.5×10^{-3} °C, which reflects a negligible effect of the vapor velocity in the heat transfer between the vapor and the thermocouple. It can also be inferred that the results are not sensitive to the evaporation fluxes used as a boundary condition in eq (4-17), which are subject to errors due to the fact that they are calculated from measuring the temperature gradients in liquid and vapor at the interface. This could be verified in the simulation by observing no significant change in the bead temperature even when the evaporation flux in eq (4-17) was changed by several percent.

Another important point which needs to be discussed is the uncertainty about the position of the thermocouple in the vapor in the experimental study of Badam *et al*. From the information they provided, one cannot determine the exact distance of the thermocouple to the interface when the thermocouple was at the interface. As was shown in Figure 4-6, our simulation only presents results for when the thermocouple edge is within 30 μm above the interface. In case the thermocouple edge was located out of this range in the Badam *et al*. experiments, the simulation results suggest that the temperature jumps at the interface would still be smaller than what we computed and in that case the thermocouples would have overestimated the jumps to a greater extent.

4.7 Conclusion

The behavior of a thermocouple when it measures the interfacial temperatures at a liquid–vapor interface was studied numerically. Using the Navier–Stokes equations and appropriate velocity and solid–vapor temperature jump conditions, the velocity and temperature distribution in the fluids and the temperature distribution in the solid were obtained. The effects of heat conduction through the wires and rarefaction of the vapor on the final temperature of the junction were taken into account. The interfacial temperatures in the liquid and vapor were found iteratively from the simulation. The results showed that the thermocouple reading of the interfacial temperature in the liquid is very close to the temperature of the liquid at the interface. However, in the vapor, the thermocouple readings were different from the actual temperatures at the interface, due to conduction heat transfer through the thermocouple wires to the junction, inaccessibility of the interface as a result of the experimental limitations, and rarefaction of the vapor which causes the temperature at the junction to be different from the temperature at the interface. As a result, the experimentally measured temperature jumps at liquid–vapor interfaces during evaporation are questionable.

For the particular study of Badam *et al.* it was estimated that the temperature jumps were overestimated by almost 50% due to the combined factors mentioned above. This was obtained by assuming that the thermocouple in their experiments was kept 5 μm above the interface. If the thermocouple was positioned at farther distances (which is not far from expectation due to the fluctuation of the interface during their measurements), then the temperature jumps at the interface would be overestimated by more than 50%, and the real jumps would be even smaller than half of the jumps that the thermocouples show.

Finally, the corrected interfacial temperatures were applied to the SRT expression for evaporation, and no disagreement was found. Although the results of this study suggest that the temperature jumps at the interface should be smaller than those measured by a thermocouple, they were not found to be small enough to explain the significant underestimation of jumps by the currently available expression obtained from KTG. Perhaps a more accurate expression for the temperature jump by KTG, which is free from the simplifying assumptions that are made to derive the currently available expression, can explain this discrepancy.

4.8 References

(1) Pao, Y.-P. Temperature and Density Jumps in the Kinetic Theory of Gases and Vapors. *Phys. Fluids* **1971**, *14* (2), 306.

(2) Cipolla, J. W. Kinetic Theory of Condensation and Evaporation. II. *J. Chem. Phys.* **1974**, *61* (1), 69.

(3) Fang, G.; Ward, C. A. Temperature Measured close to the Interface of an Evaporating Liquid. *Phys. Rev. E* **1999**, *59* (1), 417–428.

(4) Badam, V. K.; Kumar, V.; Durst, F.; Danov, K. Experimental and Theoretical Investigations on Interfacial Temperature Jumps during Evaporation. *Exp. Therm. Fluid Sci.* **2007**, *32* (1), 276–292.

(5) Shankar, P. N.; Deshpande, M. D. On the Temperature Distribution in Liquid-Vapor Phase Change between Plane Liquid Surfaces. *Phys. Fluids A* **1990**, *2* (1990), 1030.

(6) Hisatake, K.; Tanaka, S.; Aizawa, Y. Evaporation Rate of Water in a Vessel. *J. Appl. Phys.* **1993**, *73* (11), 7395–7401.

(7) Duan, F.; Thompson, I.; Ward, C. A. Statistical Rate Theory Determination of Water Properties below the Triple Point. *J. Phys. Chem. B* **2008**, *112* (29), 8605–8613.

(8) Duan, F.; Ward, C. A. Surface Excess Properties from Energy Transport Measurements during Water Evaporation. *Phys. Rev. E* **2005**, *72* (5), 56302.

(9) Ghasemi, H.; Ward, C. A. Mechanism of Sessile Water Droplet Evaporation: Kapitza Resistance at the Solid–liquid Interface. *J. Phys. Chem. C* **2011**, *115* (43), 21311–21319.

(10) Ghasemi, H.; Ward, C. A. Energy Transport by Thermocapillary Convection during Sessile-Water-Droplet Evaporation. *Phys. Rev. Lett.* **2010**, *105* (13), 136102.

(11) Ward, C. A.; Stanga, D. Interfacial Conditions during Evaporation or Condensation of Water. *Phys. Rev. E* **2001**, *64* (5), 51509.

(12) Popov, S.; Melling, A.; Durst, F.; Ward, C. A. Apparatus for Investigation of Evaporation at Free Liquid–vapour Interfaces. *Int. J. Heat Mass Transf.* **2005**, *48* (11), 2299–2309.

(13) He, B.; Duan, F. Statistical Rate Theory Approach on the Ethanol Droplet Evaporation. In *ASME 2012 Heat Transfer Summer Conference Collocated with the ASME 2012 Fluids Engineering Division Summer Meeting and the ASME 2012 10th International Conference on Nanochannels, Microchannels, and Minichannels*; ASME, 2012; pp 681–685.

(14) Persad, A. H. Statistical Rate Theory Expression for Energy Transported during Evaporation. Ph.D. Thesis, University of Toronto (2014), University of Toronto.

(15) Persad, A. H.; Ward, C. A. Statistical Rate Theory Examination of Ethanol Evaporation. *J. Phys. Chem. B* **2010**, *114* (18), 6107–6116.

(16) Fang, G.; Ward, C. A. Examination of the Statistical Rate Theory Expression for Liquid Evaporation Rates. *Phys. Rev. E* **1999**, *59* (1), 441–453.

(17) Ward, C. A.; Fang, G. Expression for Predicting Liquid Evaporation Flux: Statistical Rate Theory Approach. *Phys. Rev. E* **1999**, *59* (1), 429–440.

(18) Bond, M.; Struchtrup, H. Mean Evaporation and Condensation Coefficients Based on Energy Dependent Condensation Probability. *Phys. Rev. E* **2004**, *70* (6), 61605.

(19) Badam, V. K. Experimental and Theoretical Investigation of the Evaporation of Fluids from Free Surfaces. Ph.D. Thesis, University of Erlangen-Nuremberg (2007).

(20) Kazemi, M. A.; Nobes, D. S.; Elliott, J. A. W. Experimental and Numerical Study of the Evaporation of Water at Low Pressures. *Langmuir* **2017**, *33* (18), 4578–4591.

(21) McGaughey, A. J. H.; Ward, C. A. Temperature Discontinuity at the Surface of an Evaporating Droplet. *J. Appl. Phys.* **2002**, *91* (10), 6406–6415.

(22) Zhu, Z. Q.; Liu, Q. S. Interfacial Temperature Discontinuities in a Thin Liquid Layer during Evaporation. *Microgravity Sci. Technol.* **2013**, *25* (4), 243–249.

(23) Zhu, Z. Q.; Liu, Q. S.; Xie, J. C. Experimental Study on the Combined Evaporation Effect and Thermocapillary Convection in a Thin Liquid Layer. *Microgravity Sci. Technol.* **2009**, *21* (SUPPL. 1), 241–246.

(24) Gatapova, E. Y.; Graur, I. A.; Kabov, O. A.; Aniskin, V. M.; Filipenko, M. A.; Sharipov, F.; Tadrist, L. The Temperature Jump at Water–Air Interface during Evaporation. *Int. J. Heat Mass Transf.* **2017**, *104*, 800–812.

(25) Attia, M. H.; Cameron, A.; Kops, L. Distortion in Thermal Field Around Inserted Thermocouples in Experimental Interfacial Studies, Part 4: End Effect. *J. Manuf. Sci. Eng.* **2002**, *124* (1), 135.

(26) Attia, M. H.; Kops, L. Distortion in Thermal Field around Inserted Thermocouples in Experimental Interfacial studies–Part II: Effect of the Heat Flow through the Thermocouple. *J. Eng. Ind.* **1988**, *110* (1), 7.

(27) Lyons, B. E.; Samulski, T. V; Britt, R. H. Temperature Measurements in High Thermal Gradients: I. The Effects of Conduction. *Int. J. Radiat. Oncol. Biol. Phys.* **1985**, *11* (5), 951–962.

(28) Samulski, T. V.; Lyons, B. E.; Britt, R. H. Temperature Measurements in High Thermal Gradients: II. Analysis of Conduction Effects. *Int. J. Radiat. Oncol. Biol. Phys.* **1985**, *11* (5), 963–971.

(29) Hindasageri, V.; Vedula, R. P.; Prabhu, S. V. Thermocouple Error Correction for Measuring the Flame Temperature with Determination of Emissivity and Heat Transfer Coefficient. *Rev. Sci. Instrum.* **2013**, *84* (2), 24902.

(30) Chen, X.; Xia, X.-L.; Sun, C.; Li, Y. Numerical Analysis on the Transient Measurement of Gas Temperature in Porous Material Using Thermocouples at High Temperatures. *Int. J. Heat Mass Transf.* **2015**, *91*, 1060–1068.

(31) Fu, X.; Luo, X. Can Thermocouple Measure Surface Temperature of Light Emitting Diode Module Accurately? *Int. J. Heat Mass Transf.* **2013**, *65*, 199–202.

(32) AlWaaly, A. A. Y.; Paul, M. C.; Dobson, P. S. Effects of Thermocouple Electrical Insulation on the Measurement of Surface Temperature. *Appl. Therm. Eng.* **2015**, *89*, 421–431.

(33) He, Q.; Smith, S.; Xiong, G. Thermocouple Attachment Using Epoxy in Electronic System Thermal Measurements — A Numerical Experiment. In *2011 27th Annual IEEE Semiconductor Thermal Measurement and Management Symposium* IEEE, 2011; pp 280–291.

(34) Weng, C.; Li, W.; Hwang, C. Gaseous Flow in Microtubes at Arbitrary Knudsen Numbers. *Nanotechnology* **1999**, *10*, 373–379.

(35) Dongari, N.; Agrawal, A. Modeling of Navier-Stokes Equations for High Knudsen Number Gas Flows. *Int. J. Heat Mass Transf.* **2012**, *55* (15–16), 4352–4358.

(36) Zhang, W. M.; Meng, G.; Wei, X. A Review on Slip Models for Gas Microflows. *Microfluid. Nanofluidics* **2012**, *13* (6), 845–882.

(37) Maxwell, J. C. On Stresses in Rarefied Gases Arising from Inequalities of Temperature. *Philos. Trans. R. Soc. London* **1879**, *170*, 231–256.

(38) Smolan, M. S. von. Ueber Wärmeleitung in Verdünnten Gasen. *Ann. Phys.* **1898**, *300* (1), 101–130.

(39) Greenshields, C. J.; Reese, J. M. Rarefied Hypersonic Flow Simulations Using the Navier-Stokes Equations with Non-Equilibrium Boundary Conditions. *Prog. Aerosp. Sci.* **2012**, *52*, 80–87.

(40) Vera, J.; Bayazitoglu, Y. Temperature and Heat Flux Dependence of Thermal Resistance of Water/metal Nanoparticle Interfaces at Sub-Boiling Temperatures. *Int. J. Heat Mass Transf.* **2015**, *86*, 433–442.

(41) Vera, J. Temperature and Heat Flux Dependence of Thermal Resistance of Water/metal Nanoparticle Interfaces. Ph.D. Thesis, Rice University (2014), Rice University.

(42) Kestin, J.; Sokolov, M.; Wakeham, W. A. Viscosity of Liquid Water in the Range −8 °C to 150 °C. *J. Phys. Chem. Ref. Data* **1978**, *7* (3), 941.

(43) Kell, G. S. Density, Thermal Expansivity, and Compressibility of Liquid Water from 0 °C to 150 °C. Correlations and Tables for Atmospheric Pressure and Saturation Reviewed and Expressed on 1968 Temperature Scale. *J. Chem. Eng. Data* **1975**, *20* (1), 97–105.

(44) Benchikh, O.; Fournier, D.; Boccara, A. C.; Teixeira, J. Photothermal Measurement of the Thermal Conductivity of Supercooled Water. *J. Phys.* **1985**, *46* (5), 727–731.

(45) Archer, D. G.; Carter, R. W. Thermodynamic Properties of the NaCl + H_2O System. 4. Heat Capacities of H_2O and NaCl(aq) in Cold-Stable and Supercooled States. *J. Phys. Chem. B* **2000**, *104* (35), 8563–8584.

(46) Wagner, W.; Pruß, A. The IAPWS Formulation 1995 for the Thermodynamic Properties of Ordinary Water Substance for General and Scientific Use. *J. Phys. Chem. Ref. Data* **2002**, *31* (2), 387–535.

(47) Caldwell, F. R. *Thermocouple Materials*; U.S. Department of Commerce, National Bureau of Standards: Washington, 1962.

(48) Duan, F.; Ward, C. A.; Badam, V. K.; Durst, F. Role of Molecular Phonons and Interfacial-Temperature Discontinuities in Water Evaporation. *Phys. Rev. E* **2008**, *78* (4), 41130.

(49) *COMSOL Multiphysics® v. 5.2a,*; AB, Stockholm, Sweden, 2016.

(50) Sharipov, F. Data on the Velocity Slip and Temperature Jump on a Gas-Solid Interface. *J. Phys. Chem. Ref. Data* **2011**, *40* (2), 23101.

(51) Sharipov, F. Data on the Velocity Slip and Temperature Jump Coefficients [Gas Mass, Heat and Momentum Transfer]. In *5th International Conference on Thermal and Mechanical Simulation and Experiments in Microelectronics and Microsystems, 2004. EuroSimE 2004. Proceedings of the* IEEE, 2004; pp 243–249.

(52) Beskok, A.; Karniadakis, G. E.; Trimmer, W. Rarefaction and Compressibility Effects in Gas Microflows. *J. Fluids Eng.* **1996**, *118* (3), 448.

(53) Silva, E.; Rojas-Cardenas, M.; Deschamps, C. J. Experimental Analysis of Velocity Slip at the Wall for Gas Flows of Nitrogen, R134a, and R600a through a Metallic Microtube. *Int. J. Refrig.* **2016**, *66*, 121–132.

(54) Josyula, E.; Burt, J. *Review of Rarefied Gas Effects in Hypersonic Applications*; Air force Res. lab Wright-Patterson AFB OH: Air force research lab Wright-Patterson AFB OH, 2011.

Chapter 5: Evaporation of Water from a Meniscus in a Rectangular Cuvette

Chapter 3 describes an experimental and a numerical study to explore the evaporation phenomena in a cylindrical tube. In this chapter, is reported a similar study in a rectangular cuvette to understand more details about the evaporation phenomena that might have been lost by using a simple axisymmetric geometry. The model is validated with the experimental data and was used to explain some aspects of the evaporation phenomenon which could not be understood from the experiments alone, such as addressing the question of why a thermocapillary flow in water, in contrast to many other liquids, does not sometimes exist. Moreover, the effect of cuvette thermal conductivity on the evaporation rates, which was shown qualitatively in Chapter 3 to play a crucial role in the evaporation from the interface, has been demonstrated quantitatively.

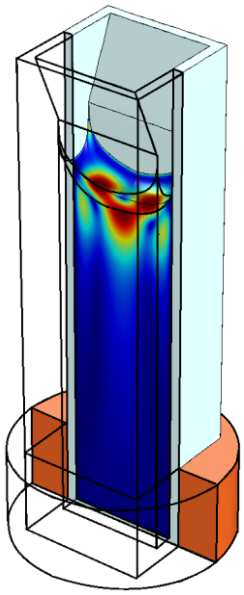

Graphical Abstract Chapter 5

5.1 Introduction

Evaporation is a ubiquitous phenomenon that takes place ceaselessly in nature and is vital to maintaining life on earth. Due to a wide range of applications, it has attracted attention from various disciplines, ranging from engineering and astronomy to biology, botany, and agriculture. Investigations on the evaporation phenomenon have increased significantly in the past few decades and have led to promising advances in the relevant technological applications such as heat pipe cooling systems,[1] ink jet printing,[2] self-assembly of nanoparticles,[3] and recently, electricity generation,[4] and evaporation-driven engines.[5] Meanwhile, fundamental studies on evaporation are still necessary as they result in innovations while developing solutions to practical problems.

Most of the experimental and theoretical studies in the literature are devoted to studying the evaporation of water droplets into noncondensable gases (*i.e.*, air) at atmospheric pressure. In this limit of evaporation, the transport of vapor molecules away from the drop often determines the conditions at the interface as well as in the bulk of the fluids.[6] Given this fact, Hu and Larson[7] derived a simple expression representing the local evaporation flux at the interface of a droplet from the solution of the Laplace equation for the vapor concentration. Sefiane and Bennacer[8] extended the expression proposed by Hu and Larson to nonisothermal conditions by incorporating the evaporative cooling effects at the droplet interface in their new model. They also defined a dimensionless number, which includes substrate and liquid properties as well as the kinetics of evaporation, to demarcate the transition from the isothermal assumption to a nonisothermal one. Hu and Larson further explored the liquid flow inside a droplet in the presence[9] and absence[10] of a Marangoni stress at the interface and provided further insights into the flow patterns induced within an evaporating droplet. This had been shown previously by Deegan *et al.*[11,12] to be responsible for leaving the coffee ring-like stain after drying a drop of suspension. By reviewing the literature on droplet evaporation at atmospheric conditions, one can find several studies that investigated the influences of various parameters including the substrate thermal properties,[13,14] substrate wettability,[15,16] substrate temperature,[17] droplet surface area,[18] relative humidity in the vapor,[19] and the asymmetry in the geometry of the drop,[20,21] on the evaporation rates and flow patterns in the liquid.

While studies on the evaporation of a liquid into a non-condensable gas have a solid grounding in the literature, the evaporation of a liquid into its vapor has not received as much attention. This is perhaps due to the complexity and difficulty associated with the experimental studies in low-pressure environments. In this limit of evaporation, the diffusion of vapor molecules usually takes place very fast and has a negligible contribution to the determination of the evaporation rate. Accordingly, the evaporation flux cannot be simply calculated from the solution of the Laplace equation of the vapor concentration. This is because the assumption of a chemical equilibrium at the interface, that was made in the previous limit, is no longer valid[6] and the concentration of the vapor at the interface is unknown. Rather, the interfacial conditions at the liquid–vapor boundary (*i.e.*, the transport of molecules across the interface and transport of energy to the interface) are the determining mechanisms of the evaporation process. To describe the

evaporation flux in this limit, the Hertz–Knudsen relation has been used for more than 130 years. However, this kinetic-theory-based expression has led to some inaccuracies and inconsistencies such as obtaining scattered evaporation and condensation coefficients for water[22] and also inconsistent predictions of the experimentally measured temperature discontinuities at the interface.[23–25]

In a series of experiments on the evaporation of water at steady-state conditions in a vacuum chamber, Ward and Fang[26] measured the temperatures across the liquid–vapor interface and found that the interfacial temperature in the vapor was always higher than that in the liquid by as much as 7.8 °C, which was not in agreement with the prediction of the Hertz–Knudsen relation. Following on from that work, in 1999, they proposed a new expression for predicting the evaporation flux based on the transition probability concept in quantum mechanics, termed statistical rate theory (SRT).[24] The newly proposed expression was consistent with the measured temperature discontinuities and could always predict the pressures of the vapor phase within the experimental uncertainty of the measurements. More importantly, no empirical constants or adjustable parameters were introduced in the new expression, something that was the Achilles' heel of previous expressions.

It was not surprising that the new SRT expression, as well as the new findings of the temperature jumps, attracted the attention of several researchers. Inspired by the theoretical study of Bond and Struchtrup[27] that demonstrated that the temperature jumps at the interface strongly depended on the heat flux from the vapor, Badam *et al.*[28,29] purposely used a heating element above the interface to verify the effect of heat flux on the temperature jumps experimentally. By doing so, they could measure temperature jumps as large as ∼28 °C in their experiments and confirmed the strong influence of the vapor heat flux on the temperature jumps. Given that all the previously reported temperature jumps were obtained using thermocouples, Kazemi *et al.*[30] numerically investigated the possibility of misinterpretation of the temperature jumps as a result of incorrect readings of the temperatures in the vapor. They found that almost half of the measured jumps obtained by Badam *et al*. could be attributed to the effect of the thermocouple itself. However, they found that the corrected temperature jumps were still consistent with the SRT expression. Ward and coworkers also applied the SRT expression by conducting experiments with other

liquids such as ethanol,[31] octane and methylcyclohexane,[23] and confirmed the consistency of the SRT expression with the measured parameters at the interface.

The authors in[32–34] highlighted that the thermocapillary flow played the major role in transferring energy to the interface. However, Thompson *et al.*[35] observed no signs of a thermocapillary flow at the same vacuum pressures even at large Marangoni numbers. Song and Nobes[36] investigated the velocity and temperature fields in the center plane of evaporating water in a rectangular cuvette at low pressures and observed a large vortical flow pattern below the interface. Recently, Kazemi *et al.*[37] studied the evaporation of water from a cylindrical cuvette at low pressures and explained the role of heat transfer in controlling the evaporation fluxes and the flow pattern in the fluids. By using a mathematical model, they demonstrated that the evaporation rates obtained in their experiments were entirely independent of choosing the expression for the evaporation flux.

Despite the remarkable progress in understanding the heat transfer aspect of the evaporation phenomenon through the past studies, the underlying physics and mechanisms involved during evaporation are not yet fully understood, and research needs to be continued in this area. The complexity of this phenomenon springs from the fact that it involves simultaneous heat, mass, and momentum transfer in the bulk fluids and at the liquid–vapor boundary. As indicated by Persad and Ward in a review article on the topic,[25] the coupling between the vapor and liquid phases in studying the evaporation phenomenon is a key factor that if neglected, as it was in the Hertz–Knudsen theory, may lead to the evaporation phenomenon being misconstrued. However, it is clear that the conditions existing at the liquid–vapor interface in real systems (including those used in experiments) are strongly coupled to the transport of mass, momentum, and energy through the bulk of the fluids to the interface. Studies such as those performed by Ward and coworkers,[23,31–35,38–40] although having shed much light on the problem by profoundly focusing on the interfacial conditions, have not provided sufficient details about the circumstances upon which these conditions occur. More specifically, questions such as: *i*) How can the flow pattern in the liquid influence the evaporation at the interface? *ii*) When does a thermocapillary flow occur at the interface? *iii*) How much does the evaporation flux depend on the thermocapillary flow? *iv*) How much does each of the heat transfer and the molecular transfer across the interface contribute to the evaporation rates? *iv*) Under what conditions is the evaporation independent of the thermal

limitation? Accordingly, in the current study, we have put our effort into addressing this gap by performing a series of experimental and numerical studies on evaporation of water from a rectangular cuvette at low pressures. In Sec. 5.1, the three-dimensional flow field below the interface is quantified using particle image velocimetry (PIV). The reliability of this technique in measuring the flow field for the specific case of evaporation of a pure liquid is discussed. Also, the temperature profiles along/across the interface are measured by a thermocouple to gain better insight into the interfacial phenomena. A mathematical model is developed in Sec. III to simulate the interactions between the phenomena occurring in the bulk phases and those taking place at the interface. The model accounts for the transport of mass, momentum, and energy in the bulk of the liquid and vapor and couples them together by assuming appropriate boundary conditions at the interface. The numerical solution of the model is validated against the experimental results and is then used to examine some features that are difficult to capture and understand solely from the experiments. This includes providing a possible answer to the question of why a thermocapillary flow in water, in contrast to many other liquids, does not always occur during evaporation. Also, it is shown quantitatively by the model how the controlling mechanism of evaporation is altered by changing the thermal conductivity of the container.

5.2 Experiments

Since the details of the experimental setup, experimental preparation and procedure, and the velocity measurement techniques are described in Chapter 2, we only summarize the main aspects of the experiments in this section.

5.2.1 Description of the experimental setup

The experimental setup, as it is shown in Figure 5-1, consists of a stainless-steel vacuum chamber (CU6-0275, Kurt J. Lesker) which was connected to a vacuum pump and equipped with four glass windows on each side to allow optical access to the interior of the chamber. The working liquid was distilled and deionized water. The liquid was degassed in a vacuum jar for 20 minutes before it was introduced into the low-pressure vacuum chamber to avoid generation of bubbles during the experiments. The cuvette (9F-Q-10, Starna Cells) containing the liquid was 45 mm high and had a rectangular cross section of 10 mm × 4 mm. The cuvette was made of quartz material

with a thermal conductivity of 3 $W/(m\,K)$.[36] The lower end of the cuvette was supported on a temperature-controlled copper block to keep the liquid temperature at the bottom of the cuvette at 4 °C.[43] This was done to make the liquid vertically stabilized and minimize the buoyancy driven flows since water has a maximum density at 4 °C.[26] The small gap between the cuvette and the copper block cavity was filled with thermal paste to improve the thermal contact between the cuvette and the block. Temperatures in the liquid and vapor were measured by a fine thermocouple (details below) which was positioned by an *XYZ* manipulator installed on top of the chamber. The horizontal position of the thermocouple was adjusted manually. The vertical / transverse motion of the thermocouple was performed by a stepper motor (Vexta PK266-03A, Velmex, Inc.) that was capable of moving the thermocouple vertically with a minimum step size of 1.25 ± 0.03 μm and was controlled and programmed using available custom code (CVI LabWindows, National Instruments Inc.). The manipulator could move the thermocouple in space with a resolution of 5 μm in each direction. The pressure inside the chamber was adjusted by manipulating a valve and was read continuously via a transducer (INFICON Porter, CDG020D) which was capable of monitoring the pressures within the range of 0–1333 Pa with an accuracy of ± 0.5% of the read value. The pressure in the chamber was reduced gradually at regular intervals to reach the desired pressure. This allowed removal of any dissolved gas gently from the liquid. The system was then allowed to operate for several minutes while the temperature of the liquid 5 mm below the interface on the centerline was monitored. Once the temperature at the measured depth changed by less than 0.01 °C, the system was assumed to have reached a pseudo steady-state, and experiments would commence with the assumption that the velocity field should have stabilized before the temperature field since the rate of momentum diffusion in water is an order of magnitude higher than the rate of thermal diffusion (Prandtl number ≈ 10).

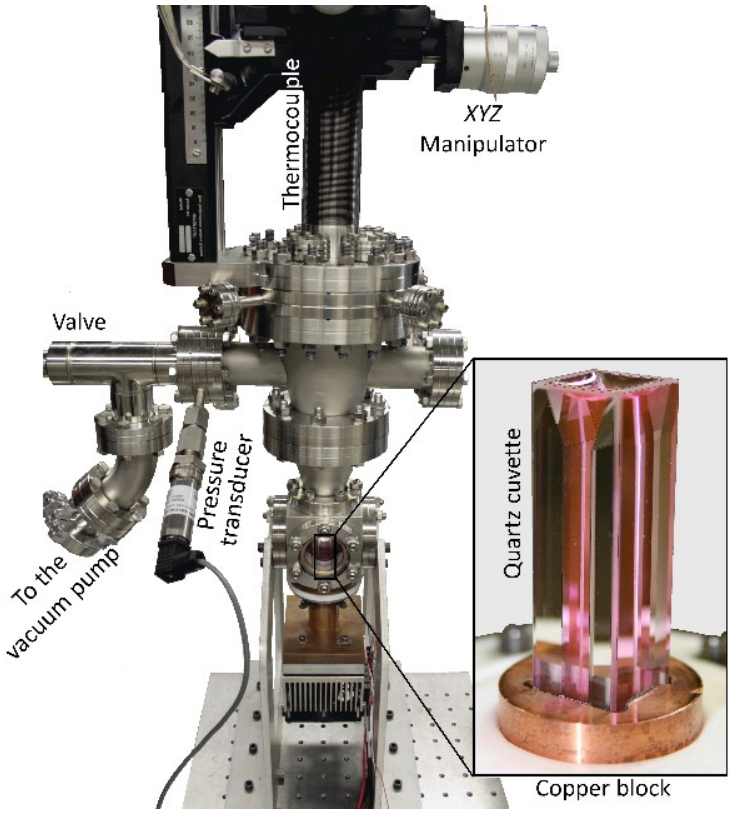

Figure 5-1 The vacuum chamber and other components used in evaporation experiments. The cuvette and copper block are magnified to enhance small details.

5.2.2 Velocity measurement

The three-component, three-dimensional (3C3D) flow field in the liquid close to the evaporating meniscus was obtained by using 3D scanning PIV which is explained in Chapter 2 and is not repeated here.

5.2.3 Temperature measurement

The temperature measurement along the vertical centerline was performed similarly to the procedure done in the cylindrical tube, which was described in section 3.2.3. However, to investigate the thermocapillary flows, the interfacial temperatures of the liquid were also measured at four points along the path from the centerline toward one of the corners. The distances of the measuring points to the centerline were 0, 1.80 mm, 3.25 mm, and 5.34 mm.

5.2.4 Evaporation flux measurement

The calculation of the experimental evaporation fluxes at different pressures is explained in section 3.2.4 and the details are not repeated here. The calculation of the interfacial area is described in Appendix D.

5.3 Mathematical Model

In this section, the system is described and a set of differential equations is formulated to mathematically describe the transport phenomena in the bulk fluids and at the interface.

5.3.1 Problem description

The problem under consideration is the evaporation of pure water into its vapor in a vacuum chamber as the pressure in the vapor is controlled and maintained at a certain value within the range of 150–900 Pa. The computational geometry as shown in Figure 5-2, includes the liquid, vapor, vacuum chamber, cuvette, and the upper part of the copper block that holds the cuvette. The cuvette has a constant rectangular cross section with dimensions of 4 mm × 10 mm × 38.6 mm with a V-shape inlet. The liquid forms a concave meniscus in the cuvette and climbs the corners due to strong adhesive forces with the hydrophilic walls. The shape of the interface was determined by using the experimental images taken from two perpendicular viewing angles. The evaporation occurs as the liquid is exposed to a low-pressure environment in the vacuum chamber. The interface is progressively cooled due to the evaporative cooling effects until the heat loss at the interface is balanced by the heat supplied to the system from the ambient. The system will then reach a pseudo steady-state condition at which the interfacial temperatures do not change further, although the interface moves down very slowly as a result of evaporation. In this study, we ignored the transition stage when the interface passes through the V-shape. Rather, we focused on the evaporation process when the meniscus moved well below the V-shape edges and no significant change in the interfacial temperatures was measured.

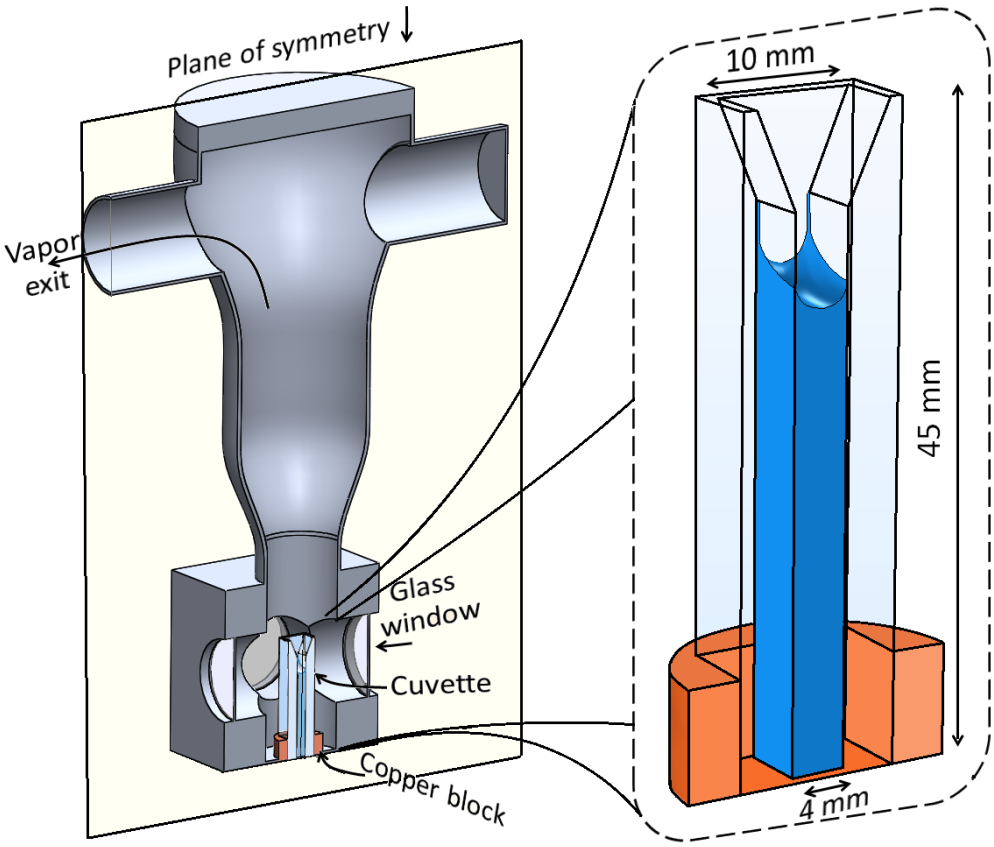

Figure 5-2 Representation of the simplified experimental setup that was studied numerically. Only half of the domain was simulated due to symmetry. The thermocouple was not included in the simulation. The cuvette and copper block are magnified to enhance small details.

5.3.2 Formulation of governing equations

The conservation laws for transport phenomena that govern the system are formulated in this section. We first present the partial differential equations in the bulk fluids and solids. Subsequently, the conditions at the boundaries that are required to complete the system of equations are explained. The equations presented in this section are similar to those used for the cylindrical tube in section 3.3.1 with the difference being that a steady state assumption is used and the motion of the interface due to evaporation is neglected.

5.3.2.1 Conservation equations in fluids and solids

In the liquid, the Mach number which is defined as the ratio of the maximum fluid velocity magnitude to the speed of sound in the fluid is very small. Therefore, the flow of the liquid can be considered incompressible, yet thermally expansible. Thus, the continuity equation is simplified to:

$$\nabla \cdot \boldsymbol{u}^L = 0, \tag{5-1}$$

where $\boldsymbol{u}$ is the velocity vector and superscript L refers to the liquid phase. By further assuming that the liquid is Newtonian and the viscous dissipation is negligible, the momentum equation can be reduced to:

$$\rho^L(\boldsymbol{u}^L \cdot \nabla)\boldsymbol{u}^L = \nabla \cdot [-P^L\boldsymbol{I} + \mu^L(\nabla\boldsymbol{u}^L + (\nabla\boldsymbol{u}^L)^{tr})] + \rho^L\boldsymbol{g}, \tag{5-2}$$

where ρ is the density, P is the pressure, $\boldsymbol{I}$ is the identity matrix, μ is the viscosity, and $\boldsymbol{g}$ is the gravitational acceleration vector. The superscript tr means transposed.

In the vapor, the assumption of incompressible flow may not hold true as the density variation in some cases was as much as 15% (assuming the ideal gas equation of state at constant pressure and using the measured temperatures in the vapor domain). Thus, the continuity equation for the vapor is expressed as:

$$\nabla \cdot (\rho^V\boldsymbol{u}^V) = 0, \tag{5-3}$$

where superscript V refers to the vapor phase. By assuming that the vapor is a Newtonian fluid and the viscous dissipation is negligible, the momentum equation becomes:

$$\rho^V(\boldsymbol{u}^V \cdot \nabla)\boldsymbol{u}^V = \nabla \cdot \left[-P^V\boldsymbol{I} + \mu^V(\nabla\boldsymbol{u}^V + (\nabla\boldsymbol{u}^V)^{tr}) - \frac{2}{3}\mu^V(\nabla \cdot \boldsymbol{u}^V)\boldsymbol{I}\right] + \rho^V\boldsymbol{g}, \tag{5-4}$$

Note that eqs (5-2) and (5-4) are derived based on the assumption of laminar flow in liquid and vapor. To check the validity of this assumption in our study, the local Reynolds number (*Re*) in each computational element, defined as the ratio of the inertial terms to the viscous terms eqs (5-2) and (5-4), was calculated. The Reynolds numbers computed by this method were always smaller than 0.021 in the liquid and 0.028 in the vapor. Therefore, the flows in both phases are dominated by viscous terms, and the assumption of laminar flow is reasonable. The temperatures in the liquid

and vapor, T^L and T^V, can be obtained from the following heat transfer convection–diffusion equations:

$$\rho^L C_p^L \boldsymbol{u}^L \cdot \nabla T^L = \nabla \cdot (k^L \nabla T^L), \tag{5-5}$$

and,

$$\rho^V C_p^V \boldsymbol{u}^V \cdot \nabla T^V = \nabla \cdot (k^V \nabla T^V), \tag{5-6}$$

where k is the thermal conductivity and C_p is the specific heat capacity at constant pressure. In eqs (5-5) and (5-6), the heat fluxes are determined by Fourier's law of conduction and the heat generated by viscous dissipation is neglected. For the solid phases, the velocity is zero and the energy balance is simplified to:

$$\nabla \cdot (k \nabla T) = 0. \tag{5-7}$$

5.3.2.2 Liquid–vapor interface

At the liquid–vapor interface, the mass balance requires that:

$$m^{"} = \rho^L \boldsymbol{u}^L \cdot \boldsymbol{n} = \rho^V \boldsymbol{u}^V \cdot \boldsymbol{n}, \tag{5-8}$$

where $m^{"}$ is the net evaporation mass flux and $\boldsymbol{n}$ is the unit normal vector at the interface which points toward the vapor. The net evaporated mass flux across the liquid–vapor interface may be calculated by using the expression proposed by Ward and Fang[24] derived from the statistical rate theory of interfacial transport (SRT) as:

$$m^{"} = 2\left(\frac{P^{sat} \exp\left(V_\infty^L (P^L - P^{sat})/\bar{R}T^L\right)}{\sqrt{2\pi \bar{R} T^L}}\right) \sinh(\Delta S/\bar{R}), \tag{5-9}$$

where P^{sat} is the saturation pressure at T^L, V_∞^L is the specific volume of the saturated liquid, $\bar{R}$ is the individual gas constant, sinh denotes the hyperbolic sine function, and ΔS is the change in the entropy due to the phase change, which is given in its most general form as[24]:

$$\frac{\Delta S}{\bar{R}} = \left\{4\left(1-\frac{T^V}{T^L}\right) + \left(\frac{1}{T^V}-\frac{1}{T^L}\right)\sum_{i=1}^{3}\left(\frac{\Theta_i}{2}+\frac{\Theta_i}{\exp(\Theta_i/T^V)-1}\right) + \frac{V_\infty^L}{\bar{R}T^L}(P^L - P^{sat}) + \ln\left[\left(\frac{T^V}{T^L}\right)^4 \frac{P^{sat}}{P^V}\right] + \ln\left[\frac{q_{vib}(T^V)}{q_{vib}(T^L)}\right]\right\}, \tag{5-10}$$

where Θ_i is the *i*th vibrational frequency of the water molecules and q_{vib} denotes the vibrational partition function and is given by:[24]

$$q_{vib}(T) = \prod_{i=1}^{3} \frac{\exp(-\hbar\Theta_i/2k_BT)}{1-\exp(-\hbar\Theta_i/k_BT)}, \tag{5-11}$$

where k_B and $\hbar$ are the Boltzmann and the reduced Planck constants respectively.

The momentum balance at the liquid–vapor interface can be described by:

$$(\boldsymbol{\tau}_L' - \boldsymbol{\tau}_V') \cdot \boldsymbol{n} = \sigma(\nabla_t \cdot \boldsymbol{n})\boldsymbol{n} - \nabla_t\sigma + m^{"}(\boldsymbol{u}^L - \boldsymbol{u}^V), \tag{5-12}$$

where $\boldsymbol{\tau}'$ is the total stress tensor, subscript t denotes the unit tangent vector at the interface, ∇_t is the surface gradient operator, $(\nabla_t \cdot \boldsymbol{n})$ is the curvature of the interface, and σ is the liquid surface tension which is assumed to be a linear function of temperature. Note that the force created by the disjoining pressure is neglected in eq (5-12).

The total stress tensors in liquid and vapor are defined as:

$$\boldsymbol{\tau}_L' = -P^L\boldsymbol{I} + \mu^L(\nabla\boldsymbol{u}^L + (\nabla\boldsymbol{u}^L)^{tr}), \tag{5-13}$$

and,

$$\boldsymbol{\tau}_V' = -P^V\boldsymbol{I} + \mu^V(\nabla\boldsymbol{u}^V + (\nabla\boldsymbol{u}^V)^{tr}) - \frac{2}{3}\mu^V(\nabla\cdot\boldsymbol{u}^V)\boldsymbol{I}. \tag{5-14}$$

The forces in eq (5-12) may be broken down into a normal component and two tangential components. The normal component relates the liquid and vapor pressures to the curvature of the interface while the tangential components describe the Marangoni stress along the interface.

To determine the temperature distribution at the interface, the energy balance is written as:

$$(k^V\nabla T^V - k^L\nabla T^L)\cdot\boldsymbol{n} - (\boldsymbol{n}\cdot\boldsymbol{\tau_l})\cdot\boldsymbol{u}^L + (\boldsymbol{n}\cdot\boldsymbol{\tau_v})\cdot\boldsymbol{u}^V = m^{"}h^{LV}, \tag{5-15}$$

where $\boldsymbol{\tau} = \boldsymbol{\tau}' + P\boldsymbol{I}$ is the viscous stress tensor and h^{LV} is the enthalpy of vaporization which is taken to be a linear function of temperature. In eq (5-15), the kinetic energy terms are assumed

negligible compared to the latent heat of evaporation term ($m^{"}h^{LV}$). In addition, the heat transfer by radiation, the heat generated by viscous dissipation, the work done by surface tension and disjoining pressure are neglected.

To complete the system of equations at the interface, we assume a no-slip condition ($\boldsymbol{u}^L = \boldsymbol{u}^V$), and a continuous temperature ($T^L = T^V$). Although the experimental thermocouple measurements showed that T^V is higher than T^L to a small degree, we will show later that ignoring the temperature discontinuities does not have a significant effect on the simulated evaporation fluxes.

5.3.2.3 Conditions at other boundaries

At the solid–liquid and solid–vapor boundaries, a no-slip condition was enforced, and since the walls were all not moving, the fluid velocities were zero. At these boundaries, the temperatures of both phases as well as the heat fluxes on each side were assumed to be equal.

For the liquid domain, an inlet stream from the bottom which was at a temperature equal to that of the temperature controller was assumed. In fact, this flow did not exist in the real experiments and was only considered to carry out the numerical simulation. This assumption should be viewed as a preparatory step to circumvent the difficulties associated with the challenging problem of modeling the contact line motion. To keep the interface at a fixed position and perform the simulation at steady-state conditions, the rate of the mass entering the liquid domain should be defined in such a way that it compensates for the mass lost at the interface, thus:

$$\dot{m}_{in} = \iint m^{"}(x, y, z) dA_I, \tag{5-16}$$

where $\dot{m}_{in}$ is the inlet mass flow rate and A_I is the area of the interface.

At the vapor outlet, the normal stress is specified as:

$$\boldsymbol{\tau}_V' \cdot \boldsymbol{n} = -P^0 \boldsymbol{n}, \tag{5-17}$$

where P^0 is the pressure measured by the pressure transducer. At the vapor outlet, it is also assumed that the temperature does not vary across the boundary ($\nabla T^V \cdot \boldsymbol{n} = 0$). This boundary condition could be verified by observing an insignificant change in the measured temperatures of

the vapor far from the interface. The outside walls of the vacuum chamber were assumed to be at the ambient temperature since the temperature of the vapor in the vacuum chamber measured far from the interface was found to be very close to the room temperature.

5.3.3 Numerical Analysis

The set of coupled nonlinear partial differential equations along with the boundary conditions given in section 5.3 was implemented in a commercial multiphysics simulation package (COMSOL Multiphysics version 5.2a, COMSOL Inc.[46]), and solved numerically. The thermophysical properties of the fluids and the solids used in the simulations are listed in Table 5-1. Only half of the domain (as shown in Figure 5-2) was studied numerically due to the symmetry in the geometry. The liquid, vapor, and solid domains were discretized into second order tetrahedral elements with a nonuniform element size distribution, being the finest at the interface and getting coarser with distance from the interface (see Appendix E). To approximate the velocities and pressure in the Navier–Stokes equations, P2+P1 elements were chosen in the software. To ensure that the solutions were independent of the mesh size, an extensive mesh dependence analysis was carried out for each run (see Appendix E). Once the relative changes in the total evaporation flux and the minimum temperature at the interface both were less than 0.1%, the refinement would stop. The maximum number of elements that satisfied the above-mentioned criteria was 865,760.

Table 5-1 Physical properties of the fluids and solids used in the simulation.

	Parameter			Unit	Ref.
Liquid	$\mu^L = 27.1\exp(-0.0352\,T)$			Pa s	47
	$\rho^L = \dfrac{(999.84 + 16.945T - 7.99\times10^{-3}T^2 - 46.17\times10^{-6}T^3 + 105.56\times10^{-9}T^4 - 280}{1 + 16.88\times10^{-3}T}$			kg/m³	48
	$\sigma = 10^{-3}(114.81 - 0.1435T)$			N/m	49
	$k^L = (T/228 - 1)^{0.18}$			W/(m K)	50
	$P^{sat} = 611.2\exp\left(1045.85115 - \dfrac{21394.66626}{T} + 1.0969T - 1.300374\times10^{-3}T^2 + 7.747299\times10^{-7}T^3 - 2.1649\times10^{-12}T^4 - 211.3896\ln T\right)$			Pa	51
	$C_p^L = 2.98806\times10^7 - 548720\,T + 4031.78\,T^2 - 14.8134\,T^3 + 2.7215\times10^{-2}\,T^4 - 2\times10^{-5}\,T^5$			J/(kg K)	52
Vapor	$\mu^V = \left(10^{-4}\sqrt{T/647.096}\right)\left(1.67752 + \dfrac{1426.601}{T} + \dfrac{2.6659\times10^5}{T^2} - \dfrac{6.5465\times10^7}{T^3}\right)^{-1}$			Pa s	53
	$C_p^V = (1875.711 - 3.465\times10^{-1}T - 5.919\times10^{-4}T^2 + 7.240\times10^{-6}T^3)$			J/(kg K)	53
	$k^V = 0.0088 - 10^{-5}T + 1.4\times10^{-7}T^2$			W/(m K)	53
	$h^{LV} = T(1/\rho^V - 1/\rho^L)\times(dP^{sat}/dT)$			J/kg	51
	$\rho^V = P^V/\bar{R}T^V$			kg/m³	
Solids	Copper	Aluminum	Quartz		
	$k^C = 386$	$k^A = 230$	$k^Q = 3$	W/(m K)	54
	$\rho^C = 8930$	$\rho^A = 2700$	$\rho^Q = 2650$	kg/m³	
	$C_p^C = 385$	$C_p^A = 900$	$C_p^Q = 743$	J/(kg K)	

5.4 Results and Discussion

In this section, a comparison between the experimental and numerical results is presented. Specifically, some aspects of the evaporation phenomenon that are difficult or almost impossible to understand solely by analyzing the experimental data are explained with the aid of numerical simulation.

5.4.1 Velocity field in the liquid

The three-component three-dimensional (3C3D) velocity field below the evaporating meniscus at 190 Pa, 300 Pa, and 475 Pa obtained from PIV experiments and numerical simulation are presented in this section. To describe the flow structure below the meniscus, the experimental

velocity arrows obtained from processing the data of scanning PIV performed at 190 Pa are shown in Figure 5-3. Note that only half of the volume was studied in the PIV experiments due to the limitation in the depth of focus of the lenses. In Figure 5-3, a large toroidal vortex ring can be seen below the meniscus which occupies the whole cuvette width. This torus shaped motion of the liquid is deformed in the wider direction (x) as a result of the rectangular cross section of the cuvette. As shown by the arrows, the liquid moves upward in the central region and reaches the interface which leads to a sudden decrease in the liquid velocity (point A). As the flow interacts with the interface, it moves toward the contact lines where the three phases meet (BC, CD, and BE). Note that the arrows on the top do not represent the velocities at the interface, but are the velocities at a small distance below the interface. This is because a small region below the interface was masked during the image processing and was not studied experimentally due to the high reflection of light emitted from accumulated particles at the interface. The velocity field in this region, however, has been predicted by the numerical simulation and will be described later.

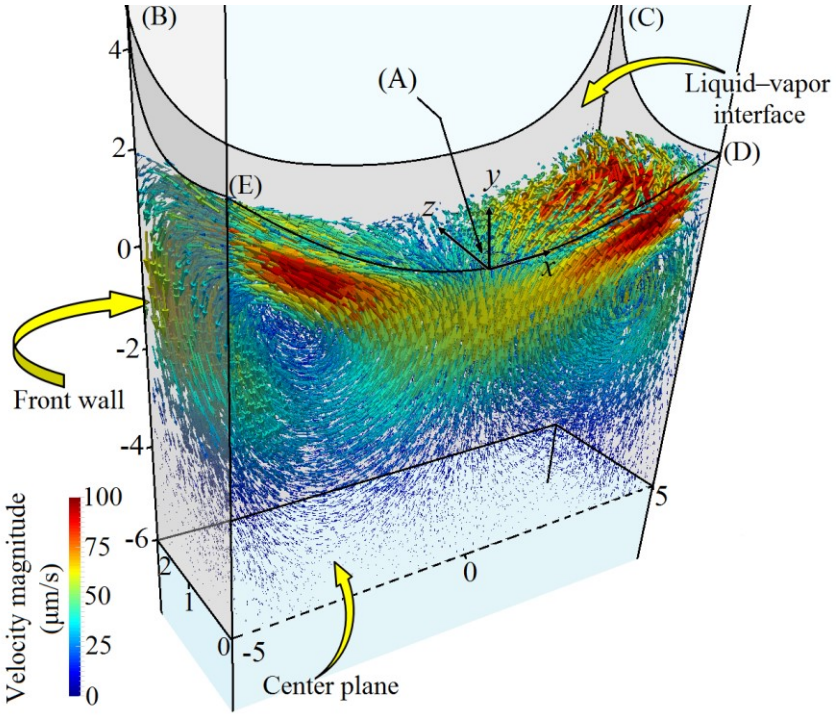

Figure 5-3 3C3D experimental velocity vectors below the evaporating meniscus for a typical pressure of 190 Pa. The arrow size and color scale to the local velocity magnitude. Only every 150th arrow from 1,650,000 available data points is illustrated to avoid cluttering the image. The dimensions are shown in millimeters. The front wall is named according to the position of the camera.

Figure 5-4 shows a comparison between the 3C3D velocity magnitudes obtained from scanning PIV and those predicted by the simulation at the same pressures. Two types of velocity boundary conditions at the interface were considered in the simulation. First, the liquid was allowed to slip freely according to the force balance given by eq (5-12). Second, the tangential velocity of the liquid at the interface was set to zero. As the results in Figure 5-4 show, when the free-slip boundary condition was applied, poor agreement between the experimental and simulated velocity magnitudes were observed. Also, the maximum velocities in the simulation using eq (5-12) occurred at the interface and were almost twice as large as the experimentally measured velocities. However, when a zero tangential velocity at the interface was applied to the model, the simulated velocities, including the magnitude and the position of the maximum velocities, matched the experimental data well. We had noticed the same behavior in our previous study[37] during a two-dimensional velocity measurement in a liquid evaporating from a cylindrical cuvette. In that

study, we show that this observation was neither due to the poor resolution of the images of particles below the interface nor the high reflection of light emitted from accumulated particles at the interface. From a theoretical point of view, there is no reason that the interfacial flows in a pure liquid would be suppressed at the interface while it is exposed to a shear force from below. The vapor flow also could not have suppressed the liquid flow as they both flow in the same tangential direction; as well the viscosity and the density of the vapor are much smaller than those of the liquid. Therefore, it can be said that the interfacial flows were almost suppressed due to using the PIV suspension instead of using pure water in evaporation experiments. Not only were the interfacial flows affected, but also the flow field far from the interface was influenced. In ref. 37, individual particles trapped at the interface were tracked at a high magnification, confirming they were stationary. The stagnation of particles at the interface of an evaporating droplet during PIV experiments was also reported by Kang *et al*.[55]. The alteration of the interfacial conditions in a liquid–gas system in the presence of surfactant molecules[55,56] and colloidal particles[57,58] (both of which are present in the PIV suspension used in our experiments) has been discussed extensively, and will not be further explored here.

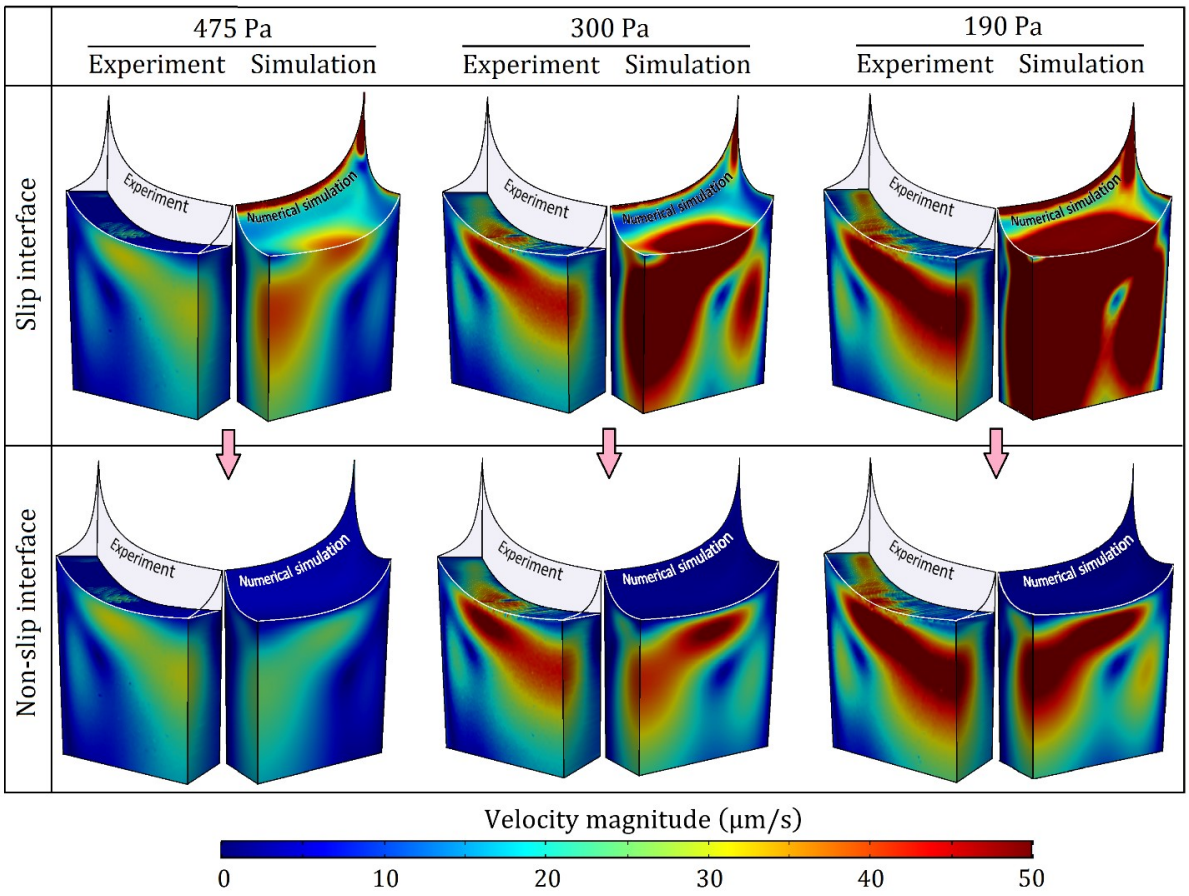

Figure 5-4 Comparison of the simulated and experimental velocity magnitudes in liquid at three pressures. The top panel compares the experimental and simulated velocities assuming in the model that the liquid slipped freely along the interface (eq (5-12)). The bottom panel compares the experimental and simulated velocities assuming in the model that the liquid did not slip along the interface. Only one quarter of the liquid is shown.

For practical applications, it is worth identifying the mechanism involved in generating the vortical flow seen in Figure 5-4. Obviously, the observed vortical flow in the experiments is not induced by surface tension forces since the maximum velocities in the experiments did not occur at the interface. Therefore, two possibilities may explain the underlying cause for inducing such a flow. The first hypothesis is that the flow is caused by the evaporation mass loss at the interface, which is believed to take place at its maximum near the contact lines and the corners, meaning liquid needs to be supplied to the corners to evaporate. The second possibility is that the vortex is generated by buoyancy forces in the liquid. This hypothesis is made based on the fact that by

decreasing the pressure, the temperature at the interface decreases due to the evaporative cooling effects, and since the temperature at the bottom of the cuvette is maintained at a constant value, the variation of the density in the liquid becomes stronger which in turn can intensify the vortical flow. Here, we encounter a case in which the experimental data cannot direct us to draw a conclusion. To overcome this limitation, we took advantage of the numerical simulation by isolating these two effects. To accomplish this, the simulations were repeated once neglecting the buoyancy forces ($\boldsymbol{g} = 0$), and once neglecting the evaporation mass loss at the interface ($m'' = 0$) but keeping the evaporative cooling effects ($m'' h^{LV} \neq 0$). The results showed that when the buoyancy effects were neglected, the vortical flow pattern in the simulation vanished completely and the flow became unidirectional toward the interface with a magnitude much smaller than the experimental velocities ($\sim 3\ \mu m/s$). However, when the evaporation loss was neglected, no significant change was observed in the simulated velocities. Therefore, the large vortex in the liquid is attributed to the buoyancy effects. In fact, as the evaporation took place, the liquid near the vertical walls became warmer and heavier (recall that at $T < 4$ °C, water becomes denser as it gets warmer) which drives the liquid in the peripheral region downward and the liquid at the central region upward according to the continuity of the liquid. An important conclusion that can be drawn from this observation is that in the experiments with water in 3D confined geometries (not infinite 1D liquid films), buoyancy driven convection may still occur although the liquid is thermally stabilized. That is, keeping the heaviest liquid at the bottom and the lightest liquid at the top during the evaporation experiments with water by setting the bottom temperature, does not ensure that buoyancy driven convection is eliminated, as it did not in our study. The dimensionless Rayleigh number (*Ra*) and Bond number (*Bo*) in the liquid for different experiments are listed in Table 5-2.

5.4.2 Interfacial flows in pure liquid

So far, we have shown that the velocities below the interface obtained from PIV using a suspension of particles could not be generalized to those that would occur in pure water in the absence of particles. However, the PIV results were valuable to partially verify the validity of the mathematical model and the numerical solutions. The certainty of the model in predicting other parameters such as temperatures and evaporation fluxes will be discussed later. In this section, the model is used to predict the flow field near the interface of pure water while it evaporates. This

could not be achieved through the PIV experiments as was discussed in Sec. 5.4.1. We should mention that Ward and Duan[33] could measure the velocities at the interface of an evaporating water droplet by partially immersing the tip of a deformable cantilevered probe into the liquid and measuring the deflection of the probe. However, their approach has some limitations regardless of the disturbance that the probe may cause in the interfacial flows. Firstly, to find the velocity distribution at a 3D interface such as that in our study, too many measuring points are required as each measurement gives only the velocity of a certain point (Ward and Duan only performed the measurement at one point at the interface). Secondly, it cannot measure the normal component of the velocity and only determines the component tangential to the interface. Thirdly, the obtained velocity depends on the depth of immersion of the probe and may not reflect the exact velocity at the interface. Fourthly, their method is not applicable in measuring the interfacial velocities in narrow regions where the liquid forms a thin film, the thickness of which is comparable to the thickness of the probe; such narrow regions occurred in the present study.

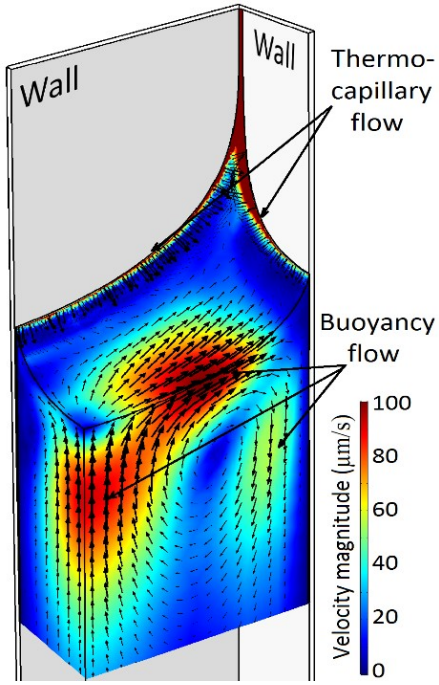

Figure 5-5 Simulated velocity magnitude and direction at 300 Pa. Only one quarter of the liquid close to the interface is shown to display the details in the center. Buoyancy forces induce the large vortex that flows outward. Thermocapillary forces produce the small flow near the contact lines which flows inward.

The simulated velocities at the interface for a pressure of 300 Pa are shown in Figure 5-5. For other pressures, the patterns were the same and are not illustrated here. As can be seen in Figure 5-5, the flow on the majority of the interface is driven by the drag of the large vortex in the bulk liquid which was induced by the buoyancy forces. There can also be seen a narrow region near the contact lines in which the liquid moves away from the solid walls. This flow was induced by the thermocapillary forces since the walls were warmer than the liquid. The flow near the contact line would vanish in the simulation when the surface tension was assumed constant. As can be seen in Figure 5-5, the thermocapillary flow could not spread entirely over the interface and was suppressed by the large vortex rotating in the opposite direction. It is interesting to note that the maximum velocity produced by the buoyancy flow at 300 Pa was ~100 μm/s while the velocity of the thermocapillary flow in the opposite direction was ~1000 μm/s. Although having a velocity an order of magnitude larger, the thermocapillary flow was not strong enough to overcome the opposite interfacial flow produced by the massive buoyancy vortex. As the pressure decreased, although the thermocapillary flows became stronger, so did the buoyancy flows. This prevented the occurrence of a thermocapillary motion at the interface within the whole range of the pressures studied here (150–900 Pa). Therefore, a low-velocity buoyancy flow that was prevalent in a large volume of the liquid below the interface, was capable of obstructing the development of a thermocapillary flow at the interface, most likely due to having a much larger moment of inertia. The velocities of the mentioned buoyant flows at the interface may sometimes be too small to be detected experimentally. For instance, at 600 Pa, the maximum simulated velocity of the large buoyancy vortex at the interface that prevented a thermocapillary flow from spreading over the interface was only ~35 μm/s. Such a slow liquid flow generated by the buoyancy effects at the interface may not be detectable in the experiments by measurement devices such as a cantilevered probe, neither can it be detected indirectly by performing an energy balance at the interface. As a result, one may conclude that the thermocapillary flows in pure water do not exist even when the interface is quiescent. Therefore, the absence of the thermocapillary flows in water in some studies such as[35] in which it was expected to occur as the Marangoni number was as large as 27,000, may also be explained by a reason other than the effect of surfactants and contaminants.[37,59,60] That is, the thermocapillary flows may be suppressed by an opposing buoyancy flow which may not sometimes be detected.

The thermocapillary flow at the interface has been observed for many liquids. However, for pure water, its existence has remained questionable. Some researchers have attributed it to the impurities accumulated at the interface during the experiments. However, this may not be the reason that differentiates water from the other liquids because first, the impurities can also exist in the experiments with other liquids and second, a thermocapillary flow in water, although the liquid contained solid particles, has been observed in a few studies such as the study of Xu and Luo.[61]

The answer might be sought in the anomaly of the density of water. Recall that the density of water is not a monotonic function of temperature as most liquids and reaches a maximum value at 4 °C. Accordingly, it is possible that a buoyancy flow in an opposite direction of the thermocapillary flow forms and suppresses the thermocapillary flow in some experiments. To be clearer, within the pressure range that we performed our study, the density of water, in contrast to other liquids, is proportional to the temperature. As a result, it becomes denser near the warmer walls and moves downward. However, if a liquid other than water were used, it would become lighter near the warm solid walls and result in an opposite rotation buoyancy flow vortex which would be in favor of the thermocapillary flow. This not only would remove the resistance against the thermocapillary flow but also would help it to develop faster. However, for water, the buoyancy vortex rotates in a reverse direction than it would do in case of using other liquids instead of water, and suppresses the thermocapillary flow. This is another possible answer to the question of why the thermocapillary flows in water are *sometimes* but not *always* absent. The thermal conductivity of the material used as the evaporation container is a key factor in determining whether the thermocapillary flow can overcome the counter rotating buoyancy flow or not. For instance, in the experiments in[35] in which the authors used a low thermal conductivity material ($k \approx 0.2\ W/(\mathrm{m\ K})$) the thermocapillary flow was absent even at Marangoni numbers as large as 27,000. However, the authors in[33,40] who used the same experimental setup and same geometry as in[35] with the only difference that they used a higher thermal conductivity material ($k \approx 14\ W/(\mathrm{m\ K})$), could detect a thermocapillary flow at the surface of water. We will show later from the numerical simulation that by increasing the thermal conductivity of the cuvette in our study, the strength of the thermocapillary flow increases until it can overcome the buoyancy flow and spreads entirely over the interface. We should highlight that some other factors such as the size and shape of the

interface as well as the dimensions of the container are also important as they determine the direction of the buoyancy flow. However, they will not be studied here.

5.4.3 Temperatures in the liquid and vapor

A comparison between the experimental and simulated temperature profiles in the liquid and vapor along the centerline is shown in Figure 5-6. As was expected, in both experiments and simulations, the minimum temperatures in the liquid and vapor were achieved at the interface due to the evaporative cooling effects. The measured interfacial temperatures are very close to the saturation temperatures corresponding to the pressure in the vapor. This implies that the evaporation rate was relatively slow which may be influenced by the limitation of heat transfer to the interface.

Table 5-2 Comparison between the experimental and simulated temperature jumps.

		Exp. Temp.		Sim. Temp.		Sat. Temp. at P^V	Exp. Temp. jump	Ra§	Bo§
	P^V(Pa)	T^L(°C)	T^V(°C)	T^L(°C)	T^V(°C)	T^L_{sat}(°C)	$[T^V - T^L]$ (°C)	$\frac{g\beta\Delta T}{L^3/\nu\alpha}$	$\frac{\Delta\rho g}{D^2/\sigma}$
1	540.4 ± 2.7	-1.64 ± 0.05	-1.41 ± 0.05	-1.68	-1.68	-1.67	0.23	604547	15.6
2	409.7 ± 2.2	-5.35 ± 0.05	-5.01 ± 0.05	-5.39	-5.39	-5.38	0.34	1634025	15.5
3	361.4 ± 1.8	-6.98 ± 0.05	-6.61 ± 0.05	-7.05	-7.05	-7.02	0.37	2236190	15.5
4	283.8 ± 1.4	-10.1 ± 0.05	-9.55 ± 0.05	-10.08	-10.08	-10.12	0.55	3634997	15.4
5	190.2 ± 1.0	N/A	-14.08 ± 0.05	-14.94	-14.94	-15.07	N/A	N/A	N/A

§ In calculation of Ra and Bo numbers, g is the gravitational acceleration (9.81 m/s^2), β is the coefficient of thermal expansion, ΔT is the difference between the temperature of the liquid at the bottom and that at the interface in the center, L is the height of the liquid at the center, ν is the kinematic viscosity, α is the thermal diffusivity, $\Delta\rho$ is the difference between the density of the liquid and the density of the vapor at the interface in the center, D is the tube diameter, and σ is the surface tension at the center of the meniscus. The physical properties used in calculation of Ra are the average between the bottom and the interface. For calculation of Bo, the properties at the interface are used.

In the liquid phase, excellent agreement between the interfacial temperatures listed in Table 5-2 predicted by the model and those measured by the thermocouple was observed. However, in the vapor phase, there was a small discontinuity (jump) in the experimental temperatures at the interface, while it was not accounted for in the simulation. In fact, the interfacial temperature of the vapor measured by the thermocouple was always a fraction of a degree higher than that of the liquid at the interface, which is consistent with previous studies. Accordingly, the simulation underpredicted the interfacial temperatures of the vapor since, in the model, a continues

temperature ($T_L = T_V$) was assumed at the interface. The maximum discontinuity measured by the thermocouple was 0.55 °C which occurred at the lowest pressure at which measurements were possible (Experiment 4). The temperatures of the liquid at 190 Pa could not be measured because as soon as the thermocouple was submerged into the liquid, the liquid would freeze and interrupt the experiment.

The existence of a temperature discontinuity at the interface of evaporating water has been investigated and discussed extensively by Ward and coworkers[26,34,39,40,62] and Badam *et al.*[28,29]. Good reviews on the topic may be found in references.[30,31] We should mention that the magnitudes of the temperature discontinuities found in the present study were an order of magnitude smaller than those reported by Ward and coworkers. As was explained in,[27,28] the temperature jump is directly proportional to the evaporation flux and vapor heat flux. Therefore, the difference between the magnitude of the jumps found in this study and those reported previously can be partly attributed to the higher evaporation rates that they achieved in their experiments by using a higher thermal conductivity material. This can be mainly due to a higher heat flux from the vapor to the interface as they used a convex interface that could produce a higher vapor heat flux compared to a flat[27] and a concave[37] interface.

To investigate the potential influence of the assumption of a continuous temperature at the interface ($T^L = T^V$) on the simulation results, the simulations were repeated by imposing the experimental jumps at the interface (*i.e.*, $T^V = T^L + \Delta T^{\exp}$, where $\Delta T^{\exp}$ is the measured temperature jump). By using a jump boundary condition, it was found that the evaporation flux increased at most by 1.2%. Moreover, the temperatures and the velocities in the liquid almost did not change. However, the temperature profiles in the vapor experienced a minor change only within 10 mm above the interface, which is demonstrated by the dashed curves in Figure 5-6. It is worth mentioning that the effect of temperature jumps may not always be negligible. For larger temperature jumps, the role of molecular phonons in eq (5-10) becomes more significant[63] and the assumption of a continuous temperature at the interface may not be valid anymore.

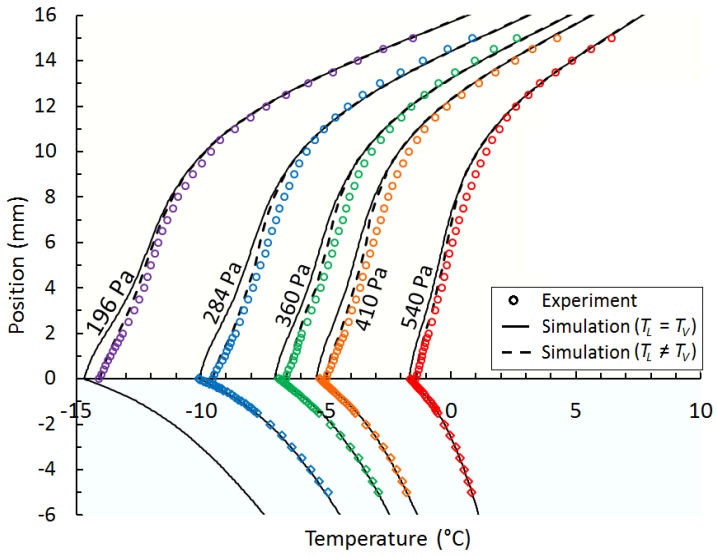

Figure 5-6 Experimental and simulated temperature profiles in the liquid and vapor along the centerline at five pressures. The position zero denotes the interface. The temperature profile in the liquid at 196 Pa was not measured to avoid freezing of the liquid.

5.4.4 Liquid temperatures along the interface

The developed model predicts that a thermocapillary convection does not exist over the majority of the interface and is only limited to a small portion of the interface in the vicinity of the contact lines. To explore this experimentally, the temperature distribution over the entire interface could be measured by the thermocouple. However, this is very difficult as the 3D interface would require many data points. Instead, the temperatures at four points along the interface between the center and one of the corners were measured at 4 points indicated in Figure 5-7a, and the results were compared to the simulated temperatures at the interface shown in Figure 5-7b. As illustrated in Figure 5-7b, the temperatures T_A, T_B, and T_C were almost equal after considering the uncertainty in the measurements. However, the temperature T_D which was measured near the solid walls is higher than the others, which is consistent with the simulated temperature distribution. From a theoretical point of view, a thermocapillary convection must exist if there is a temperature variation along the interface.[64] Therefore, by analyzing the experimental temperatures and considering the uncertainty of the measurements, it can be said that a thermocapillary convection between points C and D should essentially exist while between points A and C may be absent. However, since no

data was collected between points C and D, it could not be determined how far the thermocapillary flow could develop over the interface.

The simulated temperature profile along the diagonal curve is also shown in Figure 5-7b. As shown, the simulated liquid temperature in the diagonal direction was almost uniform and increased sharply near the corner. Note that the temperature of the liquid exactly at the solid walls could not be measured due to the limitation caused by the finite thickness of the thermocouple junction and also the necessity that the thermocouple should not touch the walls in the measurements to avoid heat exchange with the warm walls. As can be seen in Figure 5-7a, the simulated temperature is almost uniform over most of the area of the interface, which appears as a dark red color, and increases sharply near the contact lines. According to the simulated temperatures, the maximum temperature at the interface occurred at the tips of the thin films although the evaporative cooling effects were strongest in those regions, as will be shown in Sec. 5.4.5.

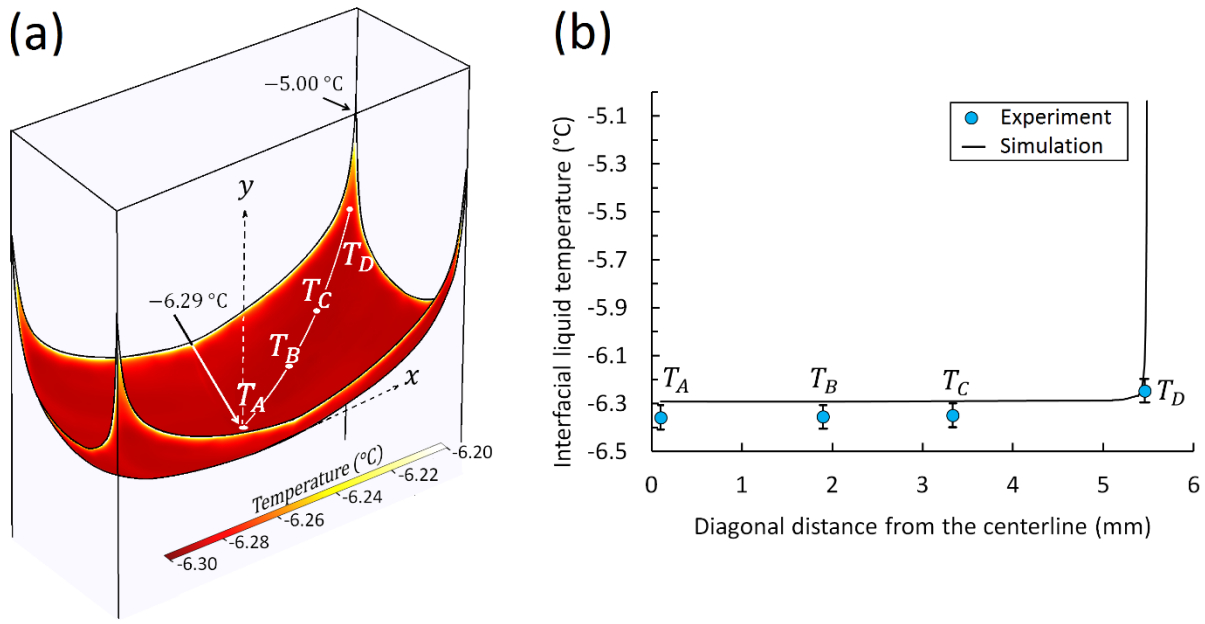

Figure 5-7 Interfacial temperatures in the liquid during evaporation at 382 Pa. (a) The distribution of the liquid temperature at the interface obtained from the numerical simulation and indication of the location of points ABCD (b) The experimentally measured temperatures at A, B, C, and D and comparison with the simulated temperatures along the curve ABCD.

5.4.5 Evaporation flux

The variation of the evaporation flux with pressure was studied experimentally and numerically. As is shown in Figure 5-8 by closed diamond data points, the experimentally measured evaporation flux of pure liquid increased with decreasing pressure. The evaporation fluxes below 216 Pa could not be measured as the liquid froze with a further decrease in the pressure. Also shown with red circles are the results of evaporation flux of pure water in a similar cuvette and the same experimental setup, which were extracted from ref. 36. The evaporation flux of the liquid when it contained solid particles was also measured to understand the possible effect of particles on the evaporation rates. As the open diamonds in Figure 5-8 show, the evaporation flux in the presence of particles is slightly lower than that of the pure liquid.

To investigate the significance of the interfacial flows on the evaporation rates, we performed the simulation with and without considering the liquid flow at the interface and compared the calculated fluxes. Based on this, we found that although by imposing a zero tangential velocity at the interface the evaporation flux decreased, this change was much less than enough to explain the difference between the experimental evaporation fluxes of suspension and pure water. Therefore, other mechanisms probably have reduced the evaporation rate of the suspension. The reduction of the interfacial area by accumulated particles at the interface could be another reason. However, it is difficult to explore numerically as one would need to include the solid particles in the model. It is worth noting that the addition of particles does not always have an adverse impact on evaporation rates. For instance, Zhang *et al*.[65] reported that the evaporation rates in suspensions that contained 3% and 6% TiO_2 nanoparticles were lower than that of pure water by 36% and 10% respectively. However, the evaporation rate in the 8% suspension of the same particles was 60% higher than that in the pure water. Therefore, the effect of particles on the evaporation rates is a complex phenomenon which depends on several parameters such as the chemistry, concentration, size, and structure of the particles trapped at the interface, as stated by the authors in.[65]

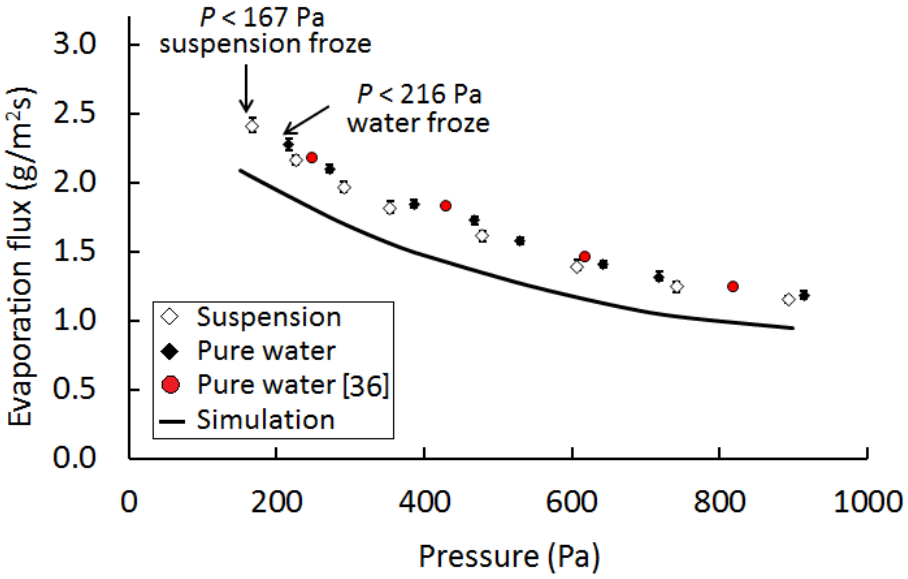

Figure 5-8 Experimental and simulated evaporation fluxes as a function of pressure in the vacuum chamber. The black and open diamonds were measured in this study. Each data point shows the average of three measurements. The error bars show the maximum and minimum values and are covered by the data points. The red circles show the measured fluxes in a similar cuvette which are extracted from ref. 36. The solid curve indicates the results of the simulation.

In Figure 5-8, the solid curve shows the model prediction of the evaporation flux at different pressures. While the dependence of the simulated evaporation flux on the pressure is in good agreement with the observed trend in the experimental data, the model always underpredicted the values of experimental evaporation fluxes. The maximum deviation of the simulated fluxes from the experimental data was found to be 19%. To understand where the deviation stems from, we should first determine by which factor the evaporation flux was controlled, *i*) heat transfer to the interface (eq (3-15)), or *ii*) molecular transport across the interface (eq (5-9)). To understand the contribution of the latter on evaporation, the SRT expression given by eq (5-9) was purposely multiplied by a factor of 2 and the simulations were repeated for several pressures within the range of 160–950 Pa. As a result of this manipulation, no change was observed in the simulated evaporation fluxes. Therefore, within the studied pressure range, the evaporation process was completely limited and controlled by heat transfer to the interface, and the mass flux was determined by the rate of energy balance to the interface rather than the mass transfer across the interface. Therefore, it is possible that the uncertainties in evaluating the liquid, vapor, and cuvette

thermo-physical properties, as well as the latent heat of evaporation used in the simulation, gave rise to the observed 19% discrepancy. For instance, a 5% increase in the cuvette thermal conductivity or saturation pressure of water, increases the simulated evaporation flux by 3.6% and 18.4%, respectively.

To make sure that the discrepancies between the measured and simulated evaporation fluxes have not come from the poor treatment of the liquid fingers at the corners where the rate of evaporation is believed to reach its maximum,[21,34] we performed the following analysis. As discussed earlier, the experimental evaporation fluxes were obtained by tracking the position of the interface with time. A plot of position with time for a typical experiment at 380 Pa is shown in Figure 5-9a. As can be seen, the data of *H vs*. *t* has a perfectly linear relationship ($R^2 = 0.999918$) which indicates that the evaporation flux essentially remained almost constant in the course of 2400 s of the measurement. During this period of time, the interface moved down by 7.3 mm which corresponded to a 7.3 mm stretch of the liquid films that were pinned to the cuvette's top edge, as shown in Figure 5-9b. Therefore, given that the measured evaporation fluxes did not change as the liquid films elongated, it can be inferred that the evaporation from the thin liquid films in this study did not contribute significantly to the total evaporation flux. This could also be verified from the numerical simulation. In the simulation, the evaporation fluxes were calculated for interfaces with various lengths of liquid films as shown in Figure 5-9c. The films were assumed to have an isosceles right triangular cross section with a reasonable side length of 50 μm. For the pressure of 380 Pa, it was found that as the tip of the liquid film moved from 0 to 4.2 mm, the total evaporation rate increased by only 1.4%, which shows the negligible contribution of the thin films in determining the total evaporation from the meniscus. However, we should note that this does not mean the evaporation flux from the thin films was small. In fact, the evaporation fluxes in this region were found to be an order of magnitude higher than that in the central region. However, their contribution to the total evaporation rate was still negligible due to the small surface area of the thin films compared to the total area of the interface.[66]

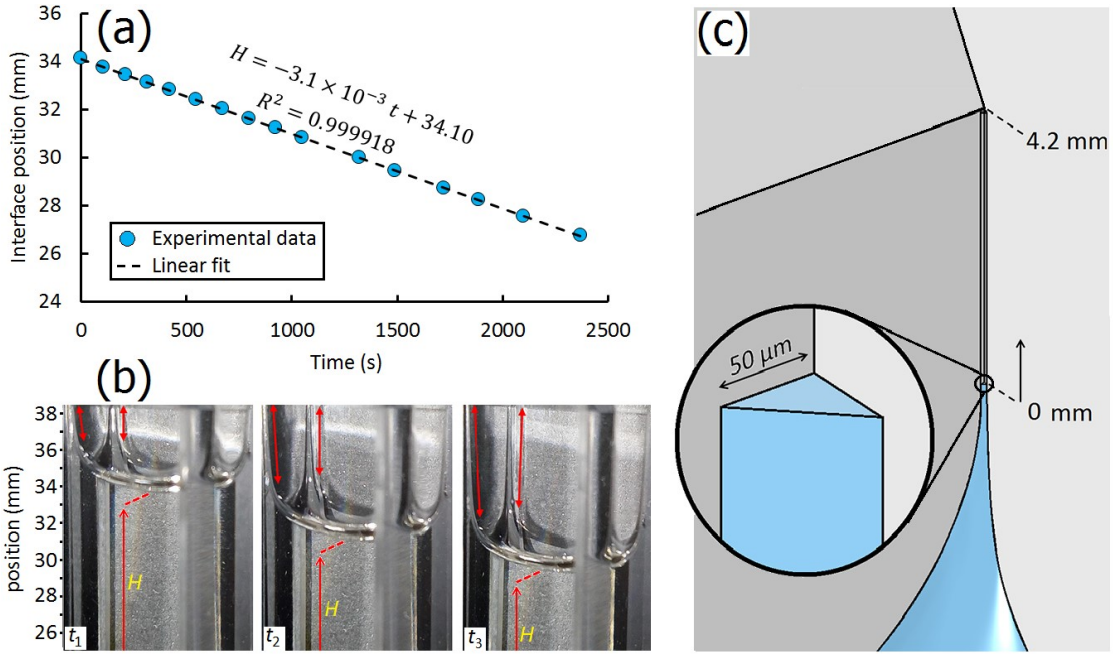

Figure 5-9 The position of the interface *vs.* time for a typical experiment at 380 Pa. (b) The three images show the recession of the interface and the subsequent stretch of the liquid films. The parameter H shows the distance from the center of the interface to the bottom of the cuvette. (c) A 50 μm thin film with a constant cross section but a variable length of up to 4.2 mm was considered in the simulation to study the contribution of the thin films to the total evaporation rate.

5.4.6 Interfacial transport limit *vs.* heat transfer limit

In Sec. 5.4.5, we showed that the evaporation in our study was controlled by heat transfer to the interface. We also showed in Sec. 5.4.2 that a thermocapillary flow at the interface, which is known to be the main mechanism of energy transfer to the interface during evaporation,[33] was suppressed by a stronger buoyancy flow. Therefore, it can be said that if the thermocapillary flow becomes strong enough to overcome the buoyancy flow at the interface, then the evaporation rates should increase significantly. To strengthen the thermocapillary flow in the simulation, we changed the thermal conductivity of the cuvette (k) in the range of $0.01 - 10{,}000$ W/(m K) and calculated the total evaporation fluxes from the numerical simulation. Figure 5-10 shows that the simulated evaporation flux increased by increasing the thermal conductivity of the cuvette, as was expected. According to Figure 5-10, for small values of k, heat transfer completely controls the evaporation rates. As k increases, the contribution of the heat transfer becomes less pronounced as

the thermocapillary flow gets stronger. A significant enhancement of the evaporation flux can be observed at $k \approx 15\ \mathrm{W/(m\ K)}$. This corresponds to the point at which the thermocapillary flow has become fully propagated over the interface and overcomes the buoyancy flow at the interface. It is interesting to note that although the thermocapillary flow has developed thoroughly across the interface at $k \approx 15\ \mathrm{W/(m\ K)}$, the evaporation rate is still controlled by heat transfer. As k increases further, the contribution of heat transfer diminishes until the evaporation flux becomes almost independent of the heat transfer, which is highlighted with a blue region in the background. In this region, the interfacial resistances against the transfer of molecules across the interface determine the evaporation rate. The thermal conductivities of some common materials that can potentially be used in the experiments are also annotated on Figure 5-10. As the results of the simulation suggest, by using a high thermal conductivity material such as graphene, the evaporation would probably be independent of the heat transfer. This condition is desirable for thermodynamicists to experimentally explore the accuracy of the existing theoretical expressions of evaporation and condensation. This is because the evaporation flux is at its maximum value while the heat transfer limitation is minimal. In this condition, the evaporation is mostly controlled by the kinetic effects at the interface. Therefore, the conclusions are less prone to be affected by the errors associated with the measurements of the interfacial temperatures and pressures. This is the limit of evaporation in which assessment of the existing evaporation expressions such as SRT and KTG (kinetic theory of gases) in predicting some fundamental phenomena occurring at the interface such as temperature jumps and condensation coefficients can be best undertaken. If the experiments are performed in the limit of evaporation that is mainly governed by heat transfer, the conclusions about these concepts may not be accurate since the interfacial phenomena have not played a role in evaporation from the interface. This is perhaps the reason that the SRT expression for evaporation flux agrees with a wide range of temperature jumps,[30] or that the evaporation coefficients obtained from the experiments are highly scattered between zero and one.[22]

We should finally note that these plots are obtained for the specific geometry of the cuvette and concave interface used in this study. For other geometrical configurations of the evaporation container and interface, the transition from the heat-transfer-limited region to the interfacial-transport-limited region is expected to occur at different *k*. For instance, for smaller interfaces, the

transition to the blue region might occur at smaller k since the buoyancy flows are weaker, and the thermocapillary flows can develop more easily than they did in our study.

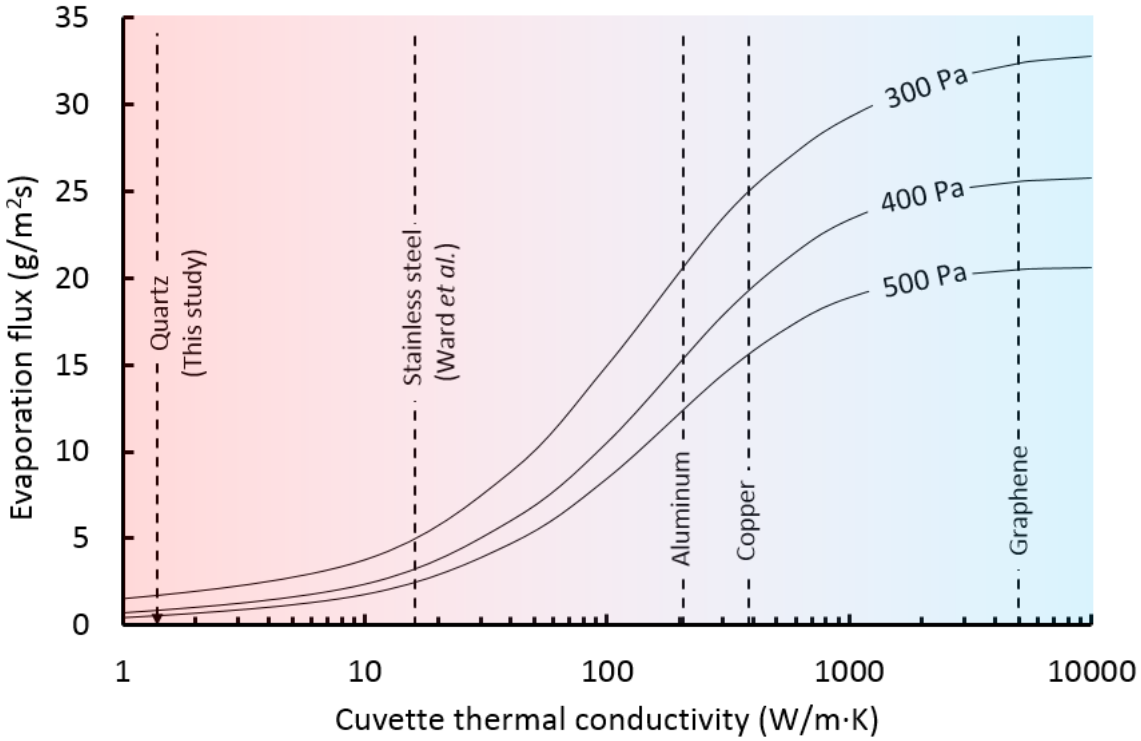

Figure 5-10 Simulated evaporation flux *vs.* thermal conductivity of the cuvette at three pressures. The red color in the background highlights the heat-transfer-limited region. The blue color in the background highlights the interfacial-transport-limited region. The horizontal axis has a logarithmic scale to depict the transition region more clearly.

5.5 Summary and Conclusions

The evaporation of water at low pressures from a meniscus formed in a rectangular geometry was studied both experimentally and numerically. A numerical model which took into account the transport of mass, momentum, and energy in the liquid, vapor, and at the interface, supplemented by appropriate boundary conditions, was developed. The model was validated by the experimental velocities obtained from 3D scanning PIV, experimental temperature fields across the interface and along the interface collected with a thermocouple, and evaporation fluxes measured at different pressures.

By comparing the experimental and simulated velocities, it was found that the particles used in the PIV experiments suppressed the interfacial flows during the evaporation experiments. Therefore, although PIV is widely accepted as a non-intrusive technique in measuring the velocities in fluids in general, special care should be taken when it is employed in measuring the interfacial flows close to a liquid–gas interface, as the velocities obtained by this technique may not reflect the actual velocities that would occur in a pure liquid.

By eliminating the effect of particles in the numerical simulation, the interfacial flows that could occur during evaporation of pure water were investigated. The results showed a large buoyancy vortex below the interface, which dragged the liquid from the center toward the solid walls, preventing the thermocapillary flows from developing at the interface. This is probably one of the reasons that a thermocapillary flow in water sometimes does not exist although the Marangoni numbers are far above the established critical one.

We also studied the evaporation fluxes from the interface and showed that the contribution of the thin liquid films formed in the corners to the total evaporation rate was negligible, although the evaporation flux was always maximum in the thin film regions because of the small area of the thin films compared to the total area of the interface.

Finally, by taking advantage of the numerical simulation, we investigated the effect of thermal conductivity of the cuvette on the evaporation fluxes and found that the evaporation phenomenon is mostly controlled by heat transfer for small thermal conductivity materials such as quartz and stainless steel. At very large thermal conductivities such as that of graphene, the evaporation is almost independent of the thermal effects and is mostly controlled by transport of molecules across the interface. The results also suggested that the occurrence of a thermocapillary flow at the interface as a result of increasing the thermal conductivity, although it increases the local evaporation flux significantly, is not enough to assume that the evaporation phenomenon has become independent of heat transfer.

5.6 References

(1) Faghri, A. Review and Advances in Heat Pipe Science and Technology. *J. Heat Transfer* **2012**, *134* (12), 123001.

(2) Lim, T.; Han, S.; Chung, J.; Chung, J. T.; Ko, S.; Grigoropoulos, C. P. Experimental Study on Spreading and Evaporation of Inkjet Printed Pico-Liter Droplet on a Heated Substrate. *Int. J. Heat Mass Transf.* **2009**, *52* (1–2), 431–441.

(3) Sau, T. K.; Murphy, C. J. Self-Assembly Patterns Formed upon Solvent Evaporation of Aqueous Cetyltrimethylammonium Bromide-Coated Gold Nanoparticles of Various Shapes. *Langmuir* **2005**, *21* (7), 2923–2929.

(4) Xue, G.; Xu, Y.; Ding, T.; Li, J.; Yin, J.; Fei, W.; Cao, Y.; Yu, J.; Yuan, L.; Gong, L.; et al. Water-Evaporation-Induced Electricity with Nanostructured Carbon Materials. *Nat. Nanotechnol.* **2017**, *12* (4), 317–321.

(5) Chen, X.; Goodnight, D.; Gao, Z.; Cavusoglu, A. H.; Sabharwal, N.; DeLay, M.; Driks, A.; Sahin, O. Scaling up Nanoscale Water-Driven Energy Conversion into Evaporation-Driven Engines and Generators. *Nat. Commun.* **2015**, *6* (June), 7346.

(6) Cazabat, A.-M.; Guéna, G. Evaporation of Macroscopic Sessile Droplets. *Soft Matter* **2010**, *6* (12), 2591.

(7) Hu, H.; Larson, R. G. Evaporation of a Sessile Droplet on a Substrate. *J. Phys. Chem. B* **2002**, *106* (6), 1334–1344.

(8) Sefiane, K.; Bennacer, R. An Expression for Droplet Evaporation Incorporating Thermal Effects. *J. Fluid Mech.* **2011**, *667*, 260–271.

(9) Hu, H.; Larson, R. G. Analysis of the Effects of Marangoni Stresses on the Microflow in an Evaporating Sessile Droplet. *Langmuir* **2005**, *21* (9), 3972–3980.

(10) Hu, H.; Larson, R. G. Analysis of the Microfluid Flow in an Evaporating Sessile Droplet. *Langmuir* **2005**, *21* (9), 3963–3971.

(11) Deegan, R. D.; Bakajin, O.; Dupont, T. F.; Huber, G.; Nagel, S. R.; Witten, T. A. Contact Line Deposits in an Evaporating Drop. *Phys. Rev. E* **2000**, *62* (1), 756–765.

(12) Deegan, R. D.; Bakajin, O.; Dupont, T. F.; Huber, G.; Nagel, S. R.; Witten, T. A. Capillary Flow as the Cause of Ring Stains from Dried Liquid Drops. *Nature* **1997**, *389* (6653), 827–829.

(13) AlWaaly, A. A. Y.; Paul, M. C.; Dobson, P. S. Effects of Thermocouple Electrical Insulation on the Measurement of Surface Temperature. *Appl. Therm. Eng.* **2015**, *89*, 421–431.

(14) Dunn, G. J.; Wilson, S. K.; Duffy, B. R.; David, S.; Sefiane, K. The Strong Influence of Substrate Conductivity on Droplet Evaporation. *J. Fluid Mech.* **2009**, *623* (2009), 329–351.

(15) Chandra, S.; di Marzo, M.; Qiao, Y. M.; Tartarini, P. Effect of Liquid-Solid Contact Angle on Droplet Evaporation. *Fire Saf. J.* **1996**, *27* (2), 141–158.

(16) Talbot, E. L.; Berson, A.; Brown, P. S.; Bain, C. D. Evaporation of Picoliter Droplets on Surfaces with a Range of Wettabilities and Thermal Conductivities. *Phys. Rev. E* **2012**, *85* (6), 61604.

(17) Sobac, B.; Brutin, D. Thermal Effects of the Substrate on Water Droplet Evaporation. *Phys. Rev. E* **2012**, *86* (2), 21602.

(18) Hu, D.; Wu, H.; Liu, Z. Effect of Liquid–vapor Interface Area on the Evaporation Rate of Small Sessile Droplets. *Int. J. Therm. Sci.* **2014**, *84*, 300–308.

(19) Fukatani, Y.; Orejon, D.; Kita, Y.; Takata, Y.; Kim, J.; Sefiane, K. Effect of Ambient Temperature and Relative Humidity on Interfacial Temperature during Early Stages of Drop Evaporation. *Phys. Rev. E* **2016**, *93* (4), 43103.

(20) Sáenz, P. J.; Wray, A. W.; Che, Z.; Matar, O. K.; Valluri, P.; Kim, J.; Sefiane, K. Dynamics and Universal Scaling Law in Geometrically-Controlled Sessile Drop Evaporation. *Nat. Commun.* **2017**, *8*, 14783.

(21) Vélez-Cordero, J. R.; Yáñez Soto, B.; Arauz-Lara, J. L. Transport of Colloids along Corners: Visualization of Evaporation-Induced Flows beyond the Axisymmetric Condition. *Langmuir* **2016**, *32* (32), 8171–8181.

(22) Marek, R.; Straub, J. Analysis of the Evaporation Coefficient and the Condensation Coefficient of Water. *Int. J. Heat Mass Transf.* **2001**, *44* (1), 39–53.

(23) Fang, G.; Ward, C. A. Examination of the Statistical Rate Theory Expression for Liquid Evaporation Rates. *Phys. Rev. E* **1999**, *59* (1), 441–453.

(24) Ward, C. A.; Fang, G. Expression for Predicting Liquid Evaporation Flux: Statistical Rate Theory Approach. *Phys. Rev. E* **1999**, *59* (1), 429–440.

(25) Persad, A. H.; Ward, C. A. Expressions for the Evaporation and Condensation Coefficients in the Hertz-Knudsen Relation. *Chem. Rev.* **2016**, *116* (14), 7727–7767.

(26) Fang, G.; Ward, C. A. Temperature Measured close to the Interface of an Evaporating Liquid. *Phys. Rev. E* **1999**, *59* (1), 417–428.

(27) Bond, M.; Struchtrup, H. Mean Evaporation and Condensation Coefficients Based on Energy Dependent Condensation Probability. *Phys. Rev. E* **2004**, *70* (6), 61605.

(28) Badam, V. K.; Kumar, V.; Durst, F.; Danov, K. Experimental and Theoretical Investigations on Interfacial Temperature Jumps during Evaporation. *Exp. Therm. Fluid Sci.* **2007**, *32* (1), 276–292.

(29) Badam, V. K. Experimental and Theoretical Investigation of the Evaporation of Fluids from Free Surfaces. PhD Thesis, University of Erlangen-Nuremberg (2007).

(30) Kazemi, M. A.; Nobes, D. S.; Elliott, J. A. W. Effect of the Thermocouple on Measuring the Temperature Discontinuity at a Liquid–Vapor Interface. *Langmuir* **2017**, *33* (28), 7169–7180.

(31) Persad, A. H.; Ward, C. A. Statistical Rate Theory Examination of Ethanol Evaporation. *J. Phys. Chem. B* **2010**, *114* (18), 6107–6116.

(32) Duan, F.; Badam, V. K.; Durst, F.; Ward, C. A. Thermocapillary Transport of Energy during Water Evaporation. *Phys. Rev. E* **2005**, *72* (5), 56303.

(33) Ward, C. A.; Duan, F. Turbulent Transition of Thermocapillary Flow Induced by Water Evaporation. *Phys. Rev. E* **2004**, *69* (5), 56308.

(34) Ghasemi, H.; Ward, C. A. Energy Transport by Thermocapillary Convection during Sessile-Water-Droplet Evaporation. *Phys. Rev. Lett.* **2010**, *105* (13), 136102.

(35) Thompson, I.; Duan, F.; Ward, C. A. Absence of Marangoni Convection at Marangoni Numbers above 27,000 during Water Evaporation. *Phys. Rev. E* **2009**, *80* (5), 56308.

(36) Song, X.; Nobes, D. S. Experimental Investigation of Evaporation-Induced Convection in Water Using Laser Based Measurement Techniques. *Exp. Therm. Fluid Sci.* **2011**, *35* (6), 910–919.

(37) Kazemi, M. A.; Nobes, D. S.; Elliott, J. A. W. Experimental and Numerical Study of the Evaporation of Water at Low Pressures. *Langmuir* **2017**, *33* (18), 4578–4591.

(38) Duan, F.; Ward, C. A. Surface-Thermal Capacity of D_2O from Measurements Made during Steady-State Evaporation. *Phys. Rev. E* **2005**, *72* (5), 56304.

(39) Duan, F.; Ward, C. A. Surface Excess Properties from Energy Transport Measurements during Water Evaporation. *Phys. Rev. E* **2005**, *72* (5), 56302.

(40) Ward, C. A.; Stanga, D. Interfacial Conditions during Evaporation or Condensation of Water. *Phys. Rev. E* **2001**, *64* (5), 51509.

(41) Kazemi, M. A.; Elliott, J. A. W.; Nobes, D. S. A 3D Flow Visualization in Evaporation of Water from a Meniscus at Low Pressures. In *The 10th Pacific Symposium on Flow Visualization and Image Processing, Naples, Italy, 15-18 June*; 2015.

(42) Kazemi, M. A.; Elliott, J. A. W.; Nobes, D. S. Determination of the Three Components of Velocity in an Evaporating Liquid from Scanning PIV. In *The 18th International Symposium on the Application of Laser and Imaging Techniques to Fluid Mechanics, July 4 – 7*; Lisbon Portugal, 2016.

(43) Song, X. Song, X., Experimental Investigation on Evaporation Induced Convection in Water

Using Laser Based Measurement Techniques. MSc. Thesis, University of Alberta (2010). 2010.

(44) Brücker, C. Digital-Particle-Image-Velocimetry (DPIV) in a Scanning Light-Sheet: 3D Starting Flow around a Short Cylinder. *Exp. Fluids* **1995**, *19* (4), 255–263.

(45) Kazemi, M.A., Experimental and Numerical Study on Evaporation of Water at Low Pressures, Ph.D. Thesis, University of Alberta (2017).

(46) *COMSOL Multiphysics® v. 5.2a,*; AB, Stockholm, Sweden, 2016.

(47) Kestin, J.; Sokolov, M.; Wakeham, W. A. Viscosity of Liquid Water in the Range −8 °C to 150 °C. *J. Phys. Chem. Ref. Data* **1978**, *7* (3), 941.

(48) Kell, G. S. Density, Thermal Expansivity, and Compressibility of Liquid Water from 0 °C to 150 °C. Correlations and Tables for Atmospheric Pressure and Saturation Reviewed and Expressed on 1968 Temperature Scale. *J. Chem. Eng. Data* **1975**, *20* (1), 97–105.

(49) Vinš, V.; Fransen, M.; Hykl, J.; Hrubý, J. Surface Tension of Supercooled Water Determined by Using a Counterpressure Capillary Rise Method. *J. Phys. Chem. B* **2015**, *119* (17), 5567–5575.

(50) Benchikh, O.; Fournier, D.; Boccara, A. C.; Teixeira, J. Photothermal Measurement of the Thermal Conductivity of Supercooled Water. *J. Phys.* **1985**, *46* (5), 727–731.

(51) Duan, F.; Thompson, I.; Ward, C. A. Statistical Rate Theory Determination of Water Properties below the Triple Point. *J. Phys. Chem. B* **2008**, *112* (29), 8605–8613.

(52) Archer, D. G.; Carter, R. W. Thermodynamic Properties of the NaCl + H_2O System. 4. Heat Capacities of H_2O and NaCl(aq) in Cold-Stable and Supercooled States. *J. Phys. Chem. B* **2000**, *104* (35), 8563–8584.

(53) Wagner, W.; Pruß, A. The IAPWS Formulation 1995 for the Thermodynamic Properties of Ordinary Water Substance for General and Scientific Use. *J. Phys. Chem. Ref. Data* **2002**, *31* (2), 387–535.

(54) Rohsenow, W. M.; Hartnett, J. P.; Cho, Y. I. *Handbook of Heat Transfer*; New York: McGraw-Hill, 1998; Vol. 3.

(55) Kang, K. H.; Lim, H. C.; Lee, H. W.; Lee, S. J. Evaporation-Induced Saline Rayleigh Convection inside a Colloidal Droplet. *Phys. Fluids* **2013**, *25* (4), 42001.

(56) Wu, T.-C.; Yang, Y.-M.; Maa, J.-R. Surfactant-Induced Retardation of the Thermocapillary Flow at a Gas/liquid Interface. *Int. Commun. Heat Mass Transf.* **2000**, *27* (5), 655–666.

(57) Kotula, A. P.; Anna, S. L. Probing Timescales for Colloidal Particle Adsorption Using Slug Bubbles in Rectangular Microchannels. *Soft Matter* **2012**, *8* (41), 10759.

(58) Hunter, T. N.; Pugh, R. J.; Franks, G. V.; Jameson, G. J. The Role of Particles in Stabilising Foams and Emulsions. *Adv. Colloid Interface Sci.* **2008**, *137* (2), 57–81.

(59) Hu, H.; Larson, R. G. Marangoni Effect Reverses Coffee-Ring Depositions. *J. Phys. Chem. B* **2006**, *110* (14), 7090–7094.

(60) Hu, H.; Larson, R. G. Analysis of the Effects of Marangoni Stresses on the Microflow in an Evaporating Sessile Droplet. *Langmuir* **2005**, *21* (9), 3972–3980.

(61) Xu, X.; Luo, J. Marangoni Flow in an Evaporating Water Droplet. *Appl. Phys. Lett.* **2007**, *91* (12).

(62) Popov, S.; Melling, A.; Durst, F.; Ward, C. A. Apparatus for Investigation of Evaporation at Free Liquid–vapour Interfaces. *Int. J. Heat Mass Transf.* **2005**, *48* (11), 2299–2309.

(63) Duan, F.; Ward, C. A.; Badam, V. K.; Durst, F. Role of Molecular Phonons and Interfacial-Temperature Discontinuities in Water Evaporation. *Phys. Rev. E* **2008**, *78* (4), 41130.

(64) Pearson, J. R. A. On Convection Cells Induced by Surface Tension. *J. Fluid Mech.* **1958**, *4* (5), 489–500.

(65) Zhang, W.; Shen, R.; Lu, K.; Ji, A.; Cao, Z. Nanoparticle Enhanced Evaporation of Liquids: A Case Study of Silicone Oil and Water. *AIP Adv.* **2012**, *2* (4), 42119.

(66) Wang, H.; Pan, Z.; Garimella, S. V. Numerical Investigation of Heat and Mass Transfer from an Evaporating Meniscus in a Heated Open Groove. *Int. J. Heat Mass Transf.* **2011**, *54* (13–14), 3015–3023.

Chapter 6: Final remarks and conclusions

Evaporation of water at reduced pressures in a vacuum chamber was studied both experimentally and numerically. The velocity distribution below the evaporating meniscus at different pressures was quantified using particle image velocimetry (PIV), and the temperature profiles in the liquid and vapor close to the interface at different pressures were measured using a fine thermocouple, to gain a better understanding of the mutual influence of the dynamics in the bulk fluids and the evaporation phenomena at the interface. A comprehensive mathematical model was developed and validated with available experimental data to help uncover new insights into the evaporation phenomenon which either could not be understood from experiments or could not be noticed and detected easily by analyzing the experimental results. The proposed model incorporated the transport of heat, mass, and momentum in the fluids as well as the conditions at the interface. The model was implemented in a commercial multiphysics simulation package and was solved numerically subject to appropriate boundary conditions for various pressures in the vapor.

Two geometries were selected as the liquid container for the evaporation studies: a cylindrical borosilicate tube and a rectangular quartz cuvette. The aim of using a cylindrical tube was to simplify the system from 3D to a 2D axisymmetric problem, which allowed us to account for the recession and deformation of the interface and solve the extra equations that they added to the system of equations. The aim of using a rectangular cuvette, regardless of the fact that it was more suitable for PIV experiments compared to the cylindrical tube that would distort the images of particles, was to understand more details about the evaporation phenomena that would be missing in the experiments with the cylindrical tube, such as evaporation from the thin liquid films formed in the corners. Also, the rectangular cuvette allowed us to develop a scanning PIV for quantification of the instantaneous 3D velocity field below the evaporating meniscus, which had not been performed in previous studies and was not achievable in the cylindrical tube. The scanning PIV yielded all three components (3C) of the velocity field in the volume (3D) using only a single camera. This was desirable in our low pressure evaporation experiments in which the full field of view from different viewing angles by multiple cameras was not possible. By performing the scanning PIV, the reliability of applying the continuity equation to obtain the out-

of-plane component of velocity (w) from the in-plane components (u and v) was examined. It was found that the w calculated from the continuity equation was in good agreement with the w obtained independently from a 3D data processing algorithm. The agreement improved remarkably when the in-plane components (u and v) were smoothed before being introduced into the continuity equation. Also, it was found that using a second order finite difference scheme to discretize the derivatives in the continuity equation did not make any improvement in calculating w compared to the first order scheme. The successful application of the continuity equation to calculate the out-of-plane component of the velocity (w) from the in-plane components (u and v) is promising since it delivers a higher resolution of w in the depth of the flow compared to the 3D cross-correlation algorithm (in our study, it yielded 4 times higher resolution). As a result, application of the continuity equation should be of interest for use in some applications other than evaporation driven flows in which the low resolution of the conventional 3D PIV techniques may cause some small scale phenomena occurring in the depth of the studied volume to be missed.

In addition to the velocity field, the temperature profiles in the liquid and vapor along the vertical centerline of the liquid containers as well as the variation of the liquid temperature along the interface were studied using a fine thermocouple. The former was performed in both containers to explore the temperature jumps existing at the interface, and the latter was carried out only in the rectangular cuvette to investigate the possibility of the occurrence a thermocapillary flow on the interface. Depending on the pressure of the vapor phase, the magnitude of the temperature jumps measured by the thermocouple at the interface fell in the range of 0.14–0.36 °C for evaporation from the cylindrical tube, and 0.23–0.55 °C for evaporation from the rectangular cuvette. The rectangular cuvette showed a larger temperature jump at the same experimental conditions compared to the cylindrical tube due to a higher evaporation flux. However, both showed significantly smaller temperature jumps compared to those previously reported at the same pressure. This was attributed to the concave interface that was surrounded by solid walls in this study, which created relatively small vapor phase heat fluxes to the interface and consequently small temperature jumps. An advantage of the temperature jump measurement in the current study compared to the previous studies was that the thermocouple in the vapor phase could approach closer to the liquid–vapor interface because of two reasons. First, the vertical position of the thermocouple was controlled using a stepper motor which could move the thermocouple with a

finer resolution (1.25 μm/step) than the currently used manual manipulators can do. Second, it was not required to keep a certain distance between the thermocouple edge and the interface since the interface receded smoothly in our unsteady-state experiments. The temperature jump measurements in the previous studies were performed at steady-state conditions in which the interface reportedly fluctuated within the range of ±10 μm as a result of continuous supplying of the evaporating liquid with a controllable syringe pump. This means that the thermocouple had to be kept at least 10 μm away from the interface when it measured the interfacial temperatures in the vapor, to avoid touching the liquid. However, the current study did not have this limitation and the thermocouple could be positioned much closer to the interface since the interface did not fluctuate. To investigate the existence of a thermocapillary flow at the interface, the liquid temperatures in the rectangular cuvette at four equidistant points on the interface were measured. It was found that the first three central points had almost the same temperatures indicating that a thermocapillary flow did not occur on the majority of the interface. However, the temperature of the liquid at the fourth point near the solid walls was a fraction of a degree higher than those of the other three points, confirming the occurrence of a thermocapillary flow near the solid. However, due to lack of data near the solid walls, the extent of the spread of the thermocapillary flow over the interface could not be measured.

The developed models in both geometries were validated with the experimentally measured velocities, temperature profiles in the liquid and vapor, and evaporation fluxes at several pressures. In each geometry, the numerical solutions of the velocities were compared to the experimentally measured velocities obtained from PIV. Both experiment and numerical simulation revealed the existence of a torus shaped vortex below the evaporating meniscus. The vortex in the cylindrical tube had a ring shape due to the symmetry while the vortex in the rectangular cuvette was deformed in the wider direction of the cuvette as a result of the rectangular cross section of the cuvette. It was found that the simulated velocity magnitudes by assuming that the liquid slipped freely at the interface were almost twice as large as the experimental velocities obtained from PIV. However, when the tangential velocity at the interface in the model was set to zero, excellent agreement between the simulated and the experimental velocities was achieved. This led us to conclude that the interfacial flows during the PIV experiments, at least for the slow flow occurring in our study with a typical velocity of ~0.1 mm/s, were almost suppressed. This was also verified by tracking

the individual particles below the interface in the cylindrical tube at a higher magnification and observing that they were trapped at the interface and remained stationary. Thus, special care is needed when PIV is employed to measure the velocities in the liquid below an evaporating interface as the velocities obtained by this technique may not reflect the actual velocities that would occur in a pure liquid.

By using the model, it was found that the main mechanism that gave rise to the observed vortex below the interface in both containers was the buoyancy forces. Identification of the mechanism that generated such a vortical flow was impossible without using the mathematical model. The occurrence of a buoyancy driven flow in the liquid below the interface in experiments identifies an important conclusion, which is that the buoyancy instabilities in water may still exist in the evaporation experiments even when the density of the liquid is vertically stabilized (*i.e.*, the lightest liquid is assumed to always rest on top of the heaviest liquid by setting the bottom temperature). This is very important to be considered in future studies since the absence of a buoyancy flow in water while the temperature at the bottom of the container is kept at 4 °C and the interface temperature is less than 4 °C has been assumed *a priori* in previous studies. However, it was shown in this thesis that a buoyancy driven flow exists under this circumstance. The buoyancy driven flow, although indirectly, played a central role in evaporation from the interface. To be more specific, the drag of the large buoyancy vortex in the bulk of the liquid induced an interfacial flow from the center toward the solid walls, preventing a thermocapillary flow from developing at the interface. It should be noted that even a very slow buoyancy flow with a velocity as low as ~30 μm/s could stop the spread of a thermocapillary flow over the interface, as shown by the numerical simulation. This slow buoyancy driven flow may sometimes be indetectable by experimental devices and lead to an incorrect conclusion that the water interface is quiescent during evaporation. This phenomenon provides a possible answer to the controversial observations that a thermocapillary flow in water does not always exist although the Marangoni numbers are far above the established critical one.

By using the model, it was shown that for containers made from small thermal conductivity materials such as borosilicate glass ($k \approx 1\,\mathrm{W/(m\,K)}$) and quartz ($k \approx 3\,\mathrm{W/(m\,K)}$), the evaporation is completely controlled by heat transfer to the interface. This was inferred by observing that imposing two different theoretical expressions of evaporation flux, namely

statistical rate theory (SRT) and kinetic theory of gases (KTG), gave the same value of evaporation flux in the simulation. More importantly, imposing the KTG expression with different values of condensation coefficients (ψ) also returned the same solutions for the evaporation flux. Therefore, it should not be supprising that the reported values for the condenstion coefficient of water in the literature are highly scattered within the range of 0 and 1 since most of them have probably been obtained from experiments that were dominated by heat transfer. It is hypothesized that the same problem exists during the assesment of temperature discontinuities at the interface by the SRT expression. The SRT expression, which incorporates the interfacial temperature discontinuities, is consistent with a wide range of interfacial vapor temperatures (T^{VI}). That is, if an interfacial vapor temperature, which is several degrees lower (or higher) than the one measured by the thermocouple, is used in the SRT equation, then the predicted pressure (P^{V}) still falls within the experimental uncertainty of the measuring device. Therefore, although the SRT expression is in agreement with the temperature discontinuities measured at the interface, it still can not confirm the reliability of the measured temperature discontinuties at the interface during evaporation.

A practical solution to remove the heat transfer limitation is to carry out the evaporation experiments using a high thermal conductivity material for the container or cuvette. For the specific geometry of the cuvette (rectangular) and the concave interface in our study, a numerical example is provided to show how increasing the thermal conductivity of the cuvette would gradually diminish the limitations associated with the heat transfer. It was demonstrated in the example that the occurrence of a thermocapillary convection at the interface does not remove the heat transfer limitations. The thermal conductivity may still need to be increased much further to remove the heat transfer limitations to evaporation. The results of the numerical simulation suggested that if a material such as graphene ($k \approx 5000\,\mathrm{W/(m\,K)}$) is used, the evaporation would be almost independent of the thermal effects and mostly controlled by transport of molecules across the interface. In such a regime, the evaporation rates would be much larger and the transport phenomena across the interface would be dominant. This would probably be the situation in which the calculated condensation coefficients from the KTG expression would fall within a narrower range (or revolve around a specific value), and the SRT expression would become more sensitive to the interfacial vapor temperatures so that it could predict the temperature jumps within a much narrower range.

In a separate numerical study, the reliability of thermocouples when they are used to measure the temperature jumps at a liquid–vapor interface was investigated. To provide a quantitative analysis of the thermocouple that was minimally affected by the numerical errors, the study of Badam *et al.* was chosen for the numerical study as they had measured relatively large temperature jumps at the interface (up to ~28 °C). By assessing the thermocouple in their study, it was estimated that the temperature jumps were overestimated by almost 50%, mainly due to the rarefaction effects which decrease the thermal heat transfer between the low-density vapor and the thermocouple junction, and partly due to conduction heat transfer through the thermocouple wires to the junction as well as the inaccessibility of the interface due to the finite thickness of the junction and the experimental limitations (*i.e.*, fluctuation of the interface). As discussed earlier, the predicted temperature jumps by the currently available KTG expression are an order of magnitude smaller than the experimental temperature jumps. The SRT expression does not show any disagreement with the measured temperature jumps by thermocouples. Nevertheless, it is still possible that neither of the experimental temperature jumps obtained by a thermocouple nor the predicted temperature jumps by KTG reflect the realistic temperature jumps at the interface. Therefore, further experimental and theoretical efforts should be put into exploring the temperature jumps not only to shed light on the magnitude and direction of the temperature jumps, but also to unravel the cause of such an important concept at an evaporating interface.

Bibliography

(1) Faghri, A. Review and Advances in Heat Pipe Science and Technology. *J. Heat Transfer* **2012**, *134* (12), 123001.

(2) Lim, T.; Han, S.; Chung, J.; Chung, J. T.; Ko, S.; Grigoropoulos, C. P. Experimental Study on Spreading and Evaporation of Inkjet Printed Pico-Liter Droplet on a Heated Substrate. *Int. J. Heat Mass Transf.* **2009**, *52* (1–2), 431–441.

(3) Sau, T. K.; Murphy, C. J. Self-Assembly Patterns Formed upon Solvent Evaporation of Aqueous Cetyltrimethylammonium Bromide-Coated Gold Nanoparticles of Various Shapes. *Langmuir* **2005**, *21* (7), 2923–2929.

(4) Xue, G.; Xu, Y.; Ding, T.; Li, J.; Yin, J.; Fei, W.; Cao, Y.; Yu, J.; Yuan, L.; Gong, L.; et al. Water-Evaporation-Induced Electricity with Nanostructured Carbon Materials. *Nat. Nanotechnol.* **2017**, *12* (4), 317–321.

(5) Chen, X.; Goodnight, D.; Gao, Z.; Cavusoglu, A. H.; Sabharwal, N.; DeLay, M.; Driks, A.; Sahin, O. Scaling up Nanoscale Water-Driven Energy Conversion into Evaporation-Driven Engines and Generators. *Nat. Commun.* **2015**, *6* (June), 7346.

(6) Hu, H.; Larson, R. G. Evaporation of a Sessile Droplet on a Substrate. *J. Phys. Chem. B* **2002**, *106* (6), 1334–1344.

(7) Deegan, R. D.; Bakajin, O.; Dupont, T. F.; Huber, G.; Nagel, S. R.; Witten, T. A. Capillary Flow as the Cause of Ring Stains from Dried Liquid Drops. *Nature* **1997**, *389* (6653), 827–829.

(8) Hertz, H. Ueber Die Verdunstung Der Flüssigkeiten, Insbesondere Des Quecksilbers, Im Luftleeren Raume. *Ann. Phys.* **1882**, *253* (10), 177–193.

(9) Knudsen, M. *Kinetic Theory of Gases*; 3rd ed.; London Methuene: London, 1950.

(10) Schrage, R. W. *A Theoretical Study of Interphase Mass Transfer*; Columbia University Press: New York, 1953.

(11) Fang, G.; Ward, C. A. Temperature Measured close to the Interface of an Evaporating Liquid. *Phys. Rev. E* **1999**, *59* (1), 417–428.

(12) Thompson, I.; Duan, F.; Ward, C. A. Absence of Marangoni Convection at Marangoni Numbers above 27,000 during Water Evaporation. *Phys. Rev. E* **2009**, *80* (5), 56308.

(13) Hu, H.; Larson, R. G. Analysis of the Effects of Marangoni Stresses on the Microflow in an Evaporating Sessile Droplet. *Langmuir* **2005**, *21* (9), 3972–3980.

(14) Cipolla, J. W. Kinetic Theory of Condensation and Evaporation. II. *J. Chem. Phys.* **1974**, *61* (1), 69.

(15) Badam, V. K. Experimental and Theoretical Investigation of the Evaporation of Fluids from Free Surfaces. PhD Thesis, University of Erlangen-Nuremberg (2007).

(16) Badam, V. K.; Kumar, V.; Durst, F.; Danov, K. Experimental and Theoretical Investigations on Interfacial Temperature Jumps during Evaporation. *Exp. Therm. Fluid Sci.* **2007**, *32* (1), 276–292.

(17) Block, M. Surface Tension as the Cause of Benard Cells and Surface Deformation in a Liquid Film. *Nature* **1956**, *178*, 650.

(18) Pearson, J. R. A. On Convection Cells Induced by Surface Tension. *J. Fluid Mech.* **1958**, *4* (5), 489–500.

(19) Bénard, H. Les Tourbillons Cellulaires dans une Nappe Liquide. - Méthodes Optiques D'observation et D'enregistrement. *J. Phys. Theor. Appl., 10* (1), **1901,** 254–266.

(20) Rayleigh, Lord. LIX. On Convection Currents in a Horizontal Layer of Fluid, When the Higher Temperature Is on the under Side. *Philos. Mag. Ser. 6* **1916**, *32* (192), 529–546.

(21) Pan, X.; Jin, W.; Liu, Y.; Ai, F. Effect of Surface Tension-Driven Flow on BaB_2O_4 Crystal Growth from High Temperature Melt-Solution. *Cryst. Res. Technol.* **2008**, *43* (2), 152–156.

(22) Sutter, T.; Kim, N.; Kyu, T.; Golovaty, D. Crystal Nucleation and Motion in an Undercooled Binary Solution. *Curr. Opin. Chem. Eng.* **2015**, *7*, 1–5.

(23) Savino, R.; di Francescantonio, N.; Fortezza, R.; Abe, Y. Heat Pipes with Binary Mixtures and Inverse Marangoni Effects for Microgravity Applications. *Acta Astronaut.* **2007**, *61* (1–6), 16–26.

(24) di Francescantonio, N.; Savino, R.; Abe, Y. New Alcohol Solutions for Heat Pipes:

Marangoni Effect and Heat Transfer Enhancement. *Int. J. Heat Mass Transf.* **2008**, *51* (25–26), 6199–6207.

(25) Cai, Y.; Newby, B. M. Z. Marangoni Flow-Induced Self-Assembly of Hexagonal and Stripelike Nanoparticle Patterns. *J. Am. Chem. Soc.* **2008**, *130* (19), 6076–6077.

(26) Bhardwaj, R.; Fang, X.; Somasundaran, P.; Attinger, D. Self-Assembly of Colloidal Particles from Evaporating Droplets: Role of DLVO Interactions and Proposition of a Phase Diagram. *Langmuir* **2010**, *26* (11), 7833–7842.

(27) Xiao-Hu, Y.; Xi, C. Importance of Marangoni Convection in Laser Full-Penetration Welding. *Chinese Phys. Lett.* **2002**, *19* (6), 788–790.

(28) Lu, S.; Fujii, H.; Nogi, K. Marangoni Convection and Weld Shape Variations in Ar-O_2 and Ar-CO_2 Shielded GTA Welding. *Mater. Sci. Eng. A* **2004**, *380* (1), 290–297.

(29) Ganzevles, F. L. A.; Van Der Geld, C. W. M. Marangoni Convection in Binary Drops in Air Cooled from below. *Int. J. Heat Mass Transf.* **1998**, *41* (10), 1293–1301.

(30) Ghasemi, H.; Ward, C. A. Energy Transport by Thermocapillary Convection during Sessile-Water-Droplet Evaporation. *Phys. Rev. Lett.* **2010**, *105* (13), 136102.

(31) Pereira, F.; Gharib, M.; Dabiri, D.; Modarress, D. Defocusing Digital Particle Image Velocimetry: A 3-Component 3-Dimensional DPIV Measurement Technique. Application to Bubbly Flows. *Exp. Fluids* **2000**, *29* (7), S078–S084.

(32) Elsinga, G. E.; Scarano, F.; Wieneke, B.; Van Oudheusden, B. W. Tomographic Particle Image Velocimetry. *Exp. Fluids* **2006**, *41* (6), 933–947.

(33) Sheng, J.; Malkiel, E.; Katz, J. Using Digital Holographic Microscopy for Simultaneous Measurements of 3D near Wall Velocity and Wall Shear Stress in a Turbulent Boundary Layer. *Exp. Fluids* **2008**, *45* (6), 1023–1035.

(34) Burgmann, S.; Schröder, W. Investigation of the Vortex Induced Unsteadiness of a Separation Bubble via Time-Resolved and Scanning PIV Measurements. *Exp. Fluids* **2008**, *45* (4), 675–691.

(35) Gao, Q.; Wang, H.; Shen, G. Review on Development of Volumetric Particle Image

Velocimetry. *Chinese Sci. Bull.* **2013**, *58* (36), 4541–4556.

(36) Wereley, S. T.; Meinhart, C. D. Recent Advances in Micro-Particle Image Velocimetry. *Annu. Rev. Fluid Mech.* **2010**, *42* (1), 557–576.

(37) Ward, C. A.; Duan, F. Turbulent Transition of Thermocapillary Flow Induced by Water Evaporation. *Phys. Rev. E* **2004**, *69* (5), 56308.

(38) Song, X.; Nobes, D. S. Experimental Investigation of Evaporation-Induced Convection in Water Using Laser Based Measurement Techniques. *Exp. Therm. Fluid Sci.* **2011**, *35* (6), 910–919.

(39) Christy, J. R. E.; Sefiane, K.; Ebeling, J. C.; Seewald, T.; Harmand, S. Flow Measurement Using Micro-PIV and Related Temperature Distributions within Evaporating Sessile Drops of Self-Rewetting Mixtures of 1-Pentanol and Water. In the *4th Micro and Nano Flows Conference, University College London, 7th - 10th September* **2014**.

(40) Buffone, C.; Sefiane, K.; Christy, J. R. E. Experimental Investigation of Self-Induced Thermocapillary Convection for an Evaporating Meniscus in Capillary Tubes Using Micro-Particle Image Velocimetry. *Phys. Fluids* **2005**, *17* (5), 1–18.

(41) Dhavaleswarapu, H. K.; Chamarthy, P.; Garimella, S. V; Murthy, J. Y. Experimental Investigation of Steady Buoyant-Thermocapillary Convection near an Evaporating Meniscus. *Phys. Fluids* **2007**, *19* (8), 82103.

(42) Thokchom, A. K.; Swaminathan, R.; Singh, A. Fluid Flow and Particle Dynamics Inside an Evaporating Droplet Containing Live Bacteria Displaying Chemotaxis. *Langmuir* **2014**, *30* (41), 12144–12153.

(43) Thokchom, A. K.; Gupta, A.; Jaijus, P. J.; Singh, A. Analysis of Fluid Flow and Particle Transport in Evaporating Droplets Exposed to Infrared Heating. *Int. J. Heat Mass Transf.* **2014**, *68*, 67–77.

(44) Babaie, A.; Madadkhani, S.; Stoeber, B. Evaporation-Driven Low Reynolds Number Vortices in a Cavity. *Phys. Fluids* **2014**, *26* (3), 33102.

(45) Minetti, C.; Buffone, C. Three-Dimensional Marangoni Cell in Self-Induced Evaporating

Cooling Unveiled by Digital Holographic Microscopy. *Phys. Rev. E - Stat. Nonlinear, Soft Matter Phys.* **2014**, *89* (1), 1–6.

(46) Brücker, C. Digital-Particle-Image-Velocimetry (DPIV) in a Scanning Light-Sheet: 3D Starting Flow around a Short Cylinder. *Exp. Fluids* **1995**, *19* (4), 255–263.

(47) David, L.; Jardin, T.; Braud, P.; Farcy, A. Time-Resolved Scanning Tomography PIV Measurements around a Flapping Wing. *Exp. Fluids* **2012**, *52* (4), 857–864.

(48) Pommer, M.; Meinhart, C. Shear-Stress Distributions Surrounding Individual Adherent Red Cells in a Microchannel Measured Using Micro-PIV. In *Proceedings of the 6th International Symposium on Particle Image Velocimetry*; 2005; pp 21–23.

(49) Kazemi, M. A.; Elliott, J. A. W.; Nobes, D. S. A 3D Flow Visualization in Evaporation of Water from a Meniscus at Low Pressures. In *The 10th Pacific Symposium on Flow Visualization and Image Processing, Naples, Italy, 15-18 June*; 2015.

(50) Hu, H.; Larson, R. G. Marangoni Effect Reverses Coffee-Ring Depositions. *J. Phys. Chem. B* **2006**, *110* (14), 7090–7094.

(51) Bhardwaj, R.; Fang, X.; Attinger, D. Pattern Formation during the Evaporation of a Colloidal Nanoliter Drop: A Numerical and Experimental Study. *New J. Phys.* **2009**, *11* (7), 75020.

(52) Maki, K. L.; Kumar, S. Fast Evaporation of Spreading Droplets of Colloidal Suspensions. *Langmuir* **2011**, *27* (18), 11347–11363.

(53) Thokchom, A. K.; Majumder, S. K.; Singh, A. Internal Fluid Motion and Particle Transport in Externally Heated Sessile Droplets. *AIChE J.* **2016**, *62* (4), 1308–1321.

(54) David, S.; Sefiane, K.; Tadrist, L. Experimental Investigation of the Effect of Thermal Properties of the Substrate in the Wetting and Evaporation of Sessile Drops. *Colloids Surfaces A Physicochem. Eng. Asp.* **2007**, *298* (1–2), 108–114.

(55) Talbot, E. L.; Berson, A.; Brown, P. S.; Bain, C. D. Evaporation of Picoliter Droplets on Surfaces with a Range of Wettabilities and Thermal Conductivities. *Phys. Rev. E* **2012**, *85* (6), 61604.

(56) Dunn, G. J.; Wilson, S. K.; Duffy, B. R.; David, S.; Sefiane, K. The Strong Influence of Substrate Conductivity on Droplet Evaporation. *J. Fluid Mech.* **2009**, *623* (2009), 329–351.

(57) Bazargan, V.; Stoeber, B. Effect of Substrate Conductivity on the Evaporation of Small Sessile Droplets. *Phys. Rev. E* **2016**, *94* (3), 33103.

(58) Chandra, S.; di Marzo, M.; Qiao, Y. M.; Tartarini, P. Effect of Liquid-Solid Contact Angle on Droplet Evaporation. *Fire Saf. J.* **1996**, *27* (2), 141–158.

(59) McHale, G.; Aqil, S.; Shirtcliffe, N. J.; Newton, M. I.; Erbil, H. Y. Analysis of Droplet Evaporation on a Superhydrophobic Surface. *Langmuir* **2005**, *21* (24), 11053–11060.

(60) Fukatani, Y.; Orejon, D.; Kita, Y.; Takata, Y.; Kim, J.; Sefiane, K. Effect of Ambient Temperature and Relative Humidity on Interfacial Temperature during Early Stages of Drop Evaporation. *Phys. Rev. E* **2016**, *93* (4), 43103.

(61) Dehaeck, S.; Rednikov, A.; Colinet, P. Vapor-Based Interferometric Measurement of Local Evaporation Rate and Interfacial Temperature of Evaporating Droplets. *Langmuir* **2014**, *30* (8), 2002–2008.

(62) McGaughey, A. J. H.; Ward, C. A. Temperature Discontinuity at the Surface of an Evaporating Droplet. *J. Appl. Phys.* **2002**, *91* (10), 6406–6415.

(63) Erbil, H. Y. Evaporation of Pure Liquid Sessile and Spherical Suspended Drops: A Review. *Adv. Colloid Interface Sci.* **2012**, *170* (1–2), 67–86.

(64) Cazabat, A.-M.; Guéna, G. Evaporation of Macroscopic Sessile Droplets. *Soft Matter* **2010**, *6* (12), 2591.

(65) Fang, G.; Ward, C. A. Examination of the Statistical Rate Theory Expression for Liquid Evaporation Rates. *Phys. Rev. E* **1999**, *59* (1), 441–453.

(66) Ward, C. A.; Fang, G. Expression for Predicting Liquid Evaporation Flux: Statistical Rate Theory Approach. *Phys. Rev. E* **1999**, *59* (1), 429–440.

(67) Ward, C. A.; Stanga, D. Interfacial Conditions during Evaporation or Condensation of Water. *Phys. Rev. E* **2001**, *64* (5), 51509.

(68) Kuznetzov, G. V; Sitnikov, A. E. Numerical Modeling of Heat and Mass Transfer in a Low-

Temperature Heat Pipe. *J. Eng. Phys. Thermophys.* **2002**, *75* (4), 840–848.

(69) Kirillov, Y. P.; Shaposhnikov, V. A.; Kuznetsov, L. A.; Shiryaev, V. S.; Churbanov, M. F. Modeling of the Evaporation of Liquids and Condensation of Their Vapor during Distillation. *Inorg. Mater.* **2016**, *52* (11), 1183–1188.

(70) Qin, T.; Tuković, Z.; Grigoriev, R. O. Buoyancy-Thermocapillary Convection of Volatile Fluids under Their Vapors. *Int. J. Heat Mass Transf.* **2015**, *80*, 38–49.

(71) Qin, T.; Tuković, Z.; Grigoriev, R. O. Buoyancy-Thermocapillary Convection of Volatile Fluids under Atmospheric Conditions. *Int. J. Heat Mass Transf.* **2014**, *75*, 284–301.

(72) Koplik, J.; Banavar, J. R.; Willemsen, J. F. Molecular Dynamics of Fluid Flow at Solid Surfaces. *Phys. Fluids A Fluid Dyn.* **1989**, *1* (5), 781–794.

(73) Dussan, E. B. On the Spreading of Liquids on Solid Surfaces: Static and Dynamic Contact Lines. *Annu. Rev. Fluid Mech.* **1979**, *11* (1), 371–400.

(74) de Gennes, P. G. Wetting: Statics and Dynamics. *Rev. Mod. Phys.* **1985**, *57* (3), 827–863.

(75) Navier, C. L. M. H. Mémoire Sur Les Lois Du Mouvement Des Fluides. *Mémoires l'Académie R. des Sci. l'Institut Fr.* **1823**, *6*, 389–440.

(76) Lauga, E.; Brenner, M.; Stone, H. Microfluidics: The No-Slip Boundary Condition. In *Springer Handbook of Experimental Fluid Mechanics*; Springer Berlin Heidelberg: Berlin, Heidelberg, 2007; pp 1219–1240.

(77) Faghri, A.; Zhang, Y. *Transport Phenomena in Multiphase Systems*, 1st ed.; Academic Press, 2006.

(78) Duan, F.; Ward, C. A. Surface-Thermal Capacity of D_2O from Measurements Made during Steady-State Evaporation. *Phys. Rev. E* **2005**, *72* (5), 56304.

(79) Duan, F.; Ward, C. A. Surface Excess Properties from Energy Transport Measurements during Water Evaporation. *Phys. Rev. E* **2005**, *72* (5), 56302.

(80) Popov, S.; Melling, A.; Durst, F.; Ward, C. A. Apparatus for Investigation of Evaporation at Free Liquid–vapour Interfaces. *Int. J. Heat Mass Transf.* **2005**, *48* (11), 2299–2309.

(81) Schrage, R. W. *A Theoretical Study of Interface Mass Transfer*; New York, Columbia University Press, 1953.

(82) McClelland, B. J. *Statistical Thermodynamics*; Chapman and Hall: London, 1973; Vol. 92.

(83) *COMSOL Multiphysics® v. 5.2a,*; AB, Stockholm, Sweden, 2016.

(84) Kestin, J.; Sokolov, M.; Wakeham, W. A. Viscosity of Liquid Water in the Range −8 °C to 150 °C. *J. Phys. Chem. Ref. Data* **1978**, *7* (3), 941.

(85) Kell, G. S. Density, Thermal Expansivity, and Compressibility of Liquid Water from 0 °C to 150 °C. Correlations and Tables for Atmospheric Pressure and Saturation Reviewed and Expressed on 1968 Temperature Scale. *J. Chem. Eng. Data* **1975**, *20* (1), 97–105.

(86) Vinš, V.; Fransen, M.; Hykl, J.; Hrubý, J. Surface Tension of Supercooled Water Determined by Using a Counterpressure Capillary Rise Method. *J. Phys. Chem. B* **2015**, *119* (17), 5567–5575.

(87) Benchikh, O.; Fournier, D.; Boccara, A. C.; Teixeira, J. Photothermal Measurement of the Thermal Conductivity of Supercooled Water. *J. Phys.* **1985**, *46* (5), 727–731.

(88) Duan, F.; Thompson, I.; Ward, C. A. Statistical Rate Theory Determination of Water Properties below the Triple Point. *J. Phys. Chem. B* **2008**, *112* (29), 8605–8613.

(89) Archer, D. G.; Carter, R. W. Thermodynamic Properties of the NaCl + H_2O System. 4. Heat Capacities of H_2O and NaCl(aq) in Cold-Stable and Supercooled States †. *J. Phys. Chem. B* **2000**, *104* (35), 8563–8584.

(90) Wagner, W.; Pruß, A. The IAPWS Formulation 1995 for the Thermodynamic Properties of Ordinary Water Substance for General and Scientific Use. *J. Phys. Chem. Ref. Data* **2002**, *31* (2), 387–535.

(91) Liley, P. E. Thermophysical Properties of Ice/Water/Steam from −20°C to 50°C. *Int. J. Mech. Eng. Educ.* **2005**, *33* (1), 45–50.

(92) Rohsenow, W. M.; Hartnett, J. P.; Cho, Y. I. *Handbook of Heat Transfer*; New York: McGraw-Hill, 1998; Vol. 3.

(93) Kang, K. H.; Lim, H. C.; Lee, H. W.; Lee, S. J. Evaporation-Induced Saline Rayleigh

Convection inside a Colloidal Droplet. *Phys. Fluids* **2013**, *25* (4), 42001.

(94) Lee, S. J.; Hong, J.; Choi, Y. Evaporation-Induced Flows inside a Confined Droplet of Diluted Saline Solution. *Langmuir* **2014**, *30* (26), 7710–7715.

(95) Li, Y.; Yoda, M. Convection Driven by a Horizontal Temperature Gradient in a Confined Aqueous Surfactant Solution: The Effect of Noncondensables. *Exp. Fluids* **2014**, *55* (1), 1663.

(96) Farley, R. W.; Schechter, R. S. Retardation of Surface Velocities by Surfactants. *Chem. Eng. Sci.* **1966**, *21*, 1079–1093.

(97) Cuenot, B.; Magnaudet, J.; Spennato, B. The Effects of Slightly Soluble Surfactants on the Flow around a Spherical Bubble. *J. Fluid Mech.* **1997**, *339*, 25–53.

(98) Wu, T.-C.; Yang, Y.-M.; Maa, J.-R. Surfactant-Induced Retardation of the Thermocapillary Flow at a Gas/liquid Interface. *Int. Commun. Heat Mass Transf.* **2000**, *27* (5), 655–666.

(99) Duan, F.; Badam, V. K.; Durst, F.; Ward, C. A. Thermocapillary Transport of Energy during Water Evaporation. *Phys. Rev. E* **2005**, *72* (5), 56303.

(100) Bond, M.; Struchtrup, H. Mean Evaporation and Condensation Coefficients Based on Energy Dependent Condensation Probability. *Phys. Rev. E* **2004**, *70* (6), 61605.

(101) Eames, I. W.; Marr, N. J.; Sabir, H. The Evaporation Coefficient of Water: A Review. *Int. J. Heat Mass Transf.* **1997**, *40* (12), 2963–2973.

(102) Persad, A. H.; Ward, C. A. Expressions for the Evaporation and Condensation Coefficients in the Hertz-Knudsen Relation. *Chem. Rev.* **2016**, *116* (14), 7727–7767.

(103) Julin, J.; Shiraiwa, M.; Miles, R. E. H.; Reid, J. P.; Pöschl, U.; Riipinen, I. Mass Accommodation of Water: Bridging the Gap Between Molecular Dynamics Simulations and Kinetic Condensation Models. *J. Phys. Chem. A* **2013**, *117* (2), 410–420.

(104) Duan, F.; Ward, C. A. Investigation of Local Evaporation Flux and Vapor-Phase Pressure at an Evaporative Droplet Interface. *Langmuir* **2009**, *25* (13), 7424–7431.

(105) Das, K. S.; Ward, C. A. Surface Thermal Capacity and Its Effects on the Boundary Conditions at Fluid-Fluid Interfaces. *Phys. Rev. E* **2007**, *75* (6), 65303.

(106) Pao, Y.-P. Temperature and Density Jumps in the Kinetic Theory of Gases and Vapors. *Phys. Fluids* **1971**, *14* (2), 306.

(107) Shankar, P. N.; Deshpande, M. D. On the Temperature Distribution in Liquid-Vapor Phase Change between Plane Liquid Surfaces. *Phys. Fluids A* **1990**, *2* (1990), 1030.

(108) Hisatake, K.; Tanaka, S.; Aizawa, Y. Evaporation Rate of Water in a Vessel. *J. Appl. Phys.* **1993**, *73* (11), 7395–7401.

(109) Ghasemi, H.; Ward, C. A. Mechanism of Sessile Water Droplet Evaporation: Kapitza Resistance at the Solid–liquid Interface. *J. Phys. Chem. C* **2011**, *115* (43), 21311–21319.

(110) He, B.; Duan, F. Statistical Rate Theory Approach on the Ethanol Droplet Evaporation. In *ASME 2012 Heat Transfer Summer Conference Collocated with the ASME 2012 Fluids Engineering Division Summer Meeting and the ASME 2012 10th International Conference on Nanochannels, Microchannels, and Minichannels*; ASME, 2012; pp 681–685.

(111) Persad, A. H. Statistical Rate Theory Expression for Energy Transported during Evaporation. PhD Thesis, University of Toronto (2014), University of Toronto.

(112) Persad, A. H.; Ward, C. A. Statistical Rate Theory Examination of Ethanol Evaporation. *J. Phys. Chem. B* **2010**, *114* (18), 6107–6116.

(113) Kazemi, M. A.; Nobes, D. S.; Elliott, J. A. W. Experimental and Numerical Study of the Evaporation of Water at Low Pressures. *Langmuir* **2017**, *33* (18), 4578–4591.

(114) Zhu, Z. Q.; Liu, Q. S. Interfacial Temperature Discontinuities in a Thin Liquid Layer during Evaporation. *Microgravity Sci. Technol.* **2013**, *25* (4), 243–249.

(115) Zhu, Z. Q.; Liu, Q. S.; Xie, J. C. Experimental Study on the Combined Evaporation Effect and Thermocapillary Convection in a Thin Liquid Layer. *Microgravity Sci. Technol.* **2009**, *21* (SUPPL. 1), 241–246.

(116) Gatapova, E. Y.; Graur, I. A.; Kabov, O. A.; Aniskin, V. M.; Filipenko, M. A.; Sharipov, F.; Tadrist, L. The Temperature Jump at Water–Air Interface during Evaporation. *Int. J. Heat Mass Transf.* **2017**, *104*, 800–812.

(117) Attia, M. H.; Cameron, A.; Kops, L. Distortion in Thermal Field Around Inserted

Thermocouples in Experimental Interfacial Studies, Part 4: End Effect. *J. Manuf. Sci. Eng.* **2002**, *124* (1), 135.

(118) Attia, M. H.; Kops, L. Distortion in Thermal Field around Inserted Thermocouples in Experimental Interfacial studies–Part II: Effect of the Heat Flow through the Thermocouple. *J. Eng. Ind.* **1988**, *110* (1), 7.

(119) Lyons, B. E.; Samulski, T. V; Britt, R. H. Temperature Measurements in High Thermal Gradients: I. The Effects of Conduction. *Int. J. Radiat. Oncol. Biol. Phys.* **1985**, *11* (5), 951–962.

(120) Samulski, T. V.; Lyons, B. E.; Britt, R. H. Temperature Measurements in High Thermal Gradients: II. Analysis of Conduction Effects. *Int. J. Radiat. Oncol. Biol. Phys.* **1985**, *11* (5), 963–971.

(121) Hindasageri, V.; Vedula, R. P.; Prabhu, S. V. Thermocouple Error Correction for Measuring the Flame Temperature with Determination of Emissivity and Heat Transfer Coefficient. *Rev. Sci. Instrum.* **2013**, *84* (2), 24902.

(122) Chen, X.; Xia, X.-L.; Sun, C.; Li, Y. Numerical Analysis on the Transient Measurement of Gas Temperature in Porous Material Using Thermocouples at High Temperatures. *Int. J. Heat Mass Transf.* **2015**, *91*, 1060–1068.

(123) Fu, X.; Luo, X. Can Thermocouple Measure Surface Temperature of Light Emitting Diode Module Accurately? *Int. J. Heat Mass Transf.* **2013**, *65*, 199–202.

(124) AlWaaly, A. A. Y.; Paul, M. C.; Dobson, P. S. Effects of Thermocouple Electrical Insulation on the Measurement of Surface Temperature. *Appl. Therm. Eng.* **2015**, *89*, 421–431.

(125) He, Q.; Smith, S.; Xiong, G. Thermocouple Attachment Using Epoxy in Electronic System Thermal Measurements — A Numerical Experiment. In *2011 27th Annual IEEE Semiconductor Thermal Measurement and Management Symposium* IEEE, 2011; pp 280–291.

(126) Weng, C.; Li, W.; Hwang, C. Gaseous Flow in Microtubes at Arbitrary Knudsen Numbers. *Nanotechnology* **1999**, *10*, 373–379.

(127) Dongari, N.; Agrawal, A. Modeling of Navier-Stokes Equations for High Knudsen Number Gas Flows. *Int. J. Heat Mass Transf.* **2012**, *55* (15–16), 4352–4358.

(128) Zhang, W. M.; Meng, G.; Wei, X. A Review on Slip Models for Gas Microflows. *Microfluid. Nanofluidics* **2012**, *13* (6), 845–882.

(129) Maxwell, J. C. On Stresses in Rarefied Gases Arising from Inequalities of Temperature. *Philos. Trans. R. Soc. London* **1879**, *170*, 231–256.

(130) Smolan, M. S. von. Ueber Wärmeleitung in Verdünnten Gasen. *Ann. Phys.* **1898**, *300* (1), 101–130.

(131) Greenshields, C. J.; Reese, J. M. Rarefied Hypersonic Flow Simulations Using the Navier-Stokes Equations with Non-Equilibrium Boundary Conditions. *Prog. Aerosp. Sci.* **2012**, *52*, 80–87.

(132) Vera, J.; Bayazitoglu, Y. Temperature and Heat Flux Dependence of Thermal Resistance of Water/metal Nanoparticle Interfaces at Sub-Boiling Temperatures. *Int. J. Heat Mass Transf.* **2015**, *86*, 433–442.

(133) Vera, J. Temperature and Heat Flux Dependence of Thermal Resistance of Water/metal Nanoparticle Interfaces. PhD Thesis, Rice University (2014), Rice University.

(134) Caldwell, F. R. *Thermocouple Materials*; U.S. Department of Commerce, National Bureau of Standards: Washington, 1962.

(135) Duan, F.; Ward, C. A.; Badam, V. K.; Durst, F. Role of Molecular Phonons and Interfacial-Temperature Discontinuities in Water Evaporation. *Phys. Rev. E* **2008**, *78* (4), 41130.

(136) Sharipov, F. Data on the Velocity Slip and Temperature Jump on a Gas-Solid Interface. *J. Phys. Chem. Ref. Data* **2011**, *40* (2), 23101.

(137) Sharipov, F. Data on the Velocity Slip and Temperature Jump Coefficients [Gas Mass, Heat and Momentum Transfer]. In *5th International Conference on Thermal and Mechanical Simulation and Experiments in Microelectronics and Microsystems, 2004. EuroSimE 2004. Proceedings of the* IEEE, 2004; pp 243–249.

(138) Beskok, A.; Karniadakis, G. E.; Trimmer, W. Rarefaction and Compressibility Effects in

Gas Microflows. *J. Fluids Eng.* **1996**, *118* (3), 448.

(139) Silva, E.; Rojas-Cardenas, M.; Deschamps, C. J. Experimental Analysis of Velocity Slip at the Wall for Gas Flows of Nitrogen, R134a, and R600a through a Metallic Microtube. *Int. J. Refrig.* **2016**, *66*, 121–132.

(140) Josyula, E.; Burt, J. *Review of Rarefied Gas Effects in Hypersonic Applications*; Air force Res. lab Wright-Patterson AFB OH: Air force research lab Wright-Patterson AFB OH, 2011.

(141) Sefiane, K.; Bennacer, R. An Expression for Droplet Evaporation Incorporating Thermal Effects. *J. Fluid Mech.* **2011**, *667*, 260–271.

(142) Hu, H.; Larson, R. G. Analysis of the Effects of Marangoni Stresses on the Microflow in an Evaporating Sessile Droplet. *Langmuir* **2005**, *21* (9), 3972–3980.

(143) Hu, H.; Larson, R. G. Analysis of the Microfluid Flow in an Evaporating Sessile Droplet. *Langmuir* **2005**, *21* (9), 3963–3971.

(144) Deegan, R. D.; Bakajin, O.; Dupont, T. F.; Huber, G.; Nagel, S. R.; Witten, T. A. Contact Line Deposits in an Evaporating Drop. *Phys. Rev. E* **2000**, *62* (1), 756–765.

(145) Sobac, B.; Brutin, D. Thermal Effects of the Substrate on Water Droplet Evaporation. *Phys. Rev. E* **2012**, *86* (2), 21602.

(146) Hu, D.; Wu, H.; Liu, Z. Effect of Liquid–vapor Interface Area on the Evaporation Rate of Small Sessile Droplets. *Int. J. Therm. Sci.* **2014**, *84*, 300–308.

(147) Sáenz, P. J.; Wray, A. W.; Che, Z.; Matar, O. K.; Valluri, P.; Kim, J.; Sefiane, K. Dynamics and Universal Scaling Law in Geometrically-Controlled Sessile Drop Evaporation. *Nat. Commun.* **2017**, *8*, 14783.

(148) Vélez-Cordero, J. R.; Yáñez Soto, B.; Arauz-Lara, J. L. Transport of Colloids along Corners: Visualization of Evaporation-Induced Flows beyond the Axisymmetric Condition. *Langmuir* **2016**, *32* (32), 8171–8181.

(149) Marek, R.; Straub, J. Analysis of the Evaporation Coefficient and the Condensation Coefficient of Water. *Int. J. Heat Mass Transf.* **2001**, *44* (1), 39–53.

(150) Kazemi, M. A.; Nobes, D. S.; Elliott, J. A. W. Effect of the Thermocouple on Measuring the Temperature Discontinuity at a Liquid–Vapor Interface. *Langmuir* **2017**, *33* (28), 7169–7180.

(151) Song, X. Song, X., Experimental Investigation on Evaporation Induced Convection in Water Using Laser Based Measurement Techniques. MSc. Thesis, University of Alberta (2010). 2010.

(152) Kazemi, M.A., Experimental and Numerical Study on Evaporation of Water at Low Pressures, Ph.D. Thesis, University of Alberta (2017).

(153) Kotula, A. P.; Anna, S. L. Probing Timescales for Colloidal Particle Adsorption Using Slug Bubbles in Rectangular Microchannels. *Soft Matter* **2012**, *8* (41), 10759.

(154) Hunter, T. N.; Pugh, R. J.; Franks, G. V.; Jameson, G. J. The Role of Particles in Stabilising Foams and Emulsions. *Adv. Colloid Interface Sci.* **2008**, *137* (2), 57–81.

(155) Hu, H.; Larson, R. G. Marangoni Effect Reverses Coffee-Ring Depositions. *J. Phys. Chem. B* **2006**, *110* (14), 7090–7094.

(156) Xu, X.; Luo, J. Marangoni Flow in an Evaporating Water Droplet. *Appl. Phys. Lett.* **2007**, *91* (12).

(157) Zhang, W.; Shen, R.; Lu, K.; Ji, A.; Cao, Z. Nanoparticle Enhanced Evaporation of Liquids: A Case Study of Silicone Oil and Water. *AIP Adv.* **2012**, *2* (4), 42119.

(158) Wang, H.; Pan, Z.; Garimella, S. V. Numerical Investigation of Heat and Mass Transfer from an Evaporating Meniscus in a Heated Open Groove. *Int. J. Heat Mass Transf.* **2011**, *54* (13–14), 3015–3023.

Appendix A: Cylindrical Image Distortion Correction in MATLAB

To correct for the radial distortion of the images acquired during the PIV experiments in the cylindrical tube, the following code was written in MATLAB and applied to the images.

```
%*************************************************************************
clc
clear
% Read the distorted image
%*************************************************************************
file_address ='D:\Mohammad Amin Kazemi\University of Alberta\Experimental Data\Cylindrical Tube\May 26, 2016\0010.png';          % Select the directory containing the images
AA =imread(file_address);
[mm,nn,oo]=size(AA);
% Enter the values below for every set of images that you are going to correct:
wall_l=152;              %Manually, specify the right wall (pixel);
wall_r=2534;             %Manually, specify the right wall (pixel);
centre=floor((wall_r-wall_l)/2)+wall_l;

% From the center to the right
%*************************************************************************
led=wall_r-center;      % Distance between the right wall and the center in the distorted image
leu=0.755244755*led;% Distance between the right wall and the center in the undistorted image
q(1)=center;             % Positions of lines in the undistorted image
qc =[0 .1875*leu .372685*leu .550926*leu .738426*leu .916667*leu 1*leu];
for i=1:6
   q(i+1)=center+qc(i+1);
end
q=round(q);              % Positions of lines in the distorted image
qq(1)=center;
qqc=[0 0.185315*led 0.374126*led  0.559441*led  0.758741*led  0.935315*led  1*led];
for i=1:6                % The target image is divided into 5 parts, from the center to the right wall
   qq(i+1)=centre+qqc(i+1);
```

```
end
qq=round(qq);          % Positions of lines in the distorted image

%From the center to the left
%*************************************************************************
ql(1)=centre;
qcl =[0  0.1875*leu  0.372685*leu  0.550926*leu  0.738426*leu  0.916667*leu 1*leu];
for i=1:6              % The target image is divided into 5 parts, from the center to the left wall
   ql(i+1)=centre-qcl(i+1);
end
ql=round(ql);          % Positions of lines in the undistorted image
qql(1)=centre;
qqcl=[0  0.185315*led  0.374126*led  0.559441*led  0.758741*led  0.935315*led  1*led];
for i=1:6
   qql(i+1)=centre-qqcl(i+1);
end
qql=round(qql);        % Positions of lines in the undistorted image

% Divide the distorted image into several compartments
%*************************************************************************
% for the right part:
comp1=AA(:,qq(1)+1:qq(2),:);
comp2=AA(:,qq(2)+1:qq(3),:);
comp3=AA(:,qq(3)+1:qq(4),:);
comp4=AA(:,qq(4)+1:qq(5),:);
comp5=AA(:,qq(5)+1:qq(6),:);
comp6=AA(:,qq(6)+1:qq(7),:);

% and for the left part:

comp1_l=AA(:,qql(2):qql(1),:);
comp2_l=AA(:,qql(3):qql(2),:);
```

```
comp3_l=AA(:,qql(4):qql(3),:);
comp4_l=AA(:,qql(5):qql(4),:);
comp5_l=AA(:,qql(6):qql(5),:);
comp6_l=AA(:,qql(7):qql(6),:);

% Resize the small parts based on the target image
%************************************************************************
comp1resized=imresize(comp1,'nearest','OutputSize',[mm q(2)-q(1)]);
comp2resized=imresize(comp2,'nearest','OutputSize',[mm q(3)-q(2)]);
comp3resized=imresize(comp3,'nearest','OutputSize',[mm q(4)-q(3)]);
comp4resized=imresize(comp4,'nearest','OutputSize',[mm q(5)-q(4)]);
comp5resized=imresize(comp5,'nearest','OutputSize',[mm q(6)-q(5)]);
comp6resized=imresize(comp6,'nearest','OutputSize',[mm q(7)-q(6)]);

% and for the left part:
comp1resized_l=imresize(comp1_l,'nearest','OutputSize',[mm ql(1)-ql(2)]);
comp2resized_l=imresize(comp2_l,'nearest','OutputSize',[mm ql(2)-ql(3)]);
comp3resized_l=imresize(comp3_l,'nearest','OutputSize',[mm ql(3)-ql(4)]);
comp4resized_l=imresize(comp4_l,'nearest','OutputSize',[mm ql(4)-ql(5)]);
comp5resized_l=imresize(comp5_l,'nearest','OutputSize',[mm ql(5)-ql(6)]);
comp6resized_l=imresize(comp6_l,'nearest','OutputSize',[mm ql(6)-ql(7)]);

% Mirror the left side
%************************************************************************
comp1resized_l=fliplr(comp1resized_l);
comp2resized_l=fliplr(comp2resized_l);
comp3resized_l=fliplr(comp3resized_l);
comp4resized_l=fliplr(comp4resized_l);
comp5resized_l=fliplr(comp5resized_l);
comp6resized_l=fliplr(comp6resized_l);

% Assemble the new compartments:
```

```
%**************************************************************************
s1=size(comp1resized);
s2=size(comp2resized);
s3=size(comp3resized);
s4=size(comp4resized);
s5=size(comp5resized);
s6=size(comp6resized);

acc1=s1(2);
acc2=s2(2)+acc1;
acc3=s3(2)+acc2;
acc4=s4(2)+acc3;
acc5=s5(2)+acc4;
acc6=s6(2)+acc5;

New_image(:,1:s1(2),:)=comp1resized;
New_image(:,acc1+1:acc2,:)=comp2resized;
New_image(:,acc2+1:acc3,:)=comp3resized;
New_image(:,acc3+1:acc4,:)=comp4resized;
New_image(:,acc4+1:acc5,:)=comp5resized;
New_image(:,acc5+1:acc6,:)=comp6resized;

New_image_l(:,1:s1(2),:)=comp1resized_l;
New_image_l(:,acc1+1:acc2,:)=comp2resized_l;
New_image_l(:,acc2+1:acc3,:)=comp3resized_l;
New_image_l(:,acc3+1:acc4,:)=comp4resized_l;
New_image_l(:,acc4+1:acc5,:)=comp5resized_l;
New_image_l(:,acc5+1:acc6,:)=comp6resized_l;
New_image_l=fliplr(New_image_l);

% Saving the corrected image into a file
```

```
%*************************************************************************
imwrite(New_image,file_address)
ssr=size(New_image);
ssl=size(New_image_l);
% final_image=zeros(mm,ssr(2)+ssl(2)+1,oo);
final_image(:,1:ssl(2),:)=New_image_l;
final_image(:,ssl(2)+1:ssr(2)+ssl(2),:)=New_image;
imwrite(final_image,file_address)
%********************************* THE END *********************************
```

Appendix B: Calibration of the Thermocouple with the Thermometer

To calibrate the thermocouple at temperatures below 0 °C, the measuring junction was placed into a mixture of ice, sodium chloride, and water. The thermocouple was calibrated in the calibrating liquid against a reference platinum resistance thermometer. The calibration curve is demonstrated in Figure B1. Also, the measured temperatures by both the thermocouple and the thermometer are listed in Table B1.

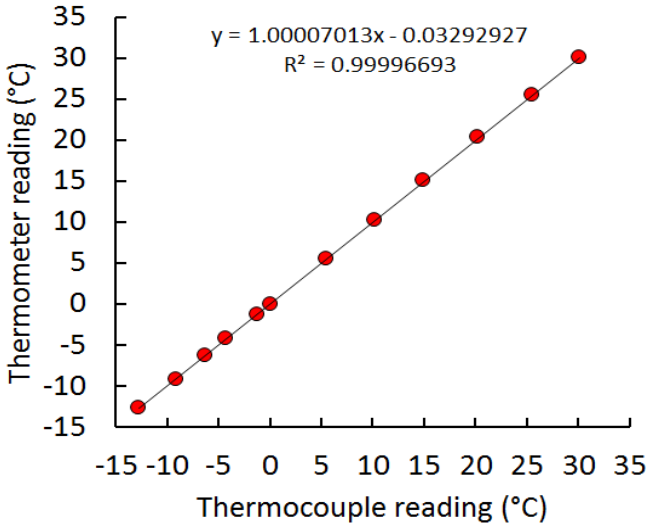

Figure B1 Calibration curve that converts the temperatures read by the thermocouple (horizontal axis) to those read by the thermometer (vertical axis) by using the equation of the fitted line.

Table B1 Comparison between the thermometer and thermocouple readings.

Test #	$T_{\text{thermometer}}$ (°C)	$T_{\text{thermocouple}}$ (°C)	$T_{\text{fitted line}}$ (°C)	$T_{\text{thermocouple}} - T_{\text{thermometer}}$ (°C)	$T_{\text{thermocouple}} - T_{\text{fitted line}}$ (°C)
1	−12.62	−12.68	−12.71	−0.06	0.034
2	−9.15	−9.13	−9.16	0.02	0.034
3	−6.29	−6.19	−6.22	0.10	0.033
4	−4.15	−4.19	−4.22	−0.04	0.033
5	−1.34	−1.20	−1.23	0.14	0.033
6	0.01	0.08	0.05	0.07	0.033
7	5.51	5.58	5.55	0.07	0.033
8	10.16	10.28	10.25	0.12	0.032
9	15.07	14.98	14.95	−0.09	0.032
10	20.32	20.25	20.22	−0.07	0.032
11	25.42	25.53	25.50	0.11	0.031
12	30.12	30.14	30.11	0.02	0.031

Appendix C: Determination of the Time Constants of the Thermocouple in the Liquid and Vapor

During the automated temperature measurements in the liquid and vapor, it is required that the temperatures be collected fast enough to make sure that the change in the position of the interface is small, but the junction should stop at each measuring point long enough to ensure that the collected temperatures are not affected by the transition response of the thermocouple as it travels between two points. Therefore, understanding the response time of the thermocouple is essential to optimize the timing of the measurements.

The responses of the thermocouple to the temperature change as a result of moving from one point to another point in the fluids are shown in Figure C1. It can be seen that the response of the thermocouple is similar to the step response of a first order system. By fitting an exponential function to the experimental temperatures, it was found that the response time of the thermocouple, defined as the time required to reach 63.2% of the temperature change, in the liquid and vapor were 0.372 s, and 0.645 s respectively.

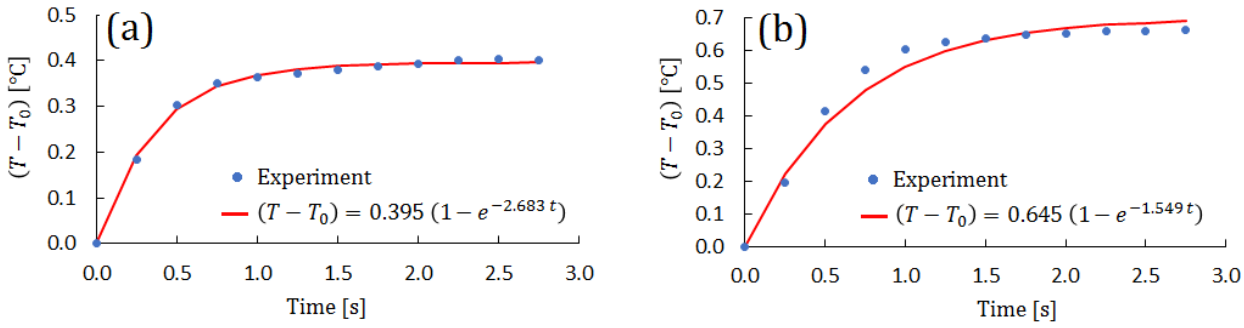

Figure C1 Responses of the thermocouple when it measures the temperatures in the (a) liquid and (b) vapor.

Appendix D: Calculation of the Area of the Interface

To calculate the surface area of the meniscus formed in the cylindrical cuvette, the undistorted image of the interface was approximated by a 6th order polynomial, and the resultant curve was revolved around the z axis:

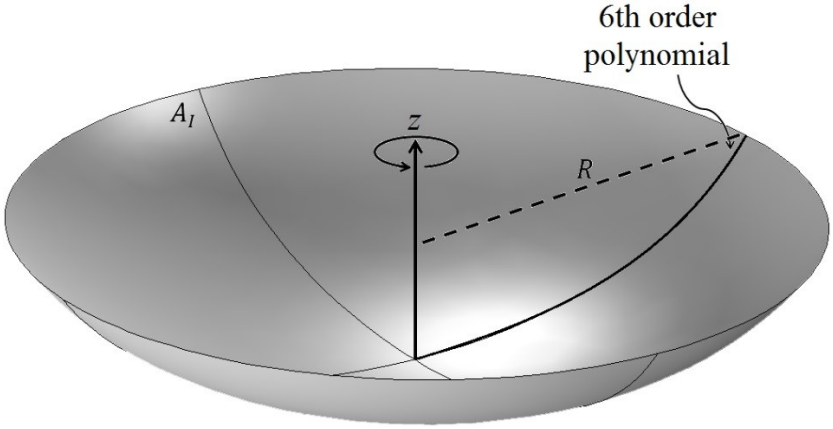

Figure D1 The area of the interface formed in the cylindrical cuvette calculated numerically by revolving a fitted curve to the interface around the vertical axis.

As a result, the area of the interface, A_I, was found to be 137.58 mm^2. The cross-sectional area of the tube was also calculated by $A_c = \pi R^2$, and was found to be 107.16 mm^2.

To calculate the surface area of the meniscus formed in the rectangular cuvette, some 3D curves at the center as well as the contact lines were extracted from the images taken from two perpendicular views. Then a loft surface was generated by connecting the curves in space together, as shown in Figure D2.

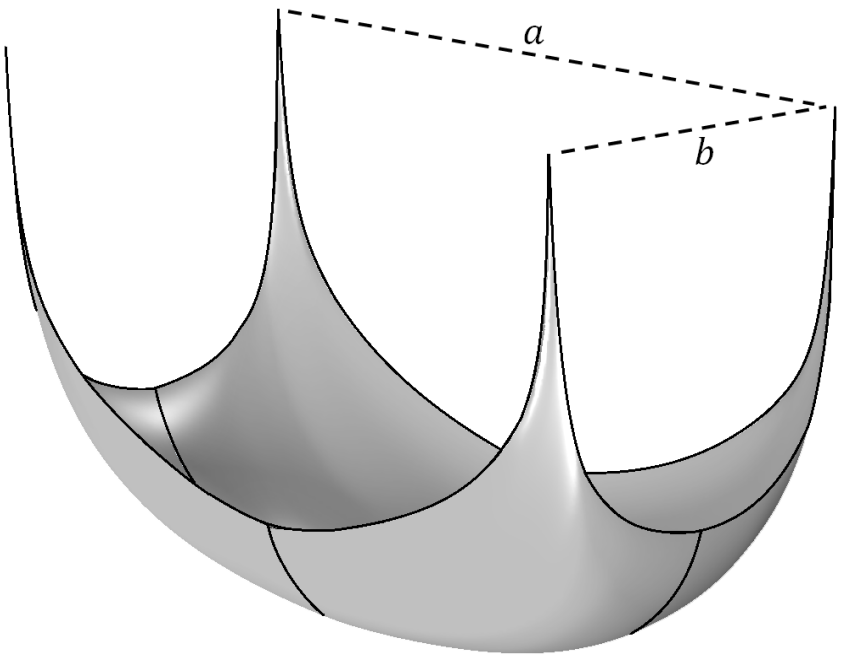

Figure D2 The area of the interface formed in the rectangular cuvette can be calculated numerically after reconstructing the 3D interface. The width and the depth of the channel is 10 mm and 4 mm respectively.

As a result, the area of the interface, A_I, was calculated to be 67.41 mm^2. The cross-sectional area of the tube was also calculated by $A_c = a \times b$, and was 40.00 mm^2.

Appendix E: Mesh Convergence Study in the Numerical Simulations

The meshed domains used in the numerical studies in the cylindrical tube and the rectangular cuvette are shown in Figure E1.

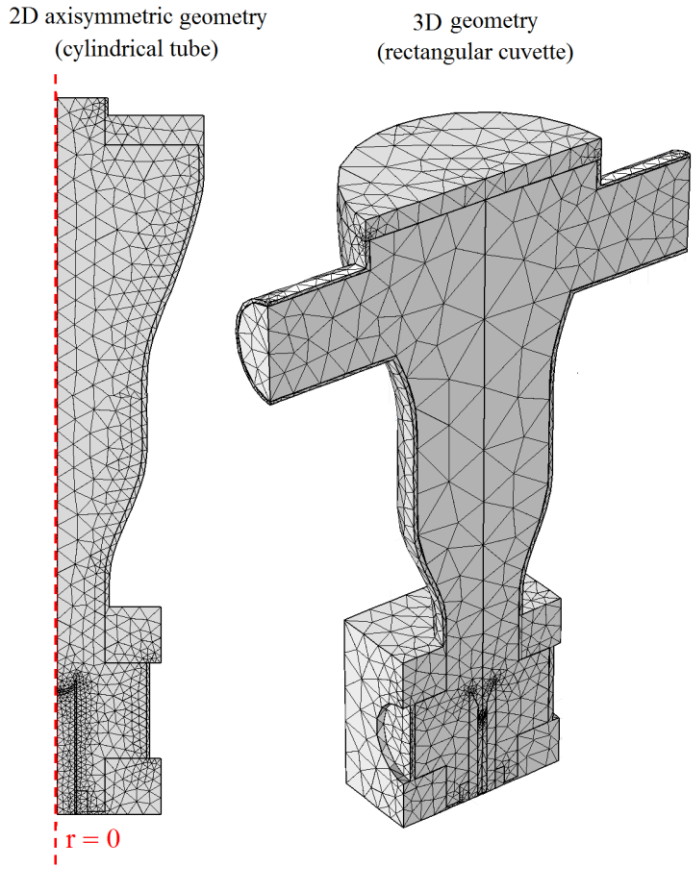

Figure E1 Illustration of the domains used in the numerical simulation and the type of the mesh used for discretizing the domains. The mesh size in the numerical simulations was smaller than what is shown here.

To make sure that the obtained solutions are independent of the mesh size, the number of the meshes are increased progressively until no significant change is observed in the calculated parameters.

As an example, for the numerical simulation of the evaporation in the cylindrical tube and the rectangular cuvette, the mesh study procedure for a typical condition is described. For the other numerical studies including the simulation of the thermocouple, a similar procedure was followed.

Figure E2 shows the percentage of the change in the computed total evaporation flux as the number of elements in the liquid and vapor increase. The mesh refinement stopped when the relative change in the total evaporation flux was less than 0.01%. For the cylindrical tube at $P^V =$ 190 Pa, the number of elements in the liquid and vapor that satisfied the mentioned condition were 20,325 and 46,568, respectively. For the rectangular cuvette at the same pressure, the number of elements in the liquid and vapor were found to be 250,333 and 595,321, respectively.

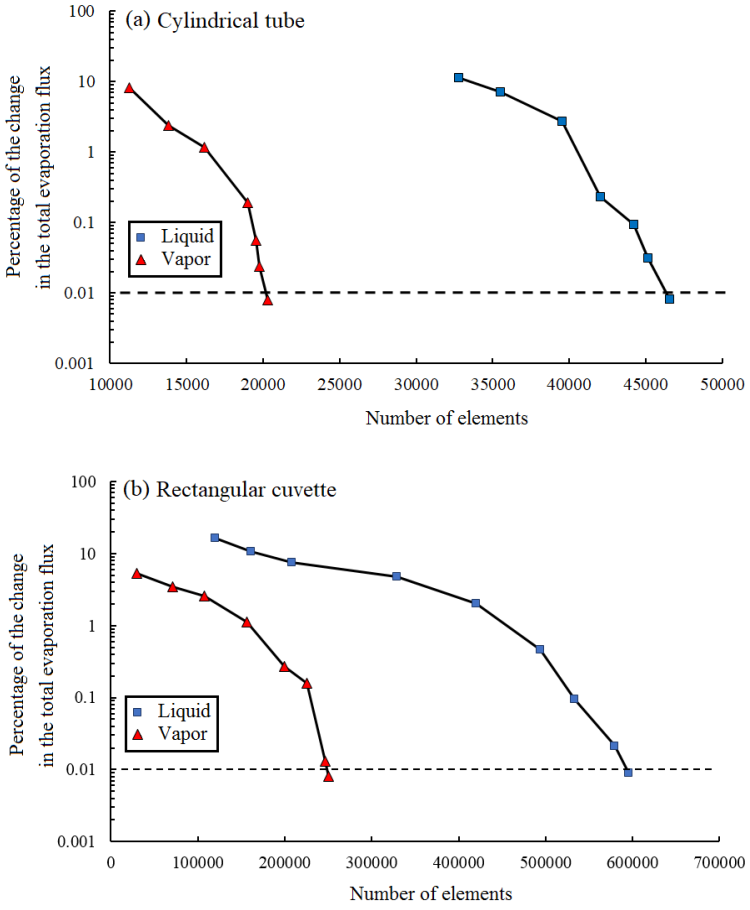

Figure E2 Reduction of the relative error while calculating the evaporation flux as the number of elements increases in the liquid and vapor, (a) cylindrical tube, and (b) rectangular cuvette.

Appendix F: The Sensitivity of SRT to the Temperature of Vapor at the Interface

In section 4.1, it was mentioned that in the studies of McGaughey and Ward [McGaughey, A. J. H.; Ward, C. A. Temperature Discontinuity at the Surface of an Evaporating Droplet. *J. Appl. Phys.* 2002, *91* (10), 6406–6415.], the calculated jumps could decrease, vanish, and become negative for some experimental conditions by manipulating the measured temperatures and position of the interface within the experimental uncertainties. To show this, consider the temperature of the vapor at the interface as reported in the mentioned study:

$$T_i^V = T_{tc}^V + (T^B - T_{tc}^V)\frac{1/r_V - 1/r_D}{1/r_V - 1/r_B}, \tag{F.1}$$

where r_D is the radius of the droplet, r_V is the distance between the center of the droplet and the thermocouple in the vapor, r_B is the distance between the center of the droplet and the chamber wall, T_i^V is the temperature of the vapor at the interface, T_{tc}^V is the temperature of the vapor at r_V, and T^B is the temperature of the vapor at the wall. The uncertainties associated with measuring the droplet radius (r_D) and the temperatures were reported as ± 0.04 mm and ± 0.1 °C respectively. Table F1 summarizes the values of these parameters in their experiments. In experiment 1, by decreasing only the thermocouple temperature T_{tc}^V by 0.1 °C while keeping all other parameters constant, the temperature jump decreases from 1.00 °C to 0.35 °C. In experiment 2, by decreasing the thermocouple temperature T_{tc}^V by 0.06 °C and increasing r_D by 0.01 mm, the temperature jump becomes zero. In experiment 3, by decreasing only the thermocouple temperature T_{tc}^V by 0.1 °C, the temperature jump changes from 0.68 °C to −0.22 °C.

Table F1 Three selected experimental conditions near an evaporating droplet extracted from the study of McGaughey and Ward

Exp. No.	T_{tc}^V (°C)	T^B (°C)	r_V (mm)	r_D (mm)	r_B (mm)	T_i^V (°C)	T_i^L (°C)	Reported temperature jump, $T_i^V - T_i^L$(°C)
1	26.54	26.87	4.08	0.69	27	24.63	23.63	1.00
2	26.66	26.87	4.43	0.51	27	24.75	24.07	0.68
3	26.61	26.87	4.24	0.57	27	24.61	23.98	0.63

Appendix G: Estimation of the Effect of Thermal Radiation on Thermocouple Readings

In the simulation of the heat transfer to the thermocouple in Chapter 4, we neglected the radiation to the thermocouple. Herein, we quantitatively show that this assumption is valid. We should note that it has already been proved in [Badam, V. K. Experimental and Theoretical Investigation of the Evaporation of Fluids from Free Surfaces. Ph.D. Thesis, University of Erlangen-Nuremberg (2007)] that the radiative heat transfer from the heating element to the thermocouple is much smaller than the convective heat transfer between the vapor and the thermocouple. However, in the mentioned analysis, several simplifying assumptions were made to assess the amount of radiative heat transfer to the thermocouple. Those include:

- The whole thermocouple arrangement was simplified to a sphere with a uniform temperature and the radiation to the wires was neglected. This cannot be a good assumption because the surface area of the wires that are exposed to the radiation is much larger than that of the bead. Moreover, when the thermocouple is located at the interface the wires are closer to the heating element than the bead is. This means that the wires are more exposed to the radiation from the heating element than the bead.
- The conduction heat transfer through the wires to the bead was not taken into account and the comparison was only made between the amount of radiation to the bead and the heat removed by convection mechanism from the bead to the vapor.

Here, we have performed a more detailed analysis of the heat transfer to the thermocouple by taking into account the conduction, convection, and radiation mechanisms at the same time. Figure G1 shows the thermocouple and the heating element arrangement which are designed according to the information provided in reference mentioned earlier. Let us make some hypothetical assumptions by which the radiation plays the maximum role:

- The thermocouple is in the vapor side.
- The heating element works at the highest temperature (200°C).
- The emissivity of the heating element is 1 (the actual emissivity is around 0.09).

- The thermocouple only absorbs radiation from the heating element and doesn't emit energy to the colder liquid interface.

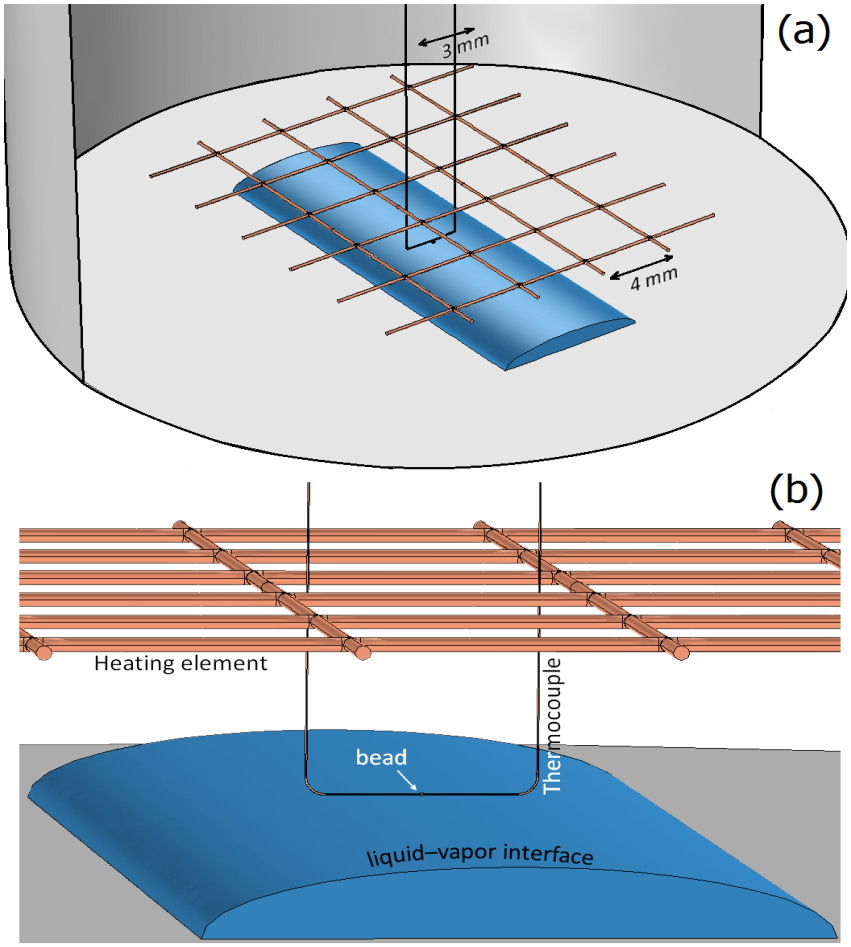

Figure G1 The arrangement of the thermocouple and the heating element from two different views. The thermocouple bead and wire diameters are 25 μm and 12.5 μm respectively. The size of the mesh wires was reported to be in the range of 0.1 mm–0.3 mm. We assumed the largest diameter to maximize the effect of radiation.

Based on these extreme values, the simulation showed that the maximum difference between the thermocouple readings at the interface with and without considering the radiation mechanism was 0.61°C. This is a negligible value compared to the interfacial temperature jump of 27.82°C in this condition. Given that the amount of radiation from the heating element to the thermocouple should be much smaller than what we used in this simulation, one can ignore the disturbance by the radiation in the similar temperature measurement experiments.